DEFORMATION BEHAVIOR AND MECHANICAL ANALYSIS OF VERTICALLY ALIGNED CARBON NANOTUBE (VACNT) BUNDLES

Thesis by

Shelby B. Hutchens

In Partial Fulfillment of the Requirements

for the Degree of

Doctor of Philosophy

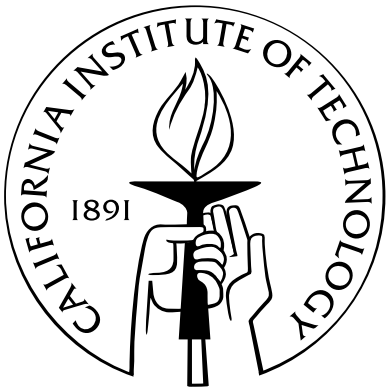

California Institute of Technology

Pasadena, California

2011

(Defended May 16, 2011)

Acknowledgements

I have had a rich and defining experience during my period at Caltech. Though many times I did not take the smoothest or most efficient path, I am very thankful to have had to opportunity to make the mistakes and overcome the obstacles that are now a cherished part of who I am as a researcher and an individual. Many people have assisted me with guidance, empathy, wisdom, and distraction when needed. I would like to thank a few especially.

The two people most responsible for my progression as a researcher are my advisors, Professors Zhen-Gang Wang and Julia R. Greer. Professor Wang consistently provided me with clear, neutral, and unaffected advice. Through his guidance I learned what it means to think deeply about scientific problems and address them with rigor, though I did not always appreciate this lesson as it was being taught. I am very grateful to have had the opportunity to know and work with him. Professor Greer has provided me with a shining example of the kind of person, science and otherwise, that I would like to become. She and her group also reintroduced me to the excitement and fun of science. I am eternally grateful for every chance she gave me to participate in the scientific community as a part of conferences, workshops, and meetings. These experiences, with her example to guide me, have helped to give me both the perspective and confidence I lacked and continue to improve upon. I also appreciate all of the time she so generously gave me in one-on-one conversations. Her insight has provided me with lessons that have shaped the way that I see the world around me, particularly science questions and my interactions with others.

I would also like to express my appreciation to our collaborator, Professor Alan Needleman, for his time, frank input, wisdom, and patience. Thanks to Professor Greer, I have been truly lucky to have had the chance to interact so closely with him.

There are several of my peers I would like to recognize. I thank Roseanna Zia for her

freely given confidence and friendship. She is an inspiration both scientifically and as a human being. I look forward to our lifelong friendship and am thankful to have met her. I am grateful for the friendship and support of my fellow incoming class of chemical engineering women and the "girly" lunches we shared: Heather Hunt, Lisa Hochrein, Arwen Brown, and Heather McCaig. I am indebted to all of the members of the Greer group, particularly Andrew Jennings and Dongchan Jang, from whom I learned my appreciation of scientific discussion and debate. I wish to express my gratitude to the Danger Twins and company for welcoming me without judgement, to every visiting speaker I hosted for the advice they so willingly gave, and to all of my summer students for the opportunity to learn through our interactions. I would also like to recognize Josh Spurgeon; our time together is a treasured memory.

Finally, I would like to thank my family, whose support of and faith in my ability got me to a position where I could reap all of the benefits of the aforementioned relationships. A thank you goes in particular to my mother, I love you very much, and I one day hope to attain your level of optimism.

I think my graduate experience can best be summed up by an adage I received in a recent email from Professor Needleman.

> I may have told you about experience:
> How did you learn how to make good decisions? Experience.
> How did you get experience? Bad decisions.

I would also like to acknowledge the funding for my graduate work through the generous donation of the Gordan and Betty Moore Foundation's Teaching and Research Fellowship at Caltech as well as the Institute for Collaborative Biotechnnologies (ICB) at Caltech (ARO Award #UCSB.ICB4b).

Abstract

Vertically aligned carbon nanotubes (VACNTs) serve as integral components in a variety of applications including MEMS devices, energy absorbing materials, dry adhesives, light absorbing coatings, and electron emitters, all of which require structural robustness. It is only through an understanding of VACNT's structural mechanical response and local constitutive stress-strain relationship that future advancements through rational design may take place. Even for applications in which the structural response is not central to device performance, VACNTs must be sufficiently robust and therefore knowledge of their microstructure-property relationship is essential. This thesis first describes the results of *in situ* uniaxial compression experiments of 50 micron diameter cylindrical bundles of these complex, hierarchical materials as they undergo unusual deformation behavior. Most notably they deform via a series of localized folding events, originating near the bundle base, which propagate laterally and collapse sequentially from bottom to top. This deformation mechanism accompanies an overall foam-like stress-strain response having elastic, plateau, and densification regimes with the addition of undulations in the stress throughout the plateau regime that correspond to the sequential folding events. Microstructural observations indicate the presence of a strength gradient, due to a gradient in both tube density and alignment along the bundle height, which is found to play a key role in both the sequential deformation process and the overall stress-strain response. Using the complicated structural response as both motivation and confirmation, a finite element model based on a viscoplastic solid is proposed. This model is characterized by a flow stress relation that contains an initial peak followed by strong softening and successive hardening. Analysis of this constitutive relation results in capture of the sequential buckling phenomenon and a strength gradient effect. This combination of experimental and modeling approaches motivates discussion of the particular microstructural mechanisms and local material behavior

that govern the non-trivial energy absorption via sequential, localized buckle formation in the VACNT bundles.

Contents

List of Figures

List of Notation

Following is a list of mathematical symbols used in this thesis. Only symbols used throughout the thesis are presented. The page on which the symbol is first defined is given on the right.

$\dot{}$	indicates the time derivative of a variable	63
ϵ_{n}	nominal or engineering strain	48
ϵ_{t}	true strain	67
ν	Poisson's ratio	26
σ_{n}	nominal or engineering stress	48
σ_{t}	true stress	74
ϕ	phase angle	15
E	Young's or elastic modulus	23
f	frequency, in Hz	15
H	pillar height before deformation	48
p_{h}	harmonic load amplitude	15
R	pillar radius before deformation	48
u_{h}	harmonic displacement amplitude	15
u_z	axial displacement	66

Chapter 1

Introduction

The study of materials science is typified by the relationships between a material's structure, properties, and processing. Characterization of these relationships yields a full description of the material of interest. This thesis focuses largely on the first two aspects, structure and properties, for a structure composed of vertically aligned carbon nanotubes (VACNTs) while bearing in mind the influence of processing on the samples tested and the information reported in the literature. VACNTs can be grown in macroscopic, continuous films and have become materials of interest due to both their relative ease of growth with respect to other fullerene-based structures and the unique properties of their carbon nanotube building blocks. In addition, they have shown promise in a wide array of applications many of which take advantage of their inherently multifunctional nature. The focus in the following study has been on the mechanical response of these materials, particularly under compression, in which they show an unusual structural response that is explored through *in situ* experiments and finite element analysis. These observations of VACNT structure and microstructure lead to increased understanding of the mechanisms responsible for and constitutive stress-strain relationship of their complex, local material behavior.

1.1 Definition and General Characteristics of Vertically Aligned Carbon Nanotubes

VACNTs can be thought of as both standalone materials and structures of CNT struts. They are remarkable not only for their structure, but for the unique characteristics of these

struts. Promising thermal, electrical, and mechanical properties have made carbon nanotubes (CNTs) the subject of study in fields ranging from medicine to electronics [1–4]. A single walled CNT (SWCNT) generally has a diameter close to 1 nm and is composed of a single sheet of graphene, a monolayer of carbon atoms in a hexagonal arrangement, in the shape of a cylinder (see Fig. 1.1(a)). Multiwalled carbon nanotubes (MWCNTs) consist of multiple concentric layers of graphene-like sheets ranging from two (double-walled CNTs) to several, with a sheet to sheet spacing of 3.4 Å [5] and diameters typically less than 100 nm [6]. Experiments have demonstrated thermal conductivities on the order of 200 W m^{-1} K^{-1} for bulk single-walled CNTs and 3000 W m^{-1} K^{-1} for an individual MWCNT [7] with theoretical predictions for the single-walled tube as high as 2980 W m^{-1} K^{-1} [8]. These numbers are 10 times those of conventional materials, i.e., metals. CNTs are also unique in that they can display both metallic and semiconducting electrical properties depending on their chirality (Fig. 1.1(a)). In their metallic configuration, they have a high electrical conductivity, comparable to that of Cu [9]. Most relevant to this work, MWCNTs have been shown to be one of the strongest materials tested, having a tensile modulus on the

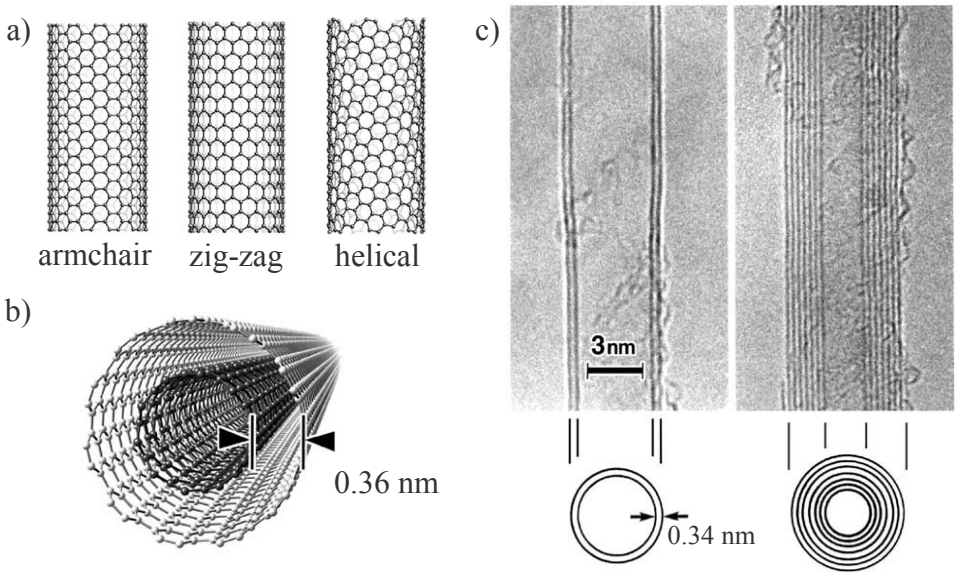

Figure 1.1: Pictorial definition of single- and multiwalled carbon nanotubes [5]. **a)** Illustration of the possible chirality configurations leading to differing electronic behavior. **b)** Diagram showing the layout of concentric graphene layers within a double walled CNT. **c)** Transmission electron micrographs of single and multiwalled CNTs. (Reprinted from [5] with permission from Elsevier.)

order of 1 TPa and a strength of tens of GPa [9]. However, due to their high aspect ratio (length/radius), MWCNTs bend or buckle readily when subject to compressive loads, doing so at much lower loads than those required for yield in tension. They have been shown to bend as much as 120° without breaking atomic bonds [10], enabling them to recover almost completely after such deformation. It is for all of these features that CNTs are a vast and prominent area of study. When combined to create a VACNT material they form a complex, hierarchical structure that bridges the gap between the nano and macro scales while maintaining many of the promising mechanical, thermal, and electrical properties of individual tubes and displaying new aspects of each arising from the collective interactions of the tubes.

Generally, VACNTs are nominally vertically aligned arrays of carbon nanotubes grown perpendicularly from a stiff substrate, typically Si or Quartz. The term vertically aligned carbon nanotubes comes from the fact that at relatively low magnifications, $1000\times$, the tubes appear highly aligned as illustrated in Fig. 1.2. It is because of this that they have also been referred to as CNT turfs, forests, brushes, mats, and foams. At $100\times$ higher magnifications (center image in Fig. 1.2), the CNTs are found to be intertwined with and adhered to each other. At this lengthscale, the anisotropy that was so obvious at lower magnification now begins to disappear in favor of isotropy. Magnifying $100\times$ more (right image in Fig. 1.2), the transmission electron microscopy (TEM) image individual structure

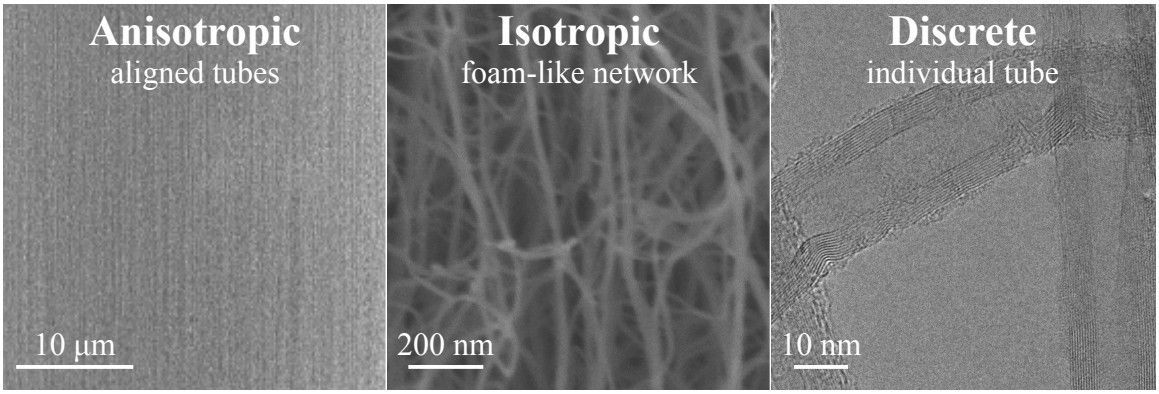

Figure 1.2: A series of micrographs illustrating the hierarchical nature of the VACNTs studied in this thesis. The left and center images are taken with a scanning electron microscope (SEM). The right image is a transmission electron microscope (TEM) image courtesy of A. T. Jennings showing the multiwall nature of the CNTs.

of the MWCNTs. This specific geometry differs from shorter forests in which tubes are either less tightly packed or shorter, preventing in complex tube entanglement that is one of the defining characteristics of VACNTs. The microstructure is also unlike CNT conglomerates or CNT composite materials in that there is typically no anisotropy due to nominal alignment in either of these examples.

VACNTs are relatively easy to grow and pattern. A typical synthesis technique is that of chemical vapor deposition (CVD) at atmospheric pressure and temperatures around 750 °C [11]. A precursor gas (e.g., ethylene) is flowed across a thin layer of catalyst (e.g., Fe) supported by a wafer substrate (e.g., Si or quartz). There are many issues with and studies on the growth mechanisms of VACNTs including efforts to control density, alignment, tube diameter, wall number, and chirality [12] that are beyond the scope of this thesis. Using the CVD technique, samples nearly 2 cm tall have been grown [6]. Typically the tubes in these materials are MWCNTs, as high purity SWCNTs are more difficult to obtain. Creation of a continuous film versus a patterned VACNT structure is often achieved through selective catalyst deposition, with photolithographic patterning of the catalyst leading to patterned VACNTs. Alternative growth techniques include simultaneous flow of both the precursor gas and the catalyst during CVD [13] and high temperature vacuum decomposition [14], which only results in very short arrays of less than 1 μm tall, to mention a few. The specifics of the growth process utilized for this thesis, based on the typical CVD techniques discussed first, are given in detail in Section 2.2.1.1.

1.2 Applications

Inspired by the many uses for the unique electrical and extraordinary mechanical properties of individual CNTs, as well the relative ease of production of VACNTs, researchers have begun to explore their possible role in a variety of technologies. A thorough review of all of these applications is not the primary aim of this thesis, though a remarkable, albeit incomplete, list of those in which the mechanical properties of VACNTs are central to design and function includes: components of highly compliant thermal contacts for micro-electro-mechanical-systems (MEMS) and microelectronics [15, 16], dry adhesives [17, 18],

thermally robust energy dissipating rubber [14, 19, 20], and energy absorption or impact mitigation [13, 21, 22]. Even in applications where the mechanical behavior is not central to design or implementation, an understanding of the mechanisms of deformation and fatigue behavior is essential for analysis of the life-in-use of the device. Several properties unique to VACNTs make them desirable candidates for these applications. First, VACNTs are unique in that they are both soft materials, due to the reduced load capacity of the CNT struts as they bend, and highly conductive materials, both electrically and thermally, while being thermally robust and non-oxidizing. Thermal contacts for MEMS and other microelectronic systems look to take advantage of their simultaneous thermal conductivity, or ability as a heat sink, and their compliance, in order to avoid damaging delicate features. Additionally, VACNT's hierarchical structure allows them to conformally contact surfaces, which is necessary both in maximizing thermal transfer and for increasing bonding between surfaces in the case of dry adhesives. In the case of dry adhesives, also called CNT tapes, the large contact area combined with the properties of the tubes themselves enable the material to withstand shear stresses of 36 N/cm^2, nearly four times higher than the gecko foot, as well as to stick to a variety of surfaces, including Teflon [17].

The interconnected, network-like structure of VACNTs closely resembles foams or other fibrous structures which traditionally find use as energy absorbers. In this application, the CNTs serve as the struts supporting the open structure of the material. A stress-strain curve for a characteristic elastic-plastic foam is shown in Figure 1.3. This response in-

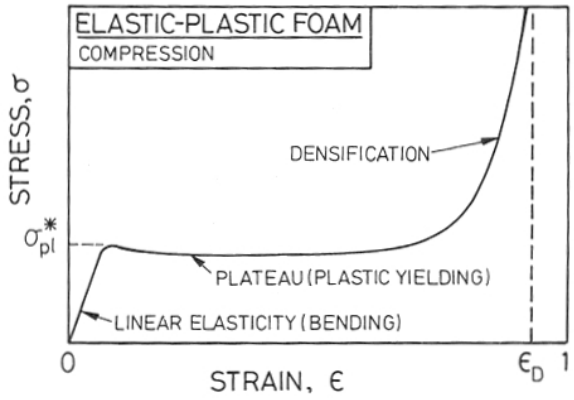

Figure 1.3: A typical stress strain curve for an elastic-plastic foam undergoing uniaxial compression [23]. Note the three distinct regimes: elastic, plateau, and densification.

cludes three distinct regimes: elastic loading, a stress plateau, and densification. The open structure allows for accommodation of large deformation for minimal changes in applied load throughout the plateau regime during which the struts bend and buckle. The result is a large area under the stress-strain curve that translates to a large amount of energy absorbed. When viewed in this framework, the CNTs, connected through their intertube interactions, serve as the struts supporting the open structure of the material. By nature, these struts are both strong and lightweight, making them ideal candidates. In fact, VACNTs have been observed to undergo an overall foam-like response [24], but do so in a highly localized manner that is very different from traditional foams as will be discussed in detail in Chapter 4.

Additionally, experiments have shown VACNTs to exhibit highly viscoelastic behavior. Researchers have surmised that energy dissipation in these materials arises from sliding and reorganization between tubes [19, 20] though detailed studies of the mechanism have not been reported at the time of this writing. This viscoelastic response, combined with their thermal robustness, enables VACNTs to act as energy dissipators or dampers at temperatures where traditional damping materials, i.e., polymers, become brittle (low temperatures) or ineffective (high temperatures).

1.3 Objectives and Scope

The objective of this thesis is to explore the mechanical deformation behavior of a class of materials known as vertically aligned carbon nanotubes. Specifically, the focus is on a relatively new, unusual, and largely unstudied phenomenon recently observed in VACNTs, that of sequential periodic buckling in VACNTs under uniaxial loading. This rich mechanical behavior is characterized *in situ* and used to motivate a constitutive relation for these complex, multiscale materials that may one day be utilized for capturing the structural response of these materials in any geometry.

Notably, we observe, during deformation, the sequential buckling phenomena and report on the nucleation and propagation behavior while uniquely correlating that phenomena to the stress–strain response as discussed in Chapter 4. The proposed constitutive model (Chapter 5), captures the qualitative structural response of uniaxially compressed VACNTs

in more than one dimension. This work is not intended to be the end of the story, but to provide the groundwork for understanding the deformation mechanisms in VACNTs with the hope that the understanding will allow future researchers to eventually tailor these unique structures to their needs.

Chapter 2

Experimental Procedure

2.1 Introduction

Mechanical properties are extracted from materials in a wide variety of methods including notched fracture testing, nanoindentation, bending tests, tension, plane strain or stress, and the list goes on. In this thesis, uniaxial compression tests are the chosen testing method for several reasons. First, nanoindentation, while simple in setup because it requires little specialized sample preparation and therefore can be performed quickly, is difficult to analyze. Stress concentrations occur at the indenter's tip or its edge (depending on indenter geometry) and corresponding strain gradients can make characterization of non-elastic or non-monolithic materials behavior non-trivial, particularly when deformation mechanisms are poorly understood as with VACNTs. Additionally, geometry independent mechanical variables like stress and strain are difficult or impossible to calculate. Second, energy absorption and dissipation applications motivate this work. Since these applications would utilize VACNTs in compression, fracture, bending, and tension tests are less applicable. Plus, uniaxial compressions enable straightforward analysis in terms of engineering stress and strain, as will be discussed in Section 2.4. Finally, experiments are performed on small scale samples via microcompression (in a nanoindenter) as opposed to macrocompressions in order to resolve load–displacement features occuring at low loads as well as conduct *in situ* studies of the deformation. As will be shown in Chapter 4, these low loads allow resolution of the localized response, which enables extraction of a complex and detailed load versus deformation responses for analysis, discussed in Chapter 5.

In order to extract the sample's load–displacement response from the raw load and displacement data gathered during an experiment, the complete description and characterization of the indenter system must be obtained. This description and procedure is described in Section 2.3. A model of the indenter-plus-sample system is discussed in Section 2.4in order to correctly deconvolute the sample and testing system responses. In Section 2.5 a method for dynamic mechanical analysis that allows the viscoelastic response of a material can be characterized is described. This method measures the storage and loss stiffnesses of a material, which can be functions of the frequency of excitation. Finally, a description of the *in situ* micromechanical testing setup, SEMentor, is given in Section 2.6.

2.2 Sample and Nanoindenter Tip Fabrication for Uniaxial Testing

In order to obtain the desired uniaxial testing geometry specialized sample geometries, circular cylinders, as well as two flat punch nanoindenter tips for *in situ* and ex situ testing are produced.

2.2.1 VACNT sample preparation

Cylindrical samples of VACNTs, which will be referred to interchangeably as both pillars and bundles, were created using the two methods described below. Cylindrical samples were initially prepared using a focused ion beam (FIB) to mill CNT material out of a continuous CNT film. Poor sample quality with this method lead to acquiring prepatterned cylindrical samples through a collaboration with Lee J. Hall and Harish Manohara at the Jet Propulsion laboratory.

2.2.1.1 Photolithographically patterned VACNT pillars

Pillars of VACNTs, also called CNT bundles, are grown on a generic Si wafer (with ∼300-–400 nm thermal oxide) patterned using contact photolithography, then cleaned with O_2 plasma. Al is then evaporated onto the substrate in a ∼3.0–3.5 nm layer after which the

chamber is vented to atmosphere to allow the Al to oxidize, forming an Al_2O_3 barrier layer. This layer performs the function of reducing diffusion of the Fe catalyst into the substrate which can interfere with CNT growth. Next, a ∼2.5–3.0 nm layer of active catalyst Fe is evaporated. The lift-off process removes the photoresist leaving only the patterned catalyst, and the wafer is placed in a 2 inch diameter quartz tube, single zone furnace outfitted with vacuum exhaust and an automated throttle valve. The quartz tube is purged and filled with Ar (99.999% pure Ar, 'UHP' grade from Airgas) 3 times, then pressure is held at 200 Torr while flowing Ar at 500 sccm and simultaneously ramping the temperature to 675 °C. When the temperature is stable at 675 °C, Ar is quickly switched out and a flow of 500 sccm of ethylene (99.995% C_2H_4, 'Research Grade' from Airgas) is begun in order to grow the multiwall CNTs. Run times are typically between 15 and 30 minutes. To end growth, the Ar and ethylene are quickly switched again and the furnace is allowed to cool to near room temp under flowing Ar. This method is discussed in further depth in Manohara et. al. [25] and references therein. These samples, whose mechanical deformation is described in this thesis, were grown by Lee J. Hall at the Jet Propulsion Laboratory. Samples are chosen from the array of grown pillars using an SEM according to three criteria: They adhere to the desired cylindrical shape (no missing parts, few stray tubes), they are perpendicular to the substrate (see Fig. 2.1), and their aspect ratio is between 1 and 1.5.

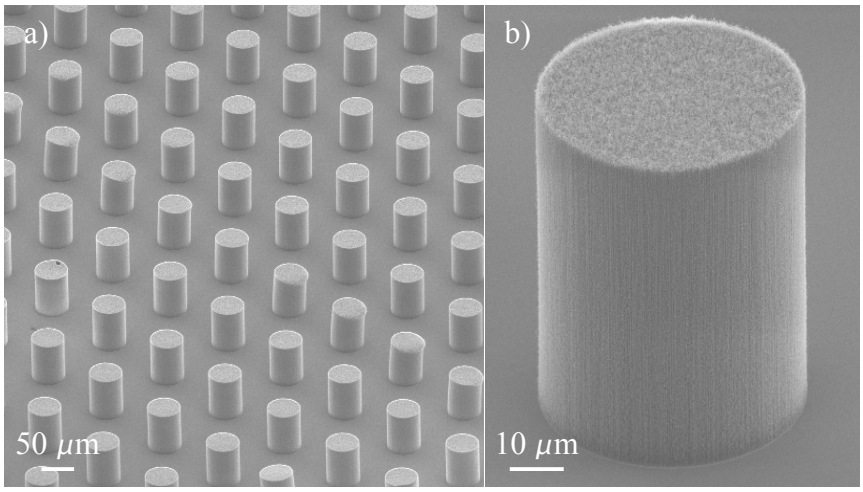

Figure 2.1: An array of 50 μm diameter pillars (left) and an individual pillar (right) as grown via CVD with photolithographically defined catalyst.

2.2.1.2 Focused Ion Beam Milled VACNT pillars

VACNTs are most easily and more commonly grown in continuous films. Therefore, it is of some interest to develop a method for small scale testing of the properties of these continuous films in uniaxial compression. Following methods utilized for creating uniaxial compression samples for small scale metallic samples, annuli were milled in the VACNT material, resulting in pillars. The continuous, VACNT films were grown via CVD and obtained through a collaboration with Chiara Daraio of Caltech. The milling was done under the focused ion beam (FIB) of a dual beam system (FEI Nova 200). FIB milling

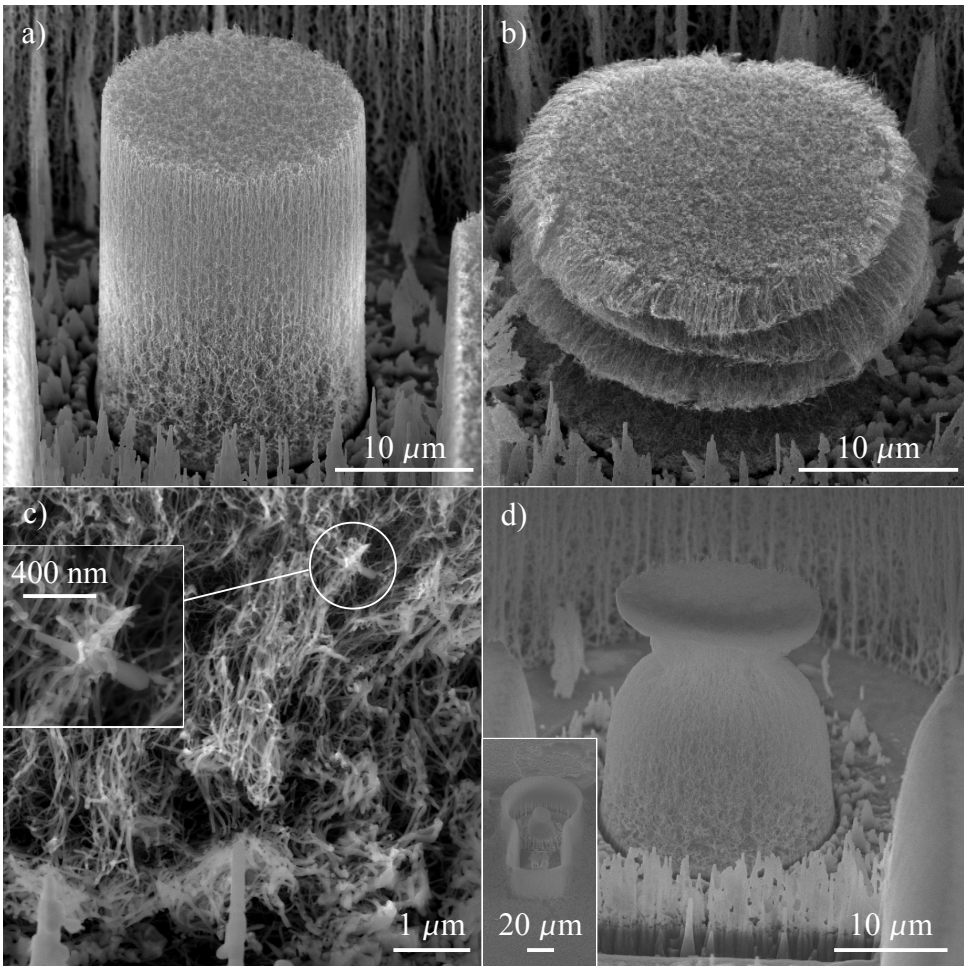

Figure 2.2: Summary of issues facing FIB milled pillars. **a)** A FIB milled pillar before compression. **b)** The same pillar in a) post-uniaxial compression. **c)** Close up of compressed pillar base showing interaction with redeposition and redeposition fracture. **d)** An uncompressed FIB milled pillar after attempt at redeposition removal using an oxygen plasma. The inset reveals that the redeopsition walls remain standing while the VACNT material that had been surrounding them was etched away.

was enhanced through the use of the selective carbon mill, which is essentially a needle that injects water vapor close to the area being milled in order to increase the oxidation of carbonaceous materials into CO_2 [26]. The milling was performed at a series of ion beam currents starting at 7 nA for removal of large regions of material and gradually decreasing to 3 nA for cleaner results toward the end. Sample geometries created typically had a radius of 20 μm or 50 μm with an aspect ratio (height/radius) of 2.5. Images of the pre- and post-compression FIB milled pillars illustrate the results achieved with this process (Figs. 2.2(a) and (b)). The milling process was prone to the accumulation of redeposition in the milled region around the pillar and on the outer edge of the pillar itself (see Figure 2.2). Attempts were made to minimize these anomalies by careful milling in sequentially smaller annuli, but their reduction to an acceptable level was never realized. An attempt to remove the redeposition was made using an oxygen plasma etcher. Unfortunately, this treatment results in removal of the VACNTs themselves, a deformed pre-compression pillar, and almost no removal of the redeposition (Fig. 2.2(d)). Post-compression images of FIB milled microcompression samples showed fracture in the difficult to remove redeposition (Fig. 2.2(c)). Additionally, the pillar and the flat punch interact with the remaining redeposition structures that surround it, as evidenced by the inset in Fig. 2.2(c). Thus, the mechanical response of the VACNT material was certainly convoluted with the mechanical response of the FIB redeposition and this sample preparation method was deemed unacceptable. The milling schedule for a 50 μm diameter pillar is given in Appendix C.

2.2.1.3 Diamond Indenter Tip Fabrication

Nanomechanical instrumentation typically utilizes diamond for the mechanical probe in direct contact with a sample due to its high stiffness and yield strength. However, the geometry of the mechanical probe is traditionally sharp, i.e., a Berkovitch, cube corner, or conical shape. In order to perform uniaxial compressions of the VACNT micropillar samples described in Section 2.2.1, flat punch tip geometries were fabricated for both testing instruments, the Agilent Nano Indenter G200 and the SEMentor. Both indenter tips were milled using the focused ion beam of an FEI Nova200 dual beam system in combination with the selective carbon mill (described in the previous section). The large, circular flat

punch (Fig. 2.3) took over 550 hours to mill at 20 nA current and was designed to be mounted in the G200 system. The final geometry has a diameter of approximately 100 μm and a length of approximately 90 μm. The smaller, rectangular flat punch (Fig. 2.4) has a width of 80 μm and a depth of 60 μm with a miniature flat punch (effectively 5 μm $\times$ 5 μm) attached to the side for compression of smaller bundles of CNTs. Its height is only 30 μm because displacement in the SEMentor is limited to 30 μm so any further height increase is unusable.

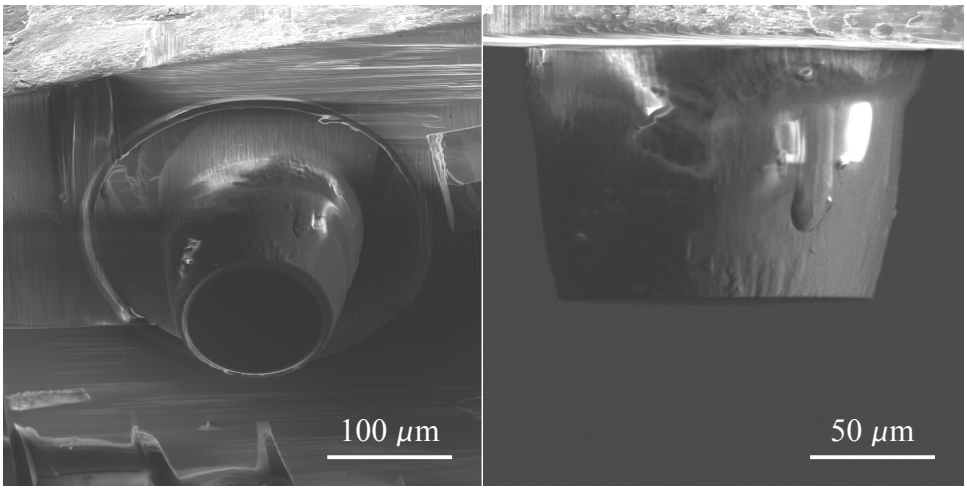

Figure 2.3: Top (left) and side (right) views of the diamond flat punch indenter tip after focused ion beam milling from a Berkovitch tip geometry.

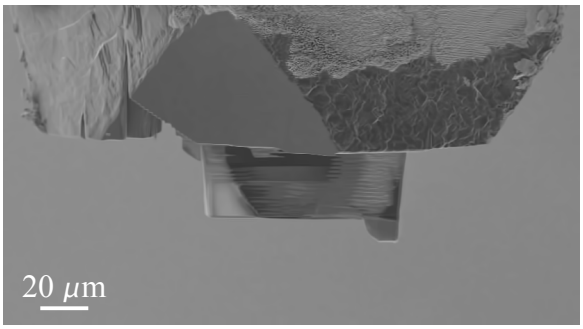

Figure 2.4: SEM image of the diamond flat punch indenter tip used during *in situ* micro-compression testing after focused ion beam milling from a conical tip geometry.

2.3 Characterization of Micromechanical Testing System

An understanding of the testing instrumentation is a necessary precursor to performing experiments, as knowledge of the measurement limitations guides experimental design and enables proper data collection. Compression tests were mostly carried out in an Agilent Nanoindenter G200 system using the XP head (comes from 'explorer'). The XP head was used as opposed to the DCM (dynamic contact module), which is also available on the testing instrument. While the DCM head is characterized by superior load resolution and displacement control, because the DCM it is limited to a maximum travel distance of 30 μm (and is really only intended for half of that) full compression of the samples is impossible and it is not used in testing. The XP head essentially consists of a electromagnetic loading cell, loading column, leaf springs, capacitive displacement gauge, and indenter tip all mounted within a stiff loading frame. A schematic of the relationship between these parts is shown in Figure 2.5. The leaf springs support the column while load is applied through the inductive coil/magnet assembly, making the system inherently load controlled. Displacement is measured via the capacitor with a zero raw displacement, u_{raw}, position being defined at the center of the capacitive range. Raw displacement can vary between -700 and $+700$ μm and is determined with a claimed resolution of 0.01 nm. (This claimed resolution is actually the nanometer per volt resolution of the capacitive displacement gauges for the most restrictive gain value. Actual displacement resolution, due to noise, is around

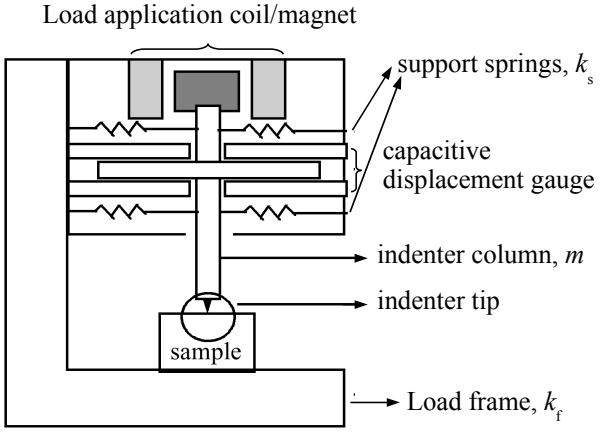

Figure 2.5: Schematic of the Agilent Nanoindenter G200 XP head.

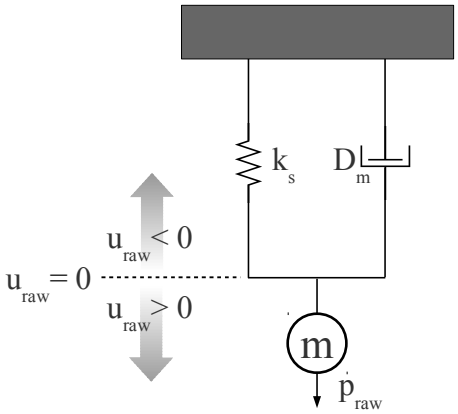

Figure 2.6: Simple harmonic oscillator model of the Agilent Nanoindenter G200 XP head

1 nm.) Load can be applied up to 500 mN with a claimed resolution of 50 nN, far beyond the capabilities needed for these experiments.

By design, the XP head can be modeled as a simple harmonic oscillator as shown in Figure 2.6. In this illustration, k_s refers to the spring constant associated with the loading column and attributable to the leaf springs, D_m is the damping constant of the machine, largely due to air resistance, and m is the mass of the loading column plus the indenter tip (mostly the column). With the assistance of with a SURF student, Pearl Fung, k_s, D_s, and m were calculated for our system following the procedure in Hay et al. [27]. Briefly, this involves oscillating the indenter head with a constant amplitude sinusoidal load and measuring amplitude and phase shift, ϕ, associated with the resulting sinusoidal displacement, all while holding the indenter head at a fixed u_raw. The magnitude of the load and displacement oscillations are referred to as the harmonic load, p_h, and harmonic displacement, u_h, respectively. We gathered u_h and the ϕ for a series of frequencies, f, from 1 to 40 Hz and at a series of u_raw from -30 μm to $+90$ μm. From this the dynamic stiffness, $C_\mathrm{h} = p_\mathrm{h}/u_\mathrm{h}$ is calculated. Finally, k_s, D_s, and m are used as fit parameters for the C_h versus f data in the simple harmonic oscillator relation [27].

$$C_\mathrm{h}^2 = (k_\mathrm{s} - m\omega^2)^2 + (D_\mathrm{m}\omega)^2. \tag{2.1}$$

Here, $\omega = 2\pi f$, is the angular frequency in radians. Figure 2.7 shows a typical fit taken

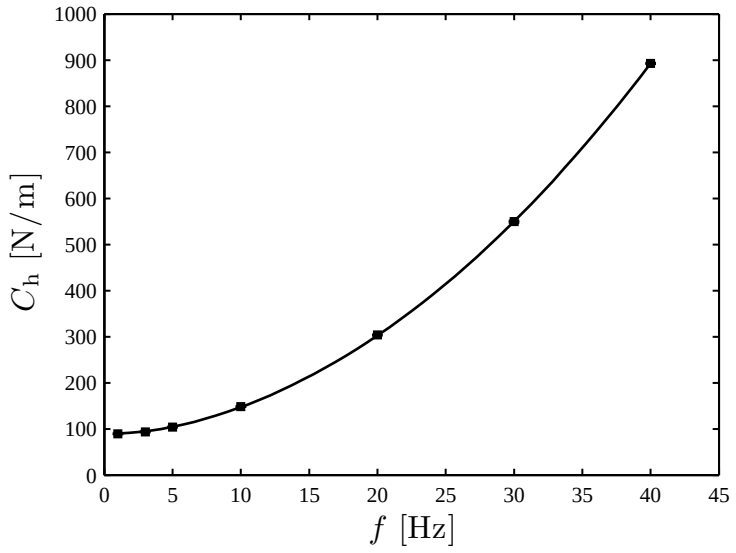

Figure 2.7: Characterization of the XP head using the simple harmonic oscillator model described by Eq. (2.1) for $u_{\mathrm{raw}} = 0$. Error bars (from four measurements) lie within the markers. The fit is denoted by the solid line.

at $u_{\mathrm{raw}} = 0$ μm, which illustrates the validity of the simple harmonic oscillator assumption. In order to fully understand the system, this test was repeated for a series of raw displacements. A summary of the variation in fit parameters obtained as a function of position, u_{raw}, are given in Figs. 2.8, 2.9, and 2.10. Our results reveal that the system is most consistently behaved in the range of 0–60 μm raw displacement. Thus, experiments are performed within this region in order to obtain the cleanest testing results. Significant changes in the spring constant within this region point to the need to fully account for the machine response, particularly when testing requires a large amount of travel by the indenter head and/or when the stiffness of the sample being characterized is on the same order of magnitude as the machine stiffness, k_{s}. These changes arise from the inherent non-linearity of a real spring. It is for this reason the test methods described in Sections 2.4 and 2.5 perform characterizations in air along with testing the sample.

The frequency range of 1–40 Hz used to characterize the XP head was motivated by the determination of the cut-off frequency for our system. The cutoff frequency, defined by Herbert et. al. [28] is the frequency beyond which crosstalk and/or phase rotations from other modes of vibration contribute to the measured response in a manner that is no longer effectively modeled by a simple harmonic oscillator. The frequency at which this occurs

can be determined through a plot of the phase angle, ϕ, the degree by which the oscillatory displacement response lags the load excitation, versus frequency, f. The cutoff frequency is defined at the point where a discontinuity in the phase angle occurs. A plot of $\phi(f)$ (Fig. 2.11) reveals that the cutoff frequency for our system is approximately 50 Hz. Thus, in performing any viscoelastic characterization of our materials, as through the methodology described in Section 2.5, we only utilize frequencies that adhere to the assumption of a simple harmonic oscillator, i.e., those below 50 Hz.

2.4 Microcompression Testing Methods

One of the major reasons for performing uniaxial compression tests is that the load-displacement data gathered during testing can be readily converted into nominal stress and strain in the axial direction. However, before this simple calculation can be performed, the p_{raw} and u_{raw} must be separated into sample and machine contributions. In this section, the microcompression experimental procedure is described for performing testing in the XP module of an Agilent Nanoindenter G200 and how the corrected load versus displacement response for the sample only is extracted from the raw data. These procedures are unusually impor-

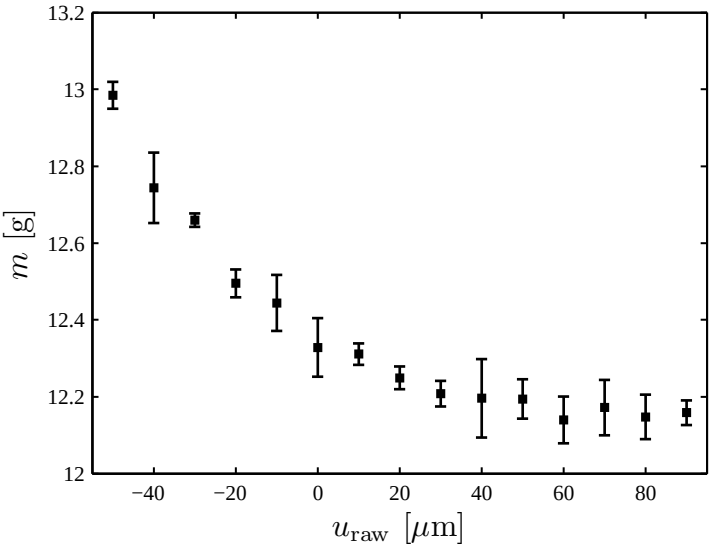

Figure 2.8: Indenter head mass, m, as a function of raw displacement, u_{raw} obtained from the fit of a simple harmonic oscillator model. Error bars were generated from the fit of four separate frequency sweeps at each u_{raw}.

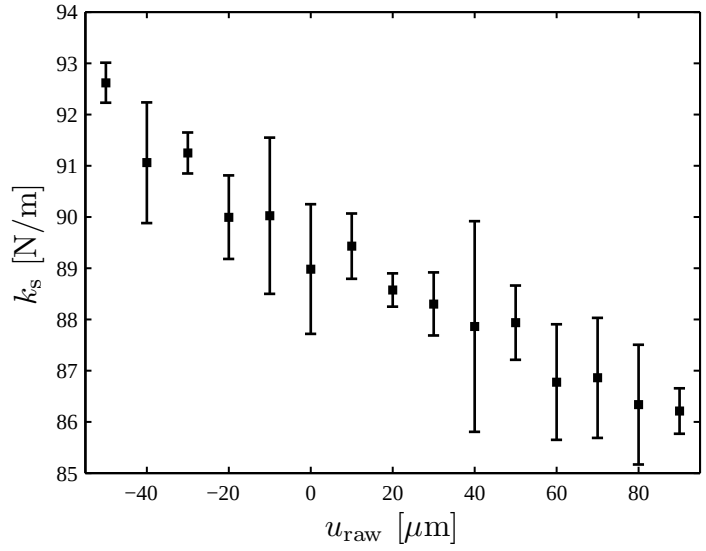

Figure 2.9: Machine stiffness, k_{s}, as a function of raw displacement, u_{raw} obtained from the fit of a simple harmonic oscillator model. Error bars were generated from the fit of four separate frequency sweeps at each u_{raw}.

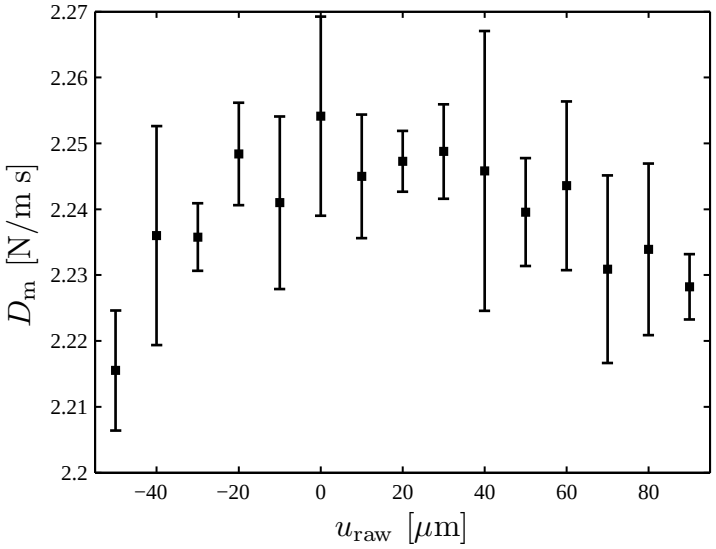

Figure 2.10: Machine damping, D_{m}, as a function of raw displacement, u_{raw} obtained from the fit of a simple harmonic oscillator model. Error bars were generated from the fit of 4 separate frequency sweeps at each u_{raw}.

tant for soft materials like VACNTs as the testing apparatus' contribution to the overall response is significant. Other experimental hurdles, also related to VACNT's high compliance, were also overcome and are described in this section. Testing methods are discussed with respect to the software accompanying the G200 which is called Testworks.

2.4.1 Setting the Sample Up for Testing

Once an array of VACNT pillars has been grown using the methods described in Section 2.2.1.1 or milled using the FIB as described in Section 2.2.1.2, the pillar plus substrate is mounted on a stiff 'sample puck' using carbon paint (PELCO Colloidal Graphite, Ted Pella, Inc.) and loaded into the G200 sample tray. Typical microscope to indenter calibration, microscope focal length/sample height, and surface find techniques as described in the G200 user's manual and applied in the default testing methods are not applicable here due the stickiness and compliance of VACNTs and the geometry of the diamond flat punch indenter tip.

The procedure for bringing the sample to the appropriate height for testing differs from the manual as follows. To get the sample at a height suitable for mechanical testing (i.e., such that testing occurs within the well-behaved range of raw displacement values determined in Section 2.3), a soft polymer sample is first mounted on either a separate puck or the same puck as the VACNT sample. Both PDMS and nail polish were used for this other sample which will subsequently be refered to as the calibration sample. The calibration sample must be soft so that during a microscope to indenter calibration, the large flat punch makes a discernible mark to calibrate against. In the case where the calibration sample is

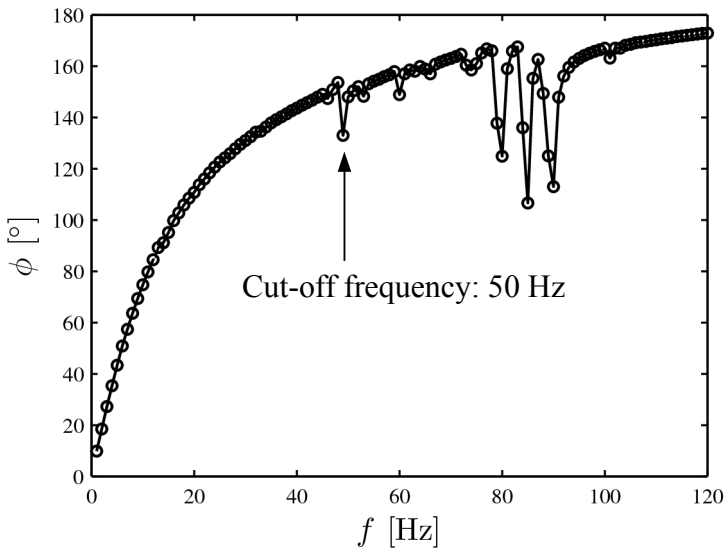

Figure 2.11: A plot of the phase angle versus the frequency of load excitation indicating the location of the cutoff frequency.

mounted on the same puck as the VACNT sample, the surface of both sample and calibration sample must be as close as possible to the same height. In the case that they are mounted separately, the microscope is brought into focus over the fused silica reference sample as described in the G200 user's manual [29] before moving the calibration sample under the microscope. The sample is brought into focus manually (without using the microscope motor). A Microscope to indenter calibration reveals the 'Raw Displacement' of the surface of the calibration sample. If this is a large number ($>$100 μm) the calibration sample must be raised 'Microscope to Indenter Calibration' and the process repeated until the 'Raw Displacement' when the surface is found is under 100 μm but greater than 20 μm. (The first calibration is likely to occur at a very large raw displacement if the flat punch described in Section 2.2.1.3 is used, as it is much shorter than a standard tip.) Now the calibration sample is near zero 'Raw Displacement', the correct height for testing. The microscope focus motor is used to bring the microscope into fine focus on the calibration sample before moving the test sample under the microscope. With the test sample visible under the microscope, the sample puck is raised and lowered manually until it is in focus. Now the sample is at approximately the correct height for performing mechanical tests. The reasons for this procedure are that the calibration sample and the test sample must be at the same height in order for the calibration to be sufficiently accurate and both must be near zero 'Raw Displacement.'

Now that the sample is in place, we perform an accurate identification of the surface of the pillar. Without this point, there is no reference for determining the correct load on the sample or displacement into the sample. Traditional Testworks surface find test segments do not work with VACNTs due to their high compliance (surface is 'found' much later than physical contact is made with the surface due to lack of sensitivity) and stickiness (VACNTs can be transfered onto the indenter tip when in contact and can be carried along from the rough initial surface find to interfere with the actual testing position of interest). From the procedure in the preceedign paragraph, it is known that the surface of the sample to be tested is in the 'Raw Displacement' range between 0 and 100 μm. A series of tests is begun by manually seting a surface approach displacement of 0 μm. The surface is approached at a slow to intermediate speed (on the order of 100 nm/s). As the surface is approached, a

small oscillation is applied to the indenter column ($p_{\mathrm{h}} = 10$ μN) and the harmonic contact stiffness is monitored by the software. The harmonic contact stiffness measures the elastic part of the dynamic stiffness, C_{h}, and is corrected within the software for the machine contribution using a set of tables determined during calibration and setup. Therefore, it hovers near 0 ± 15 N/m typically and depending on the amplitude of the oscillation can easily detect changes on the order of 50 N/m, which is the threshold we used for surface determination in these experiments. Because of the relatively high speed of the first test, it must be discarded. However, now the 'Raw Displacement' of the VACNT sample is known and is entered as the surface approach starting point along with a slow surface approach speed for all subsequent tests. Note that if the 'Raw Displacement' is > 100 μm both the test and calibration samples are raised and the 'Microscope to Indenter Calibration' process is repeated to avoid misalignment between the tip and pillar. Further details of the test method are given in Appendix A.

2.4.2 Decoupling Material and Instrumental Response

As the raw load versus raw displacement data collected during nanoindentation experiments combines both the material and instrumental responses, careful measures have to be taken in order to accurately decouple the sample-only response and the machine response. This is accomplished through properly modeling the mechanical equivalent of the entire sample-instrument system [30–32]. The equivalent mechanical model of the nanoindenter plus sample for the system of relevance is shown in Fig 2.12. Raw load data (p_{raw}), determined by the inductive loading coil, and raw displacement data (u_{raw}), gathered by the capacitive displacement gauge (see 2.3), are gathered continuously (250–500 Hz) throughout the test. After a successful surface find, the test of interest is performed, typically a constant displacement rate loading followed by unloading. After compressing the pillar, the indenter is held in the air at several characterization points within the raw displacement range accessed during compression to accurately determine the spring force and machine damping constant throughout the range of displacement in which data was gathered (see Appendix A for detailed method implementation). The load required to maintain these displacements is the column spring force, p_{s}, (a result of the load necessary to deform the

leaf springs of stiffness, k_{s}, shown in Fig. 2.12), which is slightly position dependent over large distances (enough to result in a 0.05 mN force difference over some regions of raw displacement, which is around 0.1% of the total load obtained). Post-processing (not in Testworks) interpolates between the values of p_{s} taken at 10 locations within the displacement regime and uses this information to remove p_{s} from p_{raw} at every time point. Finally, there is a small contribution to the force by the machine damping (D_{m}), which is calculated during the post-test characterization in air. However, this latter contribution is marginally important for only the highest strain rates, $\dot{\epsilon}_{\mathrm{n}}$, tested (displacement rates, $\dot{u}$) of 0.1 and 0.5 s^{-1} where the force, $D_{\mathrm{m}}\dot{u}$, is on the order of 0.05 mN. The resulting equation for the corrected load on the indenter tip/load frame/sample assembly (solid boxed region of Fig. 2.12), p_{corr}, is therefore

$$p_{\mathrm{corr}} = p_{\mathrm{raw}} - p_{\mathrm{s}} + D_{\mathrm{m}}\dot{u}. \tag{2.2}$$

It follows that the load on the sample is simply the load on this assembly due to the fact that these three elements are in series. The corrected displacement (u_{corr}), i.e., the actual displacement applied to the sample, accounts for the deformation in the load frame (frame stiffness, k_{f}) and the diamond indenter head (stiffness, k_{i}). Again, since the sample, frame,

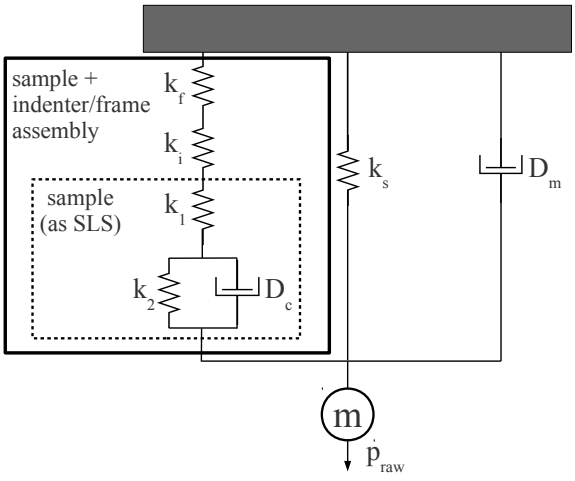

Figure 2.12: Viscoelastic model of the nanoindenter plus sample system utilized to obtain the correct load on the sample from the measured load, p_{raw}. For most calculations, the sample (inside the dashed box) can be treated as a black box. The standard linear solid model for the sample is only utilized in the application of the method of Wright, et al. [31] for determining storage and loss stiffnesses to be discussed in Section 2.5.

and indenter head are in series (Fig. 2.12), the corrected displacement can be written as

$$u_{\text{corr}} = u - \frac{p_{\text{corr}}}{k_{\text{f}}} - \frac{p_{\text{corr}}}{k_{\text{i}}}, \tag{2.3}$$

where k_{f} for our system is 5.92×10^6 N/m (calculated during instrument setup and calibration) and k_{i} is calculated from the known elastic modulus, E_{D}, and Poisson's ratio, ν_{D}, of diamond. The relationship for determining k_{i} is [30]:

$$k_{\text{i}} = \frac{2E_{\text{D}}}{(1-\nu_{\text{D}}^2)\sqrt{A_{\text{i}}/\pi}}, \tag{2.4}$$

where A_{i} is the cross-sectional area of the indenter area in contact with the sample. Both corrections turn out to be inconsequential (~ 0.01 nm) for such a compliant material under such large deformation. Additional corrections could be imagined for the compliance of the Si wafer on which the pillar sample is mounted or the carbon paint attaching the wafer to the puck, but, as is evident from the corrections for frame and indenter tip compliance, these would be minor, on the scale of random noise in the displacement signal.

As discussed in detail in the previous section, surface contact is marked by attaining a 50 N/m threshold in the harmonic contact stiffness, as a threshold any lower than that has been found to result in a significant number of false positives for surface contact due to the mechanical and electrical noise. It is important to recognize that crossing this threshold represents the initial contact, likely caused by several stray tubes or a slight misalignment between the flat pillar surface and flat punch rather than by full cross-sectional contact; full contact usually occurs within 0.5 μm of raw displacement from that point. Upon establishing contact, the harmonic measurement option can be turned off before proceeding with the compression. For the results in Section 4.2 this was done due to the fact that the indenter head cannot be oscillated fast enough to provide meaningful data at the faster displacement rate used. We identify the first attainment of full contact in post-processing by locating the first occurrence of a tangent slope in the p_{corr} versus u_{corr} data of 10 N/m in order to have a consistent surface threshold for all tests. This value corresponds to a marked increase in p_{corr} relative to the maximum load attained in the quasi-static tests. Utilizing the correct location of the sample surface, the actual load and displacement felt by the pillar is tared at

that point for a zero stress zero strain initial value. It should be noted that, p_{corr} is already approximately zero at this point, being less than 0.04 mN while the maximum p_{corr} approaches 40 times this value providing verification that our surface find and data correction procedures are accurate.

In the experiments described in this thesis, the nanoindenter compresses the samples at a constant, prescribed raw displacement rate ($\dot{u}_{\mathrm{raw}}$), and therefore a constant nominal sample strain rate, throughout the entire experiment (loading and unloading). Examples of the instrument's response to the prescribed displacement rate schedules are shown in Fig 2.13.

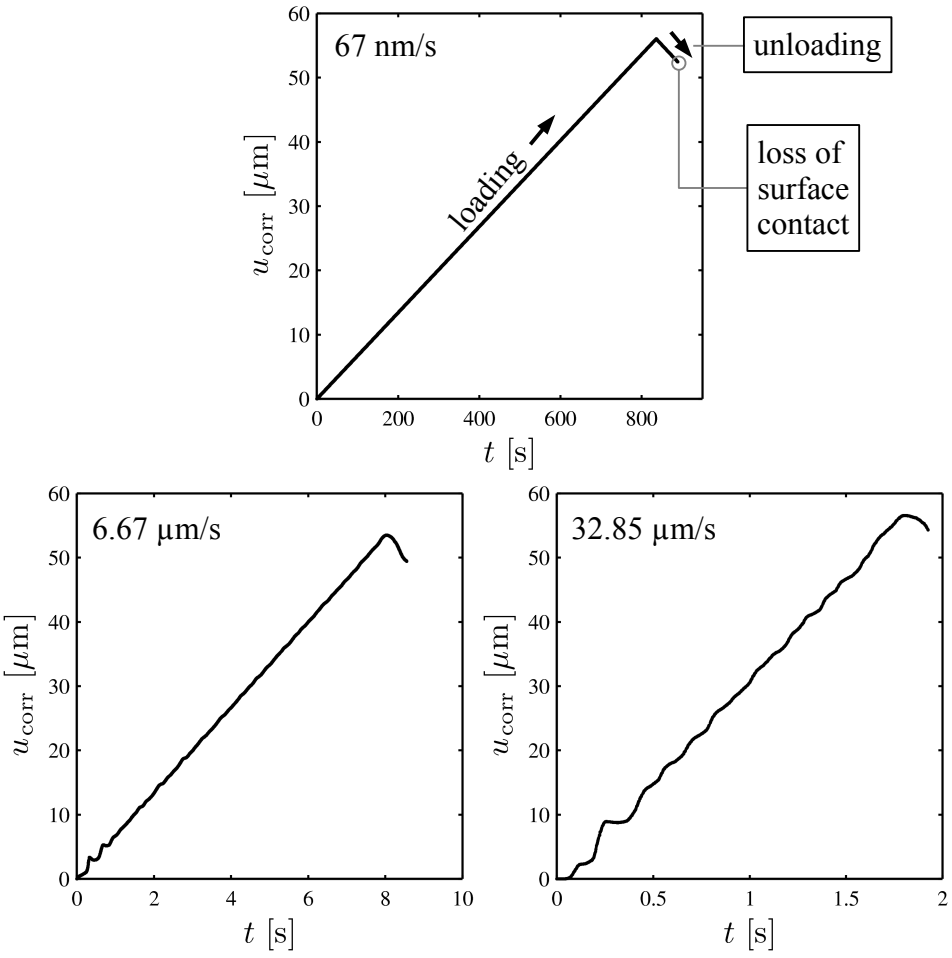

Figure 2.13: Typical loading schedules for 67 nm/s and 667 nm/s (not shown but identical) (top), 6.67 μm/s(bottom left), and 32.85 μm/s(bottom right) constant displacement rate compressions. The loading schedule for the slowest rates (top) illustrates the near ideality of control. Loading schedules for the fastest rates used (bottom) show nominal rate control, but illustrate the rate-limited control of the equipment. The unloading segment in all curves is short due to early loss of contact with the surface of the deformed sample.

Recall from Section 2.3 that the G200 is inherently load controlled, which means that constant displacement rate tests invoke the use of proportional control with limits on maximum and minimum loading rates. During a constant displacement rate uniaxial compression, the loading schedule, $u_{\mathrm{corr}}(t)$, where t is time, is ideally a straight line with slope equal to the prescribed rate. The displacement schedules for the two slowest rates we utilized have nearly perfect control (straight lines), while the two fastest rates show a progressive decrease in control, illustrating the limitations of the inherently load controlled nanoindenter. The maximum percent errors associated with the prescribed displacement rates used were $2\times10^{-3}\%$ for the slowest rate and 0.25% (up to 0.4% for beginning of unload) for the fastest rate. These are very minor errors and the tests can be assumed to be constant strain rate.

2.4.2.1 Compression Method Details

The complete method utilized in the microcompression of VACNT pillars is given in Appendix A. General highlights and features of note from that method are as follows. The top surface of the pillar is detected by setting the initial approach speed to $\sim$50 nm/s while oscillating the indenter head at a fixed harmonic load (resulting in $\sim$30 nm amplitude) at 25 Hz while waiting for the harmonic stiffness to exceed the 50 N/m threshold. The oscillation is then turned off, and the test begins by loading at the prescribed strain rate to a prescribed depth. At the peak load, a short hold (on the order of three time constants of the capacitive displacement gauge, $\sim$0.003 ms) allows the displacement gauge to recover from any offset that may have occured between the real-time and reported raw displacement position, if necessary. The pillar is then unloaded at the same prescribed displacement rate until the displacement becomes less than the displacement at the surface. Surface contact is generally lost before this point is reached. After compressing the pillar, the test method runs the series of holds in air starting at the raw displacement of the pillar surface and going to the full compression depth.

2.5 Microscale Dynamic Testing Methods

Dynamic testing methods, in which samples are subjected to oscillatory loads or displacements, are typically used in the characterization of viscoelastic materials. These materials exhibit both viscous/ energy-dissipating and elastic/energy-storing characteristics when subjected to load. Viscoelastic behavior is generally quantified in terms of the storage, E', and loss, E'', moduli which are the real and complex parts, respectively, of the complex modulus (or by the ratio, $\tan\phi$, of these two moduli). The modulus, however, is not the most fundamental measurement of the viscoelastic response. It is calculated from the harmonic stiffness, C_{h}, which is the ratio of the harmonic load and displacement amplitudes, $p_{\mathrm{h}}/u_{\mathrm{h}}$. Conversion between harmonic stiffness and complex modulus is accomplished through the well known Sneddon relation, [33]

$$E = C_{\mathrm{h}}\frac{\sqrt{\pi}}{2\beta}\frac{1-\nu^2}{\sqrt{A}}, \tag{2.5}$$

and requires knowledge of a material's Poisson's ratio, ν; unmeasured for VACNTs. It is for this reason I calculate only storage and loss stiffnesses rather than storage and loss moduli in characterizing the viscoelastic properties of VACNTs. In Eq. (2.5), β is a constant that depends on the indenter geometry (1 for a flat punch) and A is the contact area ($\sim$2,500 $\mu\mathrm{m}^2$).

In a typical dynamic testing experiment, the material is loaded to a desired strain and the mechanical probe is oscillated across a range of frequencies. By measuring the resultant load amplitude, displacement amplitude, and the phase lag during the test (following the methods outlined in Herbert et al. [28] and Wright et al. [32]), the values of loss stiffness (k_{loss}) , storage stiffness (k_{storage}), and $\tan\phi$ are determined. This method is identical to the dynamic mechanical analysis (DMA) of polymers, but occurs at a much smaller scale in terms of both oscillation amplitude and sample size. Specifically, I gather the storage and loss stiffnesses by oscillating the indenter head at $\sim$8 nm amplitude while sweeping the frequency from 1 to 45 Hz while holding the nominal strain constant at 10 values: from 0.01 to 0.8.

Briefly, the procedures and calculations described in Herbert et al. [28] and Wright

et al. [32] prescribe removal of the machine contribution by performing a second set of measurements in air (at the same raw displacement). Therefore, the storage and loss moduli for the sample/frame assembly are written

$$k_{\text{storage}} = \left|\frac{p_{\text{h}}}{u_{\text{h}}}\right| \cos\phi - \left|\frac{p_{\text{h}}}{u_{\text{h}}}\right|_{\text{air}} \cos\phi_{\text{air}}, \tag{2.6}$$

$$k_{\text{loss}} = \left|\frac{p_{\text{h}}}{u_{\text{h}}}\right| \sin\phi - \left|\frac{p_{\text{h}}}{u_{\text{h}}}\right|_{\text{air}} \sin\phi_{\text{air}}. \tag{2.7}$$

Here the subscript 'air' refers to the measurements taken while the head oscillated in air (i.e., not in contact with the sample). While this method treats the entire sample/frame assembly as a black box, a positive aspect of this treatment is that these stiffnesses remain independent of the indenter mass. This is important as values calculated for the indenter head mass utilize several assumptions and can be somewhat variable as shown in Section 2.3. It is reasonable to assume that stiffnesses calculated via Eqs. (2.6) and (2.7) correspond to those of the sample since both the frame and the indenter head stiffnesses are several orders of magnitude higher than those of the sample and thus can be assumed to be infinite [28]. It should be noted that a channel in Testworks referred to as the 'Harmonic Contact Stiffness' is essentially equivalent to k_{storage}. The only difference in this instance is that I characterize the behavior of the indenter head in air each time I perform a test and the 'Harmonic Contact Stiffness' channel uses tabulated values for the stiffness in air used in Eqs. (2.6) and (2.7). For highly compliant materials, characterization after each test yields more accurate results. The Testworks method utilized in this thesis for dynamic mechanical analysis is detailed in Appendix B.

2.6 *In Situ* Testing Setup

In this instance, an *in situ* testing setup is one in which the quantitative response of a sample is gathered simultaneously with a morphological response, in this case micrographs. The Greer group *in situ* instrument, SEMentor [34], performs this task through a combination scanning electron microscope (SEM) and nanomechanical testing arm (nanoindenter). From it we can learn, by observation, what deformation events correspond to unique signals

in the data, thus it is our 'mentor.'

Samples to be tested are mounted on a 90 degree SEM stub and loaded into the SEM chamber at a tilt of 4 degrees from vertical. The mechanical testing arm is mounted on a side port of the SEM (FEI Quanta 200) at an angle of 4 degrees from the horizon. The geometry is illustrated in the schematic in Figure 2.14 with photos of the actual system given in Figure 2.15. The mechanical arm is a derivative of the technology in the DCM head of the Agilent Nanoindenter G200 and is therefore subject to the same limitations. The first limitation is in the raw displacement which ranges from -15 to $+15$ μm. Also, maximum attainable load is 10 mN with a resolution of 50 nN. The maximum load is sufficient for our tests, but because of the limited raw displacement, *in situ* testing of 60 μm tall VACNT pillars is limited to nominal strains of only 50%.

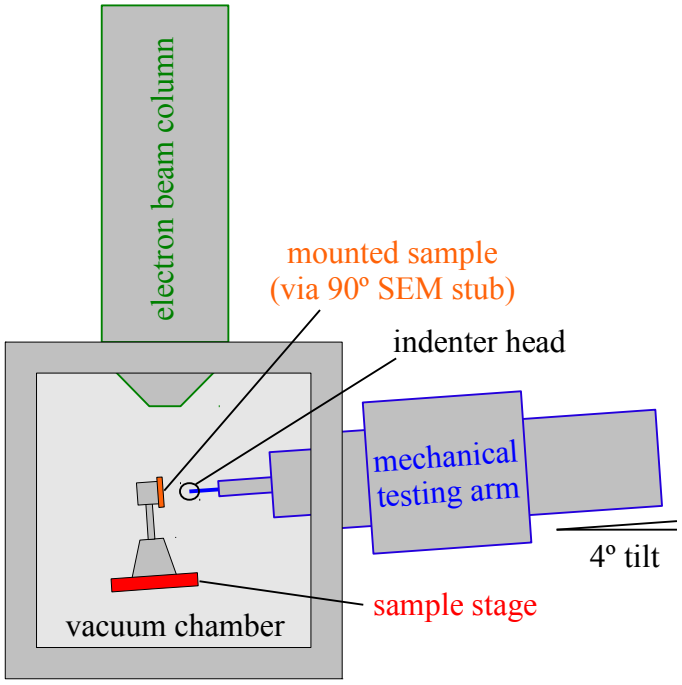

Figure 2.14: Schematic of the *in situ* testing instrument, SEMentor.

Load versus displacement data obtained in the SEMentor is analyzed slightly differently from that gathered in the G200. This is for two reasons. First, characterization of the DCM head is more difficult due to the proprietary nature of its exact geometry. Second, an accurate quantitative measurement is unnecessary as SEMentor is most beneficial as a visualization instrument. Therefore, raw load and displacement are corrected using the

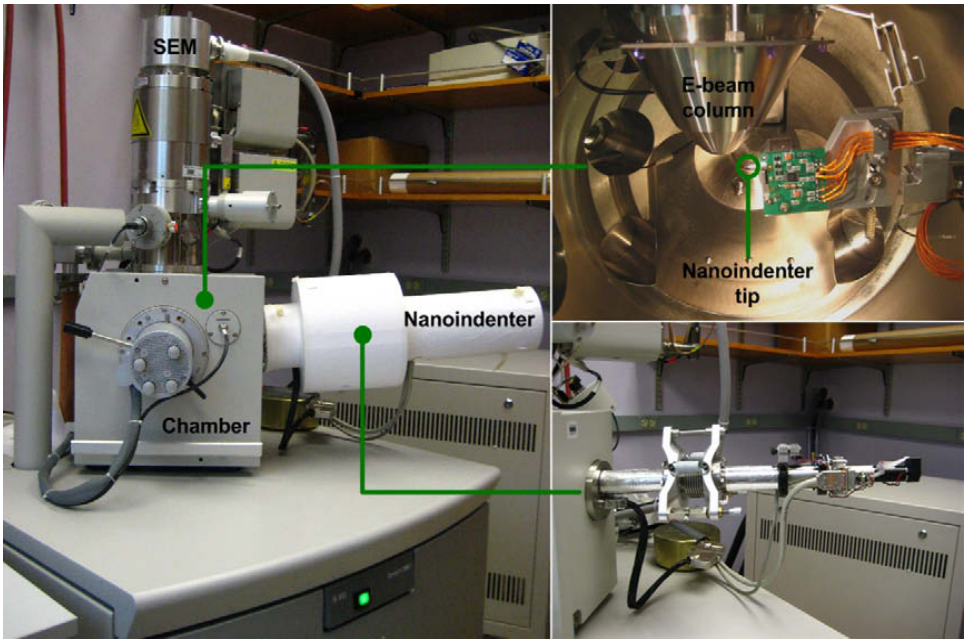

Figure 2.15: Photo of the *in situ* testing instrument, SEMentor [34]. The image on the left is the complete system with the mechanical testing arm shielded from environmental influences. The image on the upper right is a few inside the SEM chamber. The image on the lower right is the nanomechanical testing arm before shielding has been installed.

'Support Spring Stiffness' channel, which is a table of leaf spring stiffness values as a function of raw displacement, $k_{\mathrm{s,table}}(u_{\mathrm{raw}})$, obtained during a calibration run. This data is quite noisy, so the channel must be collected during the *in situ* compression, smoothed, then removed from the applied load yielding an approximate load on sample,

$$p_{\mathrm{corr}} = p_{\mathrm{raw}}(u_{\mathrm{raw}}) - p_{\mathrm{raw,surf}} - (u_{\mathrm{raw}} - u_{\mathrm{raw,surf}})k_{\mathrm{s,table}}(u_{\mathrm{raw}}), \tag{2.8}$$

where the subscript 'surf' refers to value at the point of surface contact. This correction is necessary because of the large position dependence of $k_{\mathrm{s,table}}$, which would otherwise overwhelm the sample response.

Chapter 3

Characterization of VACNT Morphology

3.1 Introduction

The specific microstructure of VACNT structures plays a key role in their mechanical response. This has been found qualitatively for a range of structures obtained through slight variations in growth by McCarter et al. [16] as well as being evident in the range of moduli reported in the literature (see Table 4.1). This chapter overviews some characteristic morphological aspects of the CNT bundles tested as well as the methodologies used to obtain these properties. Several key features set VACNTs apart from other materials. As stated earlier, the structures are hierarchical. That is, under lower magnification ($\sim$1,000$\times$), the tubes in the bundles appear vertically aligned, i.e., perpendicular to the substrate (Fig. 1.2, left). However, under larger magnifications ($>$ 30,000$\times$), it becomes evident that the CNTs are randomly oriented in a very porous network, forming a fibrous, interconnected web of support structures, where individual tubes interact with one another (Fig. 3.1, left and right). The presence of these interactions is the distinguishing attribute of this type of VACNT material in contrast to vertically aligned CNT 'forests,' in which individual tubes are far enough apart (and short enough) to grow perpendicularly to the substrate without interacting with their neighbors. Second, there exists a height-dependent inhomogeneity in the bundle structure due to its growth mechanism [35]. Visual inspection indicates there is a lower density of tubes with less vertical alignment at the bottom. This, in turn, results in fewer and weaker load bearing members at the bottom and therefore a more compliant material in this region of the pillar. These microstructural gradients are illustrated in the

high magnification SEM images taken of the pillar surface at evenly spaced heights along the pillar axis in Fig. 3.1. Quantification of this gradient has only been reported for high energy synchrotron measurements of bulk CNT films as they grow [35], a method that is both expensive and inapplicable to our sample geometry. For this reason, in Section 3.2 I discuss the image analysis techniques developed to analyze this relative density gradient directly from the SEM micrographs. These techniques are developed in collaboration with Peter Capak of the Spitzer Science Center at Caltech.

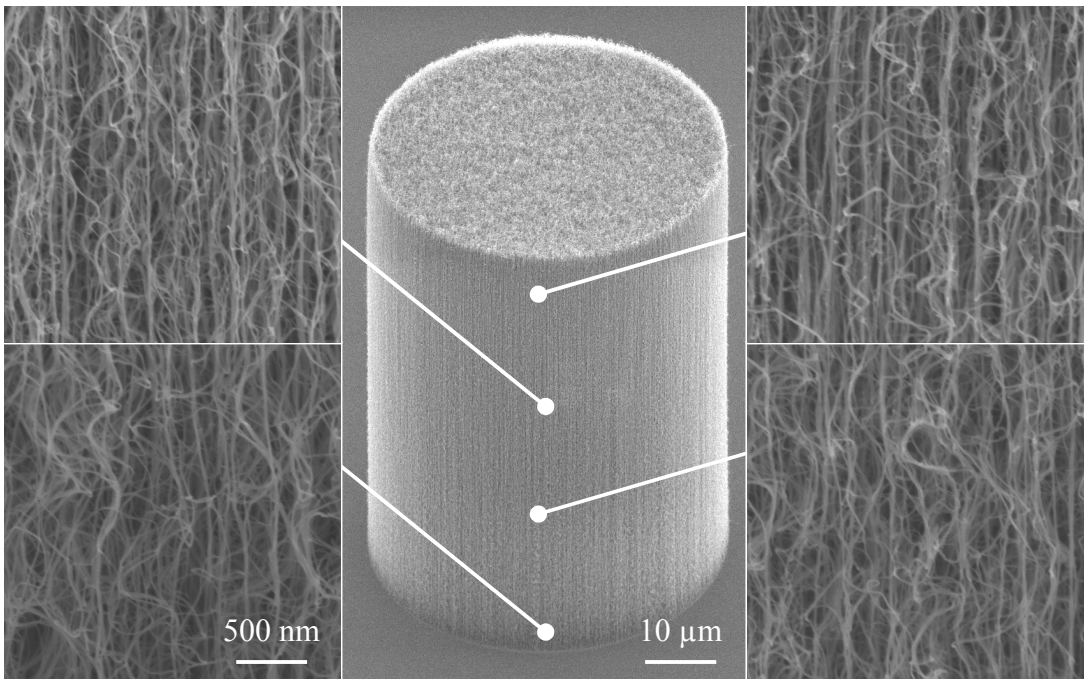

Figure 3.1: Cylindrical pillar with $32,000\times$ magnification insets, revealing the highly inhomogeneous CNT microstructure from bottom to top. The lower leftmost image corresponds to the bottom of the pillar and illustrates the sparser (less dense) and less vertically aligned CNTs when compared to the top of the pillar (upper rightmost image). Note that the surface tubes appear brightest because they return more signal to the electron detector, but these tubes are not indicative of the internal pillar microstructure and should be looked beyond in order to observe the density and alignment variation discussed.

Other important microstructural elements are the makeup of the individual CNTs themselves and the average density or porosity of the structure. Presently, there appears to be some link between tube diameter (number of walls) and/or the surface roughness of CNTs on the presence of irrecoverable versus recoverable deformation behavior [36], but this connection remains to be rigorously proven. In the present work, individual CNTs

were characterized by transmission electron microscope (TEM) (see Fig. 3.2). Diameters are found to vary between 15 and 30 nm with 22 nm being the average value. The tubes themselves are multiwalled, typically comprised of 4–5 walls per tube. Average density is clearly an important feature in comparing the mechanical response of any foam-like material. For example, the elastic modulus of a foam scales with the relative density squared for foamed metals and polymers [23], where relative density is the foam density divided by the density of a single, monolithic strut. Similar relationships exist for energy dissipation and plateau stress. Unfortunately, determining either the average tube number density or mass density has proven challenging due to the small size of individual pillars (lack of material for bulk measurement) and the large amount of open space (small surface area per gram of sample). Attempts to determine the density of the samples tested are discussed in Section 3.3.

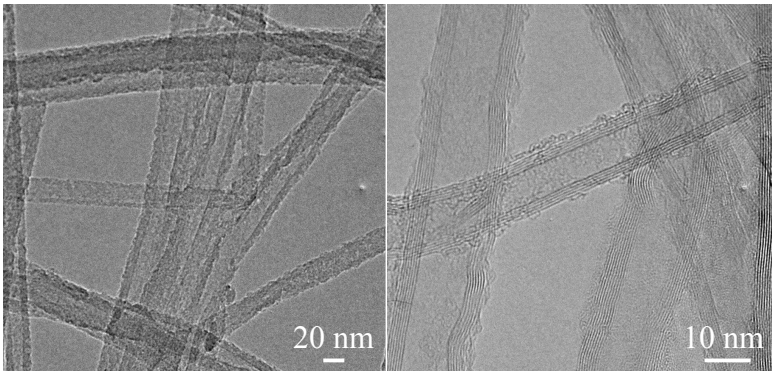

Figure 3.2: TEM images illustrating the typical multiwall CNTs making up the VACNT bundles tested. There are typically 4–5 walls per tube. Images taken by A. T. Jennings.

3.2 Density Gradient

VACNTs grown via CVD are suspected to have a tube number density gradient in the direction perpendicular to their growth substrate. This gradient is supported by *in situ* small angle x-ray scattering (SAXS) experiments during growth [35] as well as qualitatively by the visual inspection of several series of high magnification SEM images taken along the height of the VACNT film (see Fig. 3.3). As described by Bedewy et al. [35], the density gradient arises from the fact that the CNTs are formed via base growth. This means that as

catalyst is lost during the growth process (carried away by the tubes themselves or diffused into the substrate) less CNTs are being produced. The CNTs that have already been grown, however, are carried/pushed away from the substrate as new CNTs continue to form and grow. Knowing the gradient in number density that arises from this growth process is cen-

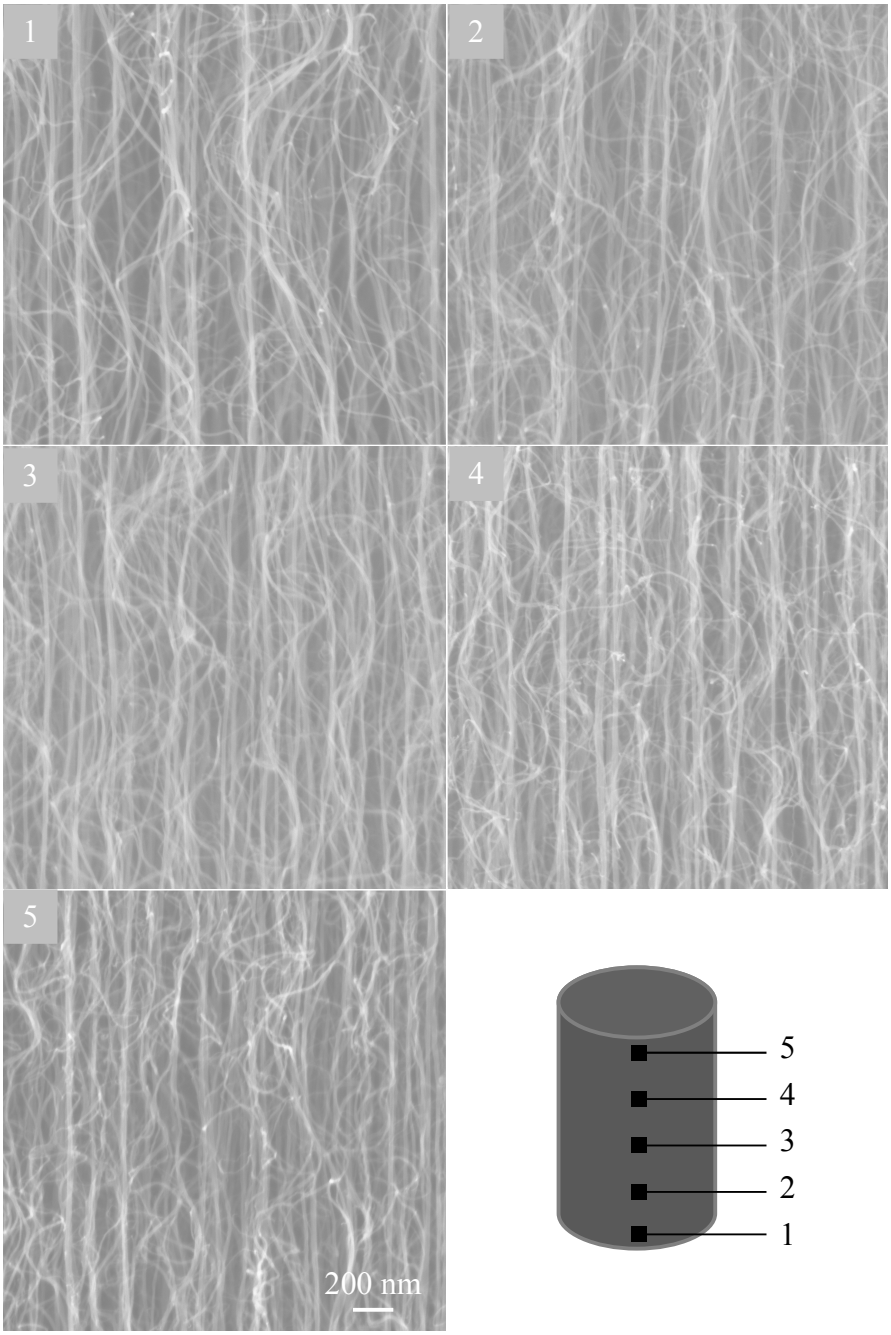

Figure 3.3: A series of SEM images at distances of 1) 5 μm 2) 15 μm 2) 25 μm 2) 35 μm and 2) 45 μm away from the growth substrate captured from the side of a 50 μm tall VACNT pillar.

tral to understanding the overall structural material response of the VACNTs under load. It is also necessary in order to separate that overall response from the local material response.

SEM images are relatively easy data to acquire for any VACNT system regardless of density, tube diameter, or size of the film. For this reason, I have made efforts to analyze several series of images (a single series corresponds to a set of images along the height of the CNT pillar) in order to quantify the *relative* density differences between them. Note that an absolute density cannot be obtained from an SEM image in this case as the interaction volume is unknown. In fact, calculation of the interaction volume is extremely complicated due to the porous nature of VACNTs. In attempting to differentiate the number of tubes between two micrographs, the issue of image normalization becomes apparent. Thresholding, in which all pixels above a given saturation value are made white and all those below are made black, appears at first to be the most straightforward way to determine the number of tubes in an image [37]. However, the images do not have the same contrast or brightness values as these values were manually tuned along the height of the pillar in order to retain information (i.e., the same brightness and contrast settings at the bottom of the pillar would result in a completely black image at the top). Therefore, the threshold must be set for each individual image, a non-trivial task in which it is difficult to deconvolute the brightness and contrast of an image's histogram from the tube density contribution to the histogram. Briefly, brightness is defined as overall saturation of an image or where it falls on the grayscale from 0 to 255. Contrast is roughly defined as the breadth of the image histogram; approximately the maximum pixel value less the minimum pixel value. A typical SEM micrograph with its corresponding histogram are given in Figs. 3.4(a) and (c). Based on the wide variation in brightness and contrast observed between experimental images, it can be concluded that the images must be either normalized with respect to both or a method must be found that is insensitive to these image properties while still being sensitive to the structure found within an image.

Image analysis utilizing the methods discussed here is heavily used in the astronomical sciences (e.g., [38] and [39]), biological sciences (e.g., [40]) and medical sciences (e.g., [41]). The knowledge and methods developed in these fields is utilized to customize a method for quantifying grayscale images of fibrous materials. In order to check the va-

lidity of a method throughout its development, A series of simulated tube images having characteristics analagous to the experimental images is generated. Once these simulation

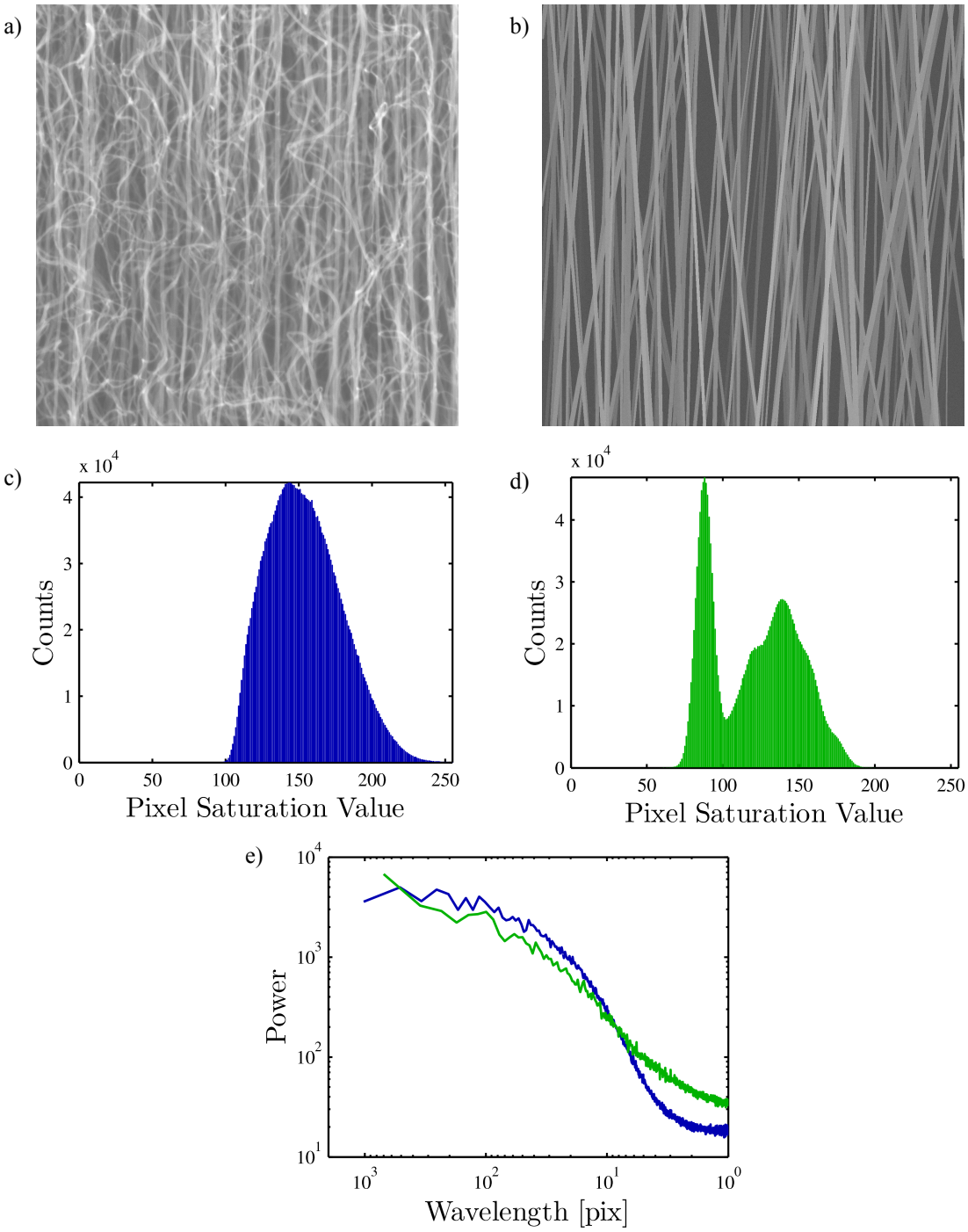

Figure 3.4: Typical experimental and simulated CNT microstructure images with their corresponding histograms and power spectra **a)** SEM image **b)** Simulated image **c)** Histogram for the image in a) **d)** Histogram for the image in b) **e)** Radially averaged power spectra for a) (blue) and b) (green).

images produce meaningful trends for a given method, limitations of the image analysis technique can be explored through controlled deviations from the experimental characteristics. Subsequently, a figure of merit corresponding to the relative increase in tube number can be developed. For this reason, key features of the experimental SEM images must be measured.

3.2.1 Experimental Image Characterization

Careful measurement of the tube diameter, image noise, and relative tube and image saturation values is performed. Tube diameters are measured by hand/eye using the software ImageJ. The resulting distribution of diameters is given in Fig. 3.5(a). The data is more reasonably fit with a log-normal distribution than a Gaussian. The average tube diameter is

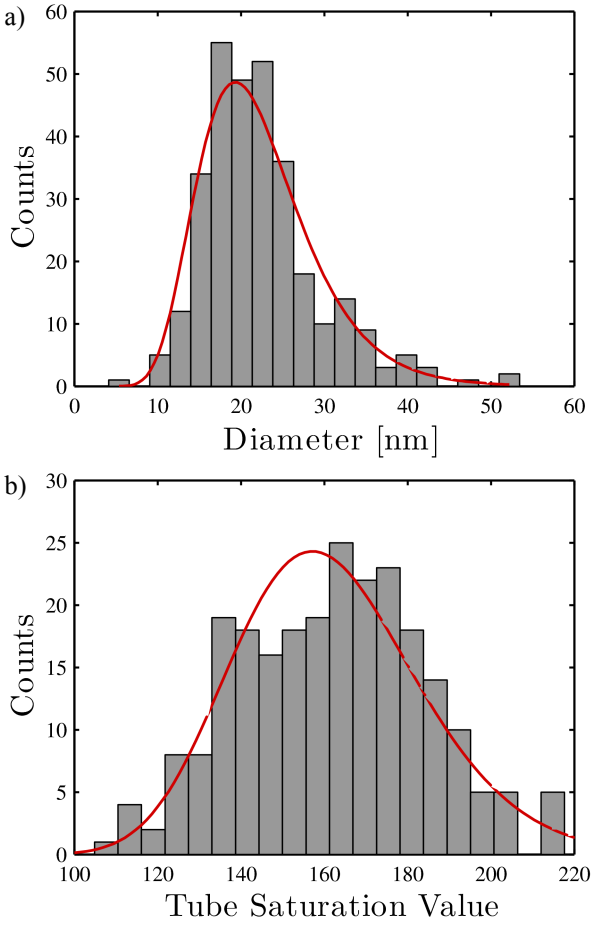

Figure 3.5: **a)** Distribution of tube diameters with superposed log-normal fit. **b)** Distribution of tube saturation values with superposed Gaussian fit.

22.3 nm with a mode of 21.1 nm and log-normal standard deviation of 0.31. Analagously, tube saturation data is gathered by taking the average value from a region of each of the tube encountered while progressing horizontally across an image. This data is presented in Fig. 3.5(b) and fit with a Gaussian distribution having a mean of 162 and standard deviation of 22 (out of a scale from 0 to 255). As each of these data analyses are tedious and many data points were collected, they were performed for only one experimental image. It is reasonable to assume that tube diameter is not changing significantly (and indeed does not appear to do so) between images. The standard deviation of tube intensity or saturation value will certainly change with image contrast, but, as stated earlier, that must be accounted for in the method deveoped. The most important attribute to bear in mind for tube intensity is that it has a Gaussian distribution and thus this will be a key feature of the simulated images.

Image noise is measured by calculating the standard deviation of pixel values within a relatively homogeneous subregion of the image. It is found to increase slightly with increasing local intensity which is expected. This is because the noise can likely be characterized as shot noise, i.e., due to the finite nature of the electrons interacting with the detector, which is proportional to the square root of the mean saturation or intensity of a pixel. The average noise (taken as the standard deviation of the pixel saturation values) for the SEM images is 0.02 ± 0.005. This value is not a function of the height at which the image is taken. Implementation of the characteristic tube diameter, brightness distribution, and noise in a series of simulated images is given in Appendix D. A typical simulated image and its corresponding histogram are shown in Figs. 3.4(b) and (d).

3.2.2 Pattern Extraction with the Power Spectrum

One measure of spatial variation in an image can be determined by taking its Fourier transform. When the Fourier spectrum is averaged radially (with the center of the image corresponding to zero frequency and the outermost corresponding to the single pixel frequency) the result is a measurement of the average variation in the image between any two pixels at any given spacing known as the radially averaged power spectrum. The radially averaged power spectrum has several notable properties. First, the overall brightness of an image has no effect on it. Only the relative variation affects the power (i.e., contrast). Second, it

contains no absolute position information, only relative position information. Thus, it can be used to measure the presence of structure at a certain lengthscale in the image. Typical power spectra obtained for experimental and simulated images are shown in Fig. 3.4(e). By convention, small wavelength or spatial scale is on the right and corresponds to pixel to pixel variation. The power at this lengthscale generally reflects the contrast of the image. However, I have found that it is also convolved with the tube number density and therefore cannot be used to normalize the power spectra between multiple images. Note that the power signal rises sharply around a wavelength of 10 pixels, which corresponds to the approximate diameter of an average CNT.

Using the power spectra, one can explore changes in power response to changes in the image's characteristics. Two series of simulated images (having characteristics similar to the experimental images as determined by the data presented in Section 3.2.1) are generated such that the contrast (and brightness, though it has no effect on the power spectrum) of each image was identical:

S1: 10 sets of 11 images - linear variation in line number from 50 to 150

S2: 10 sets of 11 images - no variation in line number, 100 lines in each

As hoped, the first series of images shows an increase in power at the wavelengths corresponding to average line width (10 pixels in this case) while series S2 shows no increase in power. The increased response in power is demonstrated in Figure 3.6(a) through a plot of the ratios of the power spectra. Each ratio is calculated with respect to the average spectra for the images with the lowest line number (50 lines). Therefore, large deviations from one indicate areas in which more structure is present. Note the largest change occurs between approximately 7 and 11 pixels. Taking the average power between 7 and 11 pixels for each set of images having a given number of lines results in the plot in Figure 3.6(c). The graded set shows an increase in power with image number while the non-graded set remains constant. Note that the error bars taken from the variation in response between the 10 sets of images demonstrate that the increased response is minimal and, in fact, appears to saturate at line numbers that are most representative of the experimental images ($\sim$100). Therefore, I conclude that the power spectrum alone is unlikely to provide us with the sensitivity

required to measure changes in the amount of fibrous structure within these experimental images, particularly within the tube number range of interest.

Additionally, when the same methods are used on a series of images in which the brightness and contrast of the simulated images is varied randomly, all correlation is lost. This

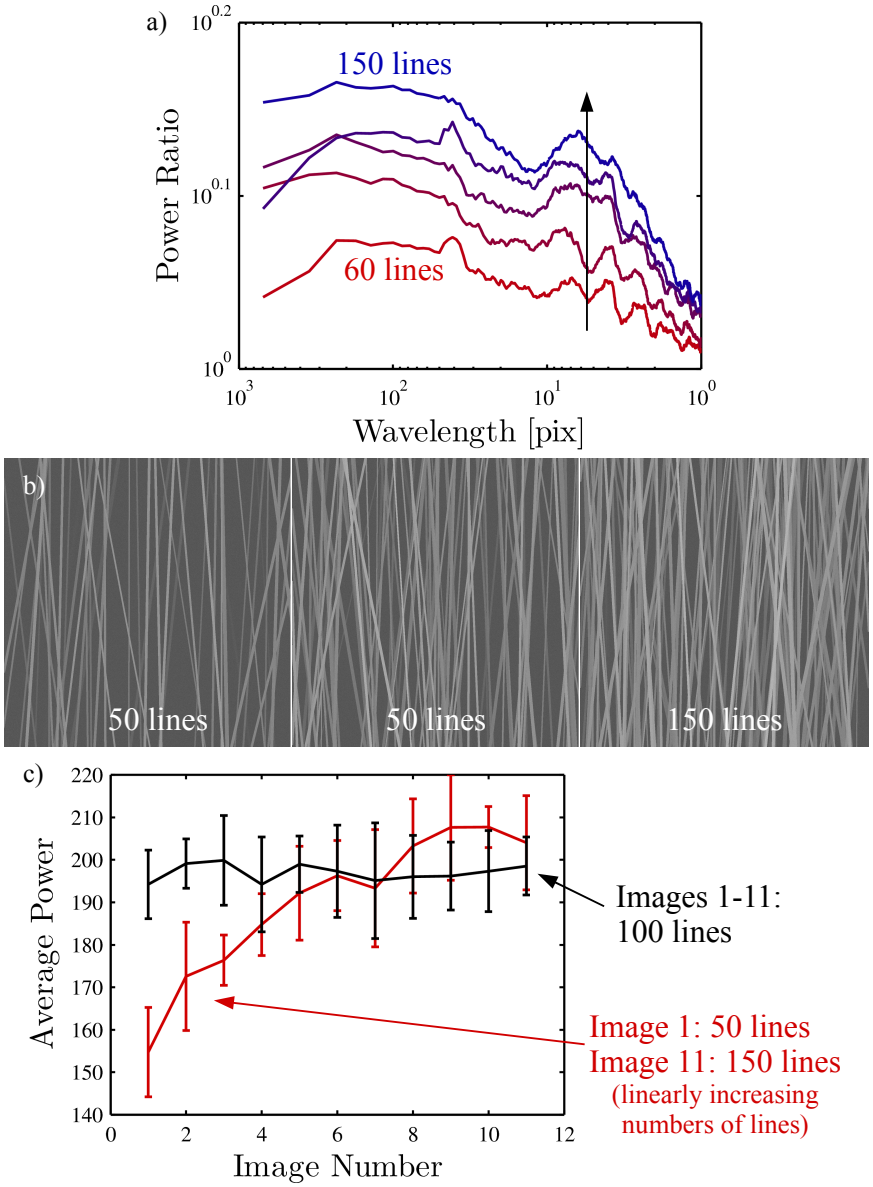

Figure 3.6: Summary of results obtained from using the radially averaged power spectra alone to quantify the number of lines in simulated images. **a)** Ratio of radially averaged power spectra to the average spectra for an image with 50 lines for a series of simulated images. **b)** Example simulated images having (from left to right) 50, 100, and 150 lines. **c)** Average power values as a function of image number for graded and non-graded sets of simulated images.

is because the contrast in the images has not been normalized. As a result, several contrast regularizing techniques were attempted: normalizing by the shortest wavelength, normalizing by the gain, and normalizing by the contrast as determined by the image histogram. At this time, a correct or experimentally feasible normalizing procedure has not been found.

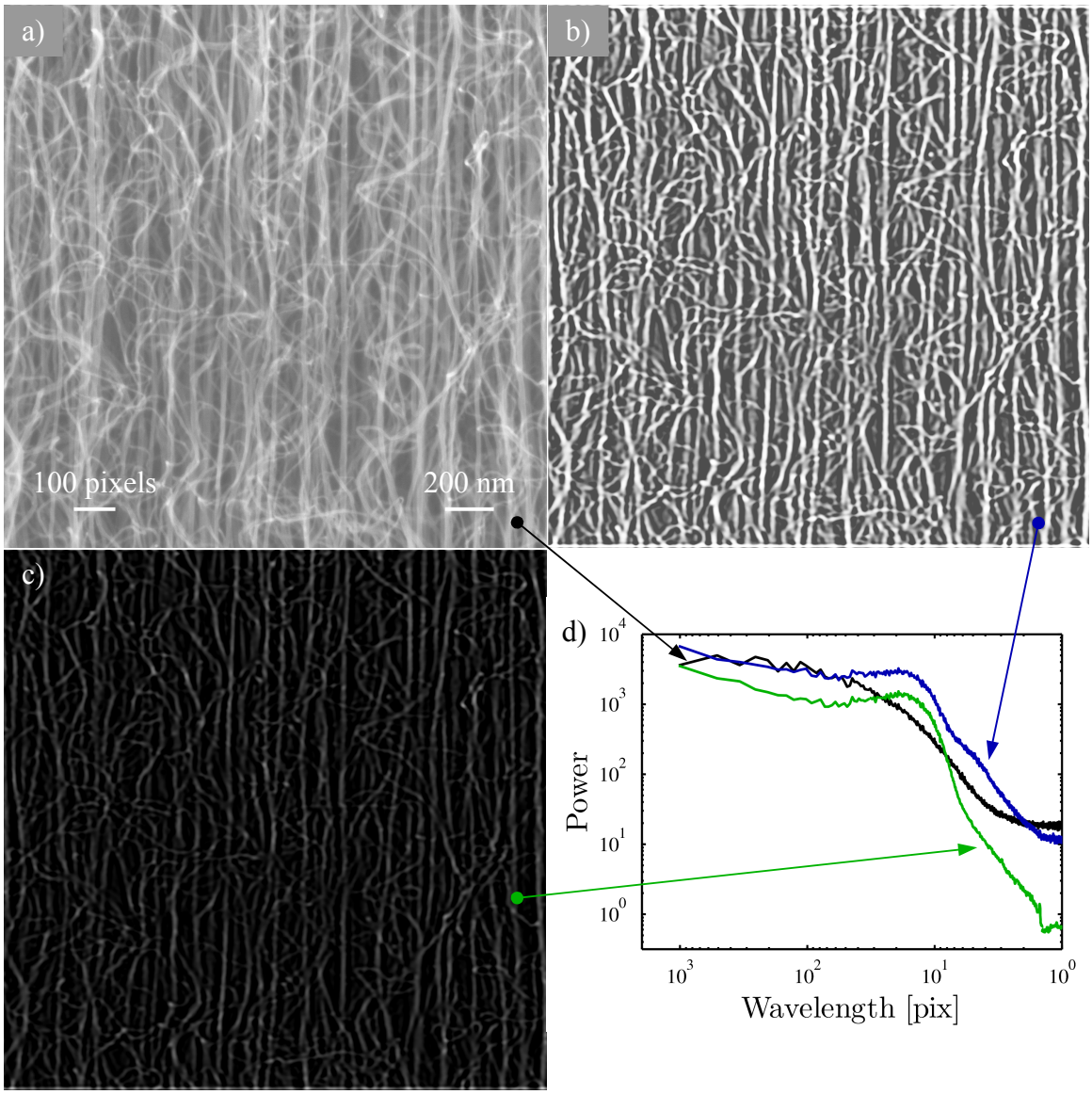

Figure 3.7: **a)** Original micrograph image. **b)** Filtered micrograph after histogram equalization. **c)** Filtered micrograph rescaled to high contrast for viewing. **d)** Radially averaged power spectra for images in a), b), and c).

3.2.3 Edge Detection

Another typical image analysis method generically known as 'segmentation' involves locating edges or objects of interest within an image. One issue with a typical edge find technique can be finding edges at lengthscales that are not of interest or missing edges due to changes in contrast either locally or between images when a threshold is set inappropriately. Since the region of the power spectrum corresponding to signal from the tubes is known, we can mitigate these issues by first filtering the image in the frequency domain with respect to this lengthscale. This results in an image in which the structure of interest is brought to the forefront. An example of a Gaussian bandpass filtered image in which a histogram normalization procedure has been performed to highlight the remaining structure is shown in Fig. 3.7(b). For reference the high contrast, but otherwise unaltered filtered result is shown in Fig. 3.7(c). Corresponding radially averaged power spectra in Fig. 3.7(d) verify the emphasis on the tube-scale structure present in the filtered image. Future efforts will be focused on the appropriate selection of filter and subsequent edge detection method in order to develop a method that is robust under changes in both contrast and brightness between images while giving resolution in line number density.

3.3 Material Density

It is generally taken for granted that a material's density and volume fraction, in the case of porous materials, can be easily obtained. For nanoscale and nanostructured materials however, this is not always true. Our VACNT pillars are both. In bulk specimens of VACNTs the density, ρ_{VACNT}, and volume fraction of tubes, ϕ_{CNT}, can be readily measured using a mass balance, the volume of the weighed sample, V_{total}, and the known density of graphite, $\rho_{\mathrm{graphite}} = 2.2$ g/cm^3, via the relations,

$$\rho_{\mathrm{VACNT}} = \frac{m}{V_{\mathrm{total}}}\phi_{\mathrm{CNT}} = \frac{m/\rho_{\mathrm{graphite}}}{V_{\mathrm{total}}} = \rho_{\mathrm{VACNT}}/\rho_{\mathrm{graphite}}. \tag{3.1}$$

Measurements of other VACNT samples grown via CVD methods (not the samples grown for and tested in this thesis) put these values around 0.1 g/cm^3 and 0.05, respectively. How-

ever, the size of our VACNT pillars does not allow for such simple techniques. A 1 cm $\times$ 1 cm continuous film of VACNT having a height similar to that of the VACNT pillars tested here (60 μm) weighs only 0.66 mg. This is not feasibly measurable on a typical lab scale and requires measurement using a high sensitivity mass balance, such as that used in thermogravimetric analysis (claimed resolution of $\sim$1 μg). To complicate things, the weight of the Si substrate on which the samples are grown is several orders of magnitude larger, making the sample's removal from the substrate necessary for measurement. Practical limitations make this undesirable: The sample is destroyed and brittle flaking occurs to such an extent that the VACNTs cannot be completely harvested. For this reason, we attempted to utilize a technique commonly applied to highly porous materials, nitrogen adsorption, following the Brunauer-Emmett-Teller (BET) theory for analysis of the results.

Briefly, BET theory is a multilayer extension of Langmuir theory, which is itself a theory for monolayer molecular adsorption of gas onto a surface. Measurements of the amount of gas adsorbed onto the sample surface at a given supersaturation combined with known quantities of the size of the gas molecule result in the ability to perform a calculation of the surface area of a sample. Systems capable of BET measurements typically require samples having a surface area of 0.1 m^2 to $\sim$300 m^2, e.g., catalyst materials like zeolites or adsorbants like activated carbon. Once a surface area measurement is obtained, an estimate of the porosity, given average values for the average inner, $d_i \approx 7$ nm, and outer, $d_o \approx 20$ nm, radii of the CNTs (combined with the assumption that N_2 adsorption occurs on both the inner and outer surfaces), can be calculated via the relation

$$\phi = \frac{d_o^2 - d_i^2}{d_o + d_i} \frac{A_{\text{surface}}}{4V_{\text{total}}}. \tag{3.2}$$

This estimate is still sensitive to measurements of the sample volume, but determination of the mass has been eliminated. Unfortunately, for a 1 cm $\times$ 1 cm $\times$ 60 μm sample with an estimated volume fraction of 0.05 (from bulk), one can only expect surface areas of $\sim$0.1, which are at the low end of the measurement capabilities for the N_2 adsorption instrument available. Even loading the BET instrument with 3 times this sample volume, we found that fits of adsorption data to the BET theory were poor. Thus, estimates of the surface area of our samples obtained in this way were unreliable. Due to the challenges associated with

determining the density of these highly porous and microscopic structures, very few reports contain these quantitative measurements, particularly as a function of specific location on the sample. Most reports in the literature estimate the density based on tube counting in samples cleaved from the surface or mass density measurements of bulk samples. Density measurement remains an unresolved issue.

Chapter 4

Deformation Under Uniaxial Compressive Loading

4.1 Introduction

While much work has been done to study the unique properties of individual CNTs and CNT-composite materials, only a few reports addressing the mechanical deformation of VACNTs, as defined in this thesis (see Chap. 1), exist. These published studies have measured the mechanical properties of VACNTs through nanoindentation [14, 16, 42, 43], uniaxial compression [13, 15, 20, 24, 44, 45], impact testing [21, 22], and across a wide range of temperatures [19]. Variations in observed behavior and quantitative results in these publications illustrate the wide variety of growth conditions that can, in turn, result in significant dissimilarities in the mechanical properties including deformation morphology, the amount of post-deformation recovery, the elastic modulus, and the amount of energy absorption and dissipation. Table 4.1 summarizes the variation in elastic moduli that have been reported from a variety of testing geometries. Some of this variability has been addressed qualitatively in terms of the visible differences in tube morphology by McCarter, et al. [16]. Despite the quantitative property differences, VACNTs have been observed to exhibit a common and intriguing structural behavior. Post-compression SEM images indicate sequential, coordinated buckling, evidenced by wavy surface morphology. In previous reports buckling appeared to initiate preferentially from the substrate side of the structure, regardless of whether the CNTs are attached to it during the course of deformation [24]. This sequential, coordinated buckling was observed by Yaglioglu for VACNT bun-

dles compressed in an SEM using an Omniprobe [46]. Many of the qualitative descriptions we observe here were reported, however, the mechanical probe had no load or displacement sensors such as characterize our *in situ* testing setup. Some of these materials display a high recoverability after significant strain, even after cyclic loading [24], while others have been observed to deform permanently [15, 44, 46]. This thesis explores the largely irrecoverable deformation we observed upon uniaxial compression of the VACNT bundles. The results presented within this chapter were first published in Hutchens et al. [44].

Uniaxial microcompression experiments were selected as the mechanism for studying the mechanical properties of VACNTs for reasons of simplified analysis as well as for the fact that a free surface allows for observation of the rich morphological response characterized by sequential, periodic folds or buckles as we will refer to them hereafter. While nanoindentation tests on VACNT films [14, 42] and on photolithographically defined features [15, 16] have provided tangent and elastic moduli, they cannot explore this wrinkle-like morphology due to its highly localized nature and the limited overall strain that can be analyzed in this testing geometry. In this chapter, we present our observations of the morphological evolution and corresponding mechanical response seen in cylindrical, 50 μm diameter CNT foam bundles subjected to uniaxial compression at different strain rates. We chose to test 50 μm diameter pillars with an aspect ratio of 2.4–2.8 (height/radius) because they are large enough to produce multiple surface undulations, as observed previously [15, 24], while being small enough to capture the local deformation events that occur during compression in our custom-built *in situ* mechanical deformation system, SEMentor [34] (see Section 2.6). Fortuitously, testing such small samples also enables resolution of the local buckling events within the overall stress-strain response, as will be shown in Section 4.2.

In addition to the quasi-static response of the VACNTs, we also characterize their viscoelastic response as a function of excitation frequency. Several studies have characterized the energy dispersive capabilities of these materials [14, 19, 20, 24, 47]. They find that, after multiple loading/unloading cycles (not including the initial few cycles), the energy dissipation and recovery remain approximately constant (up to 5×10^5 cycles [20]). Most notably, studies presented in a recent article by Xu et. al. [19] found that some VACNTs

dissipate energy at twice the amount of silicone rubber and do so at a wide range of temperatures (-196–1000 °C) over which typical viscoelastic materials, such as polymers, either harden or degrade. The specific VACNT materials we tested do not undergo the kind of reversible deformation that would allow them to act as an alternative to rubber. However, in Section 4.3 we present the results of a viscoelastic characterization of the VACNT pillars under increasing amounts of strain as part of an effort to understand the overall deformation mechanism.

Table 4.1: Table of Published Values for the Elastic Modulus of VACNTs

E (MPa)	**Measurement Method**	**Density**	**Reference**
50	Uniaxial compression	0.3 g/cm^3 [a]	Cao, et al., 2005 [24].
~ 50	DMA	NG	Mesarovic, et al., 2007 [42].
< 2	Uniaxial compression	NG	Suhr, et al., 2007 [20].
0.25	Uniaxial compression - loading	10^{10} cm^{-2} [b]	Tong, et al., 2008 [45].
15	Nanoindentation (Berkovich) - unloading	NG	Zbib, et al., 2008 [15].
18,000	Nanoindentation (flat punch) - loading	0.95 g/cm^3	Pathak, et al., 2009 [14].
~ 1	DMA	0.009 g/cm^3	Xu, et al., 2010 [19].
58	Nanoindentation (Berkovich) - unloading	NG	Zhang, et al., 2010 [47].
50 ± 25 [b]	Nanoindentation (Berkovich) - unloading	NG*	Qiu, et al., 2011 [43].

[a] Reported as an 87% porosity estimate, converted to approximate density using the density of graphite.

[b] Tube areal number density (20–30 nm diameter CNTs).

[b] Reported as a reduced modulus. Indentation was performed with a diamond tip, so difference from actual sample modulus is small.

* NG = not given

4.2 Uniaxial Results and Discussion

The mechanical response of individual pillars is analyzed through uniaxial stress-strain curves, post-mortem morphology, and *in situ* deformation videos. Four different nominal displacement rates were used: $\sim$ 65 nm/s, $\sim$ 0.65 μm/s, $\sim$ 6.5 μm/s and $\sim$ 32 μm/s, spanning just over three orders of magnitude of strain rate: 0.001 s^{-1}, 0.01 s^{-1}, 0.1 s^{-1}, and 0.5 s^{-1}. (The actual displacement rates varied with slight differences in initial pillar height, H, in order to keep the strain rate constant between tests.)

Nominal, or engineering, stress, σ_{n}, and strain, ϵ_{n}, were calculated using the initial radius and height of the pillar, R and H, respectively, along with the corrected load and displacement given in Eqs. (2.2) and (2.3) in Sec. 2.4.2.

$$\sigma_{\mathrm{n}} = \frac{p_{\mathrm{corr}}}{\pi R^2}, \tag{4.1}$$

$$\epsilon_{\mathrm{n}} = \frac{u_{\mathrm{corr}}}{H}. \tag{4.2}$$

A representative stress-strain curve (Fig. 4.1(a)) corresponding to the compression of a single CNT pillar at a rate of 0.001 s^{-1} illustrates the common features found at any of the measured strain rates. Utilizing a foam-like analogy, we first note three distinctive regimes: a short elastic region, followed by a plateau-like segment where the deformation is characterized by periodic 'humps' at a relatively constant overall applied stress, followed by stiffening indicating the onset of densification. While occurrence of these distinct types of mechanical behavior is typical for foams and other cellular materials [23], certain features are notable in the CNT bundle response: (1) the large initial buckling event marked by a significant load drop following the initial elastic deformation regime and (2) the series of distinct humps in the plateau-like segment that we will show correspond to the initiation and propagation of folding/buckling events that occur in the accomodation of deformation. A typical post-mortem image showing the multiple buckles or folds that form during compression is shown Figure 4.2(b).

Through *in situ* experiments, we discover that *sequential* (bottom - to - top), localized, periodic buckling governs bundle deformation. This is illustrated by the panels taken from

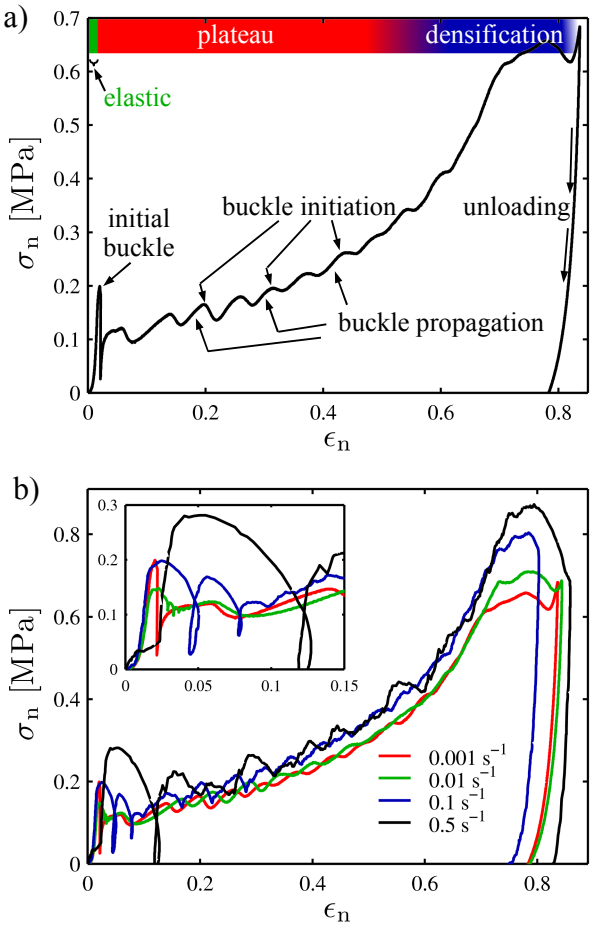

Figure 4.1: **a)** Typical stress-strain curve for uniaxial compression of a single bundle illustrating key features: i) the regions of elastic, plateau, and densification regimes (top ribbon), ii) the initial collapse peak, and iii) the characteristic humps throughout the plateau region and into densification corresponding to buckle initiation and propagation. **b)** A combined nominal stress-nominal strain plot for typical data taken at all four strain rates: 0.001 s^{-1} (thick solid), 0.01 s^{-1} (thick dashed), 0.1 s^{-1} (thin solid), and 0.5 s^{-1} (thin dashed). Hump magnitude increases with increased strain rate.

an *in situ* video (Fig. 4.3) at six regularly spaced strain/time intervals along the deformation curve and the embedded video in Fig. 4.4 (electronic version only). Cao et al. [24] hypothesized that the bottom-first buckling, hinted at by their observations of more compressed buckles at the bottom of the deformed samples than the top, was due to an inhomogeneity in material properties along the vertical axis. In particular, it has been shown that similarly grown VACNT materials exhibit a the density gradient (lower density at the bottom) and variation in the tubes relative vertical alignment (more aligned at the top) [35], which would lead to a much more compliant material near the substrate as compared to the top. Through

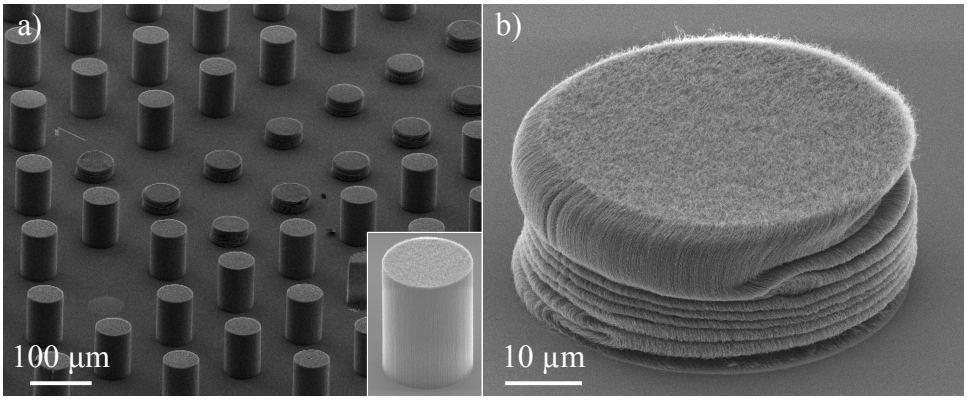

Figure 4.2: **a)** Array of compressed and uncompressed 50 μm pillars with inset showing a $1000\times$ magnified image of a single pillar. **b)** Typical buckled morphology present in a pillar after compression to $> 80\%$ strain and recovery to $> 30\%$ of its initial height (~ 67 μm).

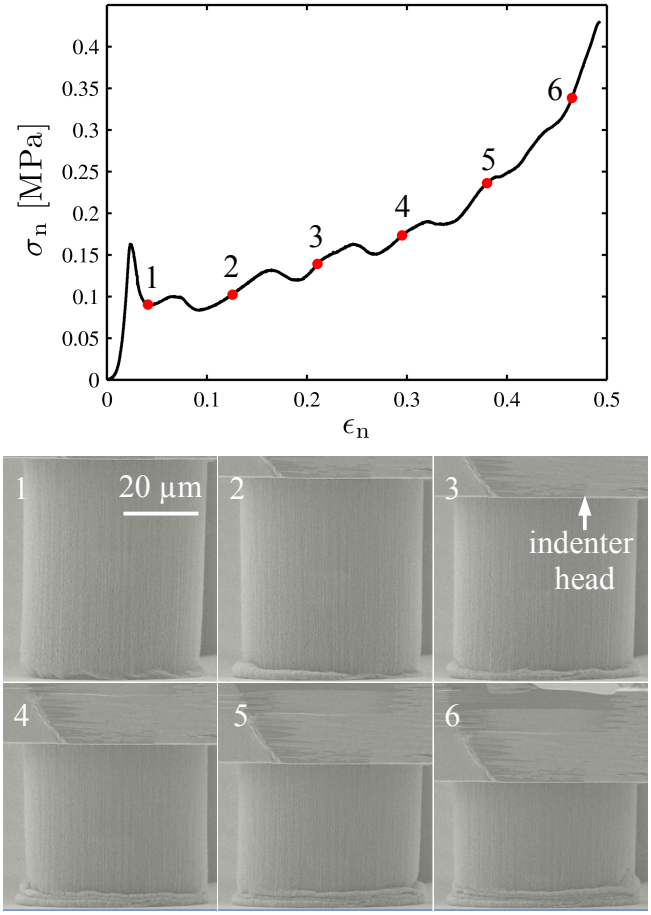

Figure 4.3: Frames from an *in situ* video illustrating the bottom-to-top sequential buckling. Each frame corresponds to the numbered six points denoted in the stress-strain curve (top), taken simultaneously with the images.

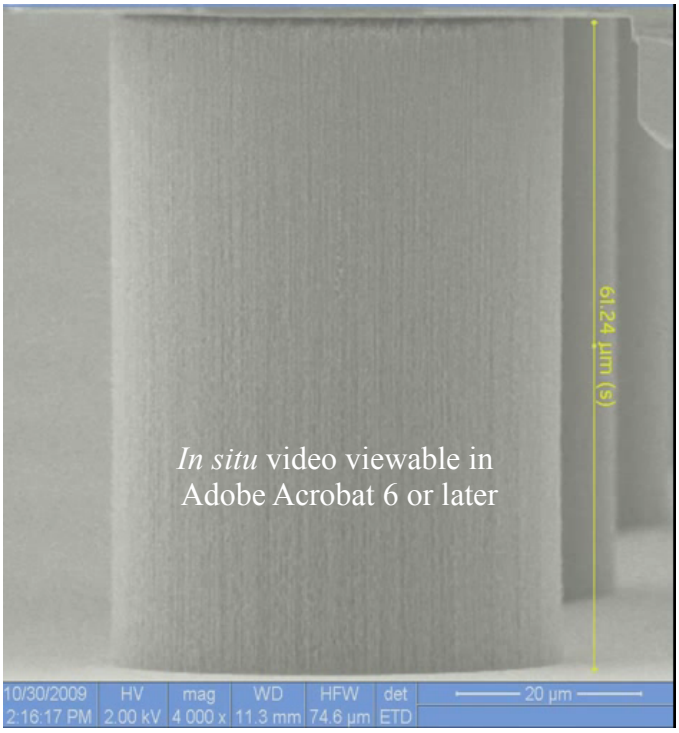

Figure 4.4: *In situ* video of a VACNT micropillar compression (electronic version only).

our *in situ* testing results we unequivocally demonstrate the deformation proceeding in a sequential manner. Specifically, we observe that, after the initial buckling, all subsequent buckled layers form in the following fashion: (1) buckles start as a localized fold or a bulge in the circumferential pillar surface, then propagate laterally (or possibly in a spiral) across the pillar diameter (Fig. 4.5), (2) buckles always form in succession, with each previous (lower) buckle fully completing before the initiation of the next buckle. As illustrated in Fig. 4.5, buckle initiaion corresponds to a sudden softening event, or drop in load, while propagation is characterized by local hardening in the stress-strain response. In addition, the entire pillar region above the buckles shows no signs of deformation, relegating all the strain accommodation to this buckling mechanism. We also observe that the wavelength of the post-compression undulations does not vary with changes in the strain rate. Instead, it remains at a relatively constant value of ~ 2 μm in all compressed pillars. As each 2 μm fold accommodates around 6 μm of unbuckled material, the final number of folds is simply a function of the total deformation only and thus also remains approximately constant over the strain rates tested.

We find that initial buckling is always more pronounced than all successive ones. It

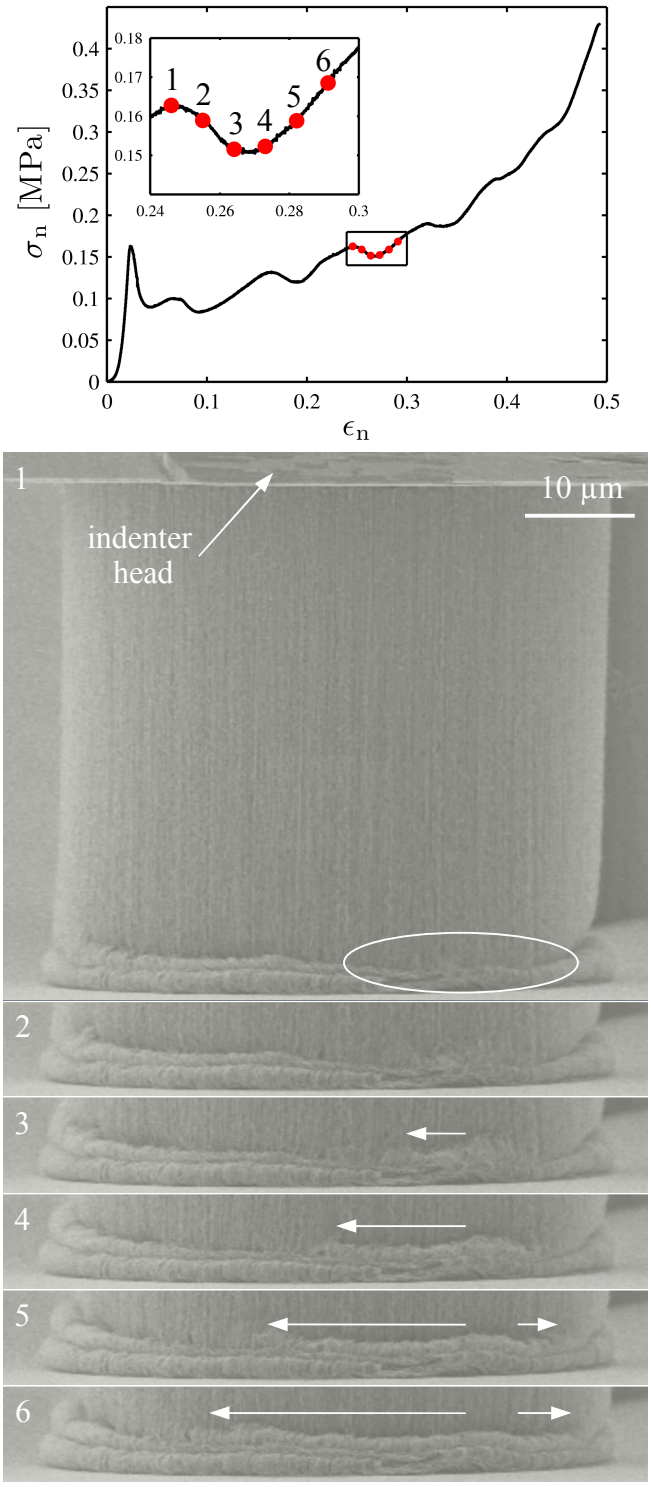

Figure 4.5: Frames from an *in situ* video illustrating the formation and propagation of a single buckle. Each of the frames aligns with the points on the accompanying stressstrain inset illustrating how a single hump corresponds to buckle initiation and propagation. The direction and magnitude of buckle propagation follow the overlaid arrows.

occurs at significantly higher loads (Figs. 4.1b), and its formation can be dramatically different even at the same loading conditions, sometimes initiating an abrupt shortening of the pillar. This causes the indenter head to momentarily lose contact with the pillar top (Fig. 4.6), resulting in a rapid load removal, and therefore a much lower stress immediately after

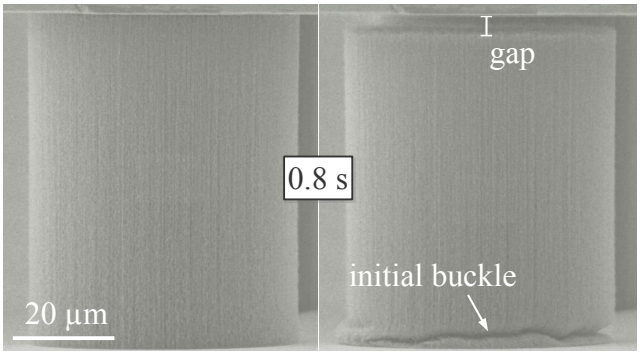

Figure 4.6: Frames from an *in situ* video illustrating the sudden initial buckle formation and momentary loss of contact with 0.8 s passing between the two images. Details of the initial buckle formation are difficult to see as they occur faster than the electron beam scan rate (0.3 μs per pixel on a 512×442 image, which is averaged over several scans to improve image quality). Note the gap formed between the collapsed pillar and the displacement-rate-constrained (300 nm s^{-1}) indenter head.

buckling. This loss of pillar-indenter contact is due to the pillar 'collapsing' faster than the prescribed rate of the indenter head motion. We observed this phenomenon in several experiments at each strain rate and during compression in both the nanoindenter and the SEMentor, suggesting a physically driven mechanism for this initial collapse rather than an experimental artifact. The inset in Fig. 4.1b shows a zoomed-in region in the stress-strain curves at each strain rate containing three examples where the pillar 'jumps' away from the indenter tip at strain rates of 0.001 s^{-1}, 0.1 s^{-1}, and 0.5 s^{-1}, and one example where it does not at the strain rate of 0.01 s^{-1}. The artificial loops in the stress-strain data are indicative of this loss of contact. Several samples, however, do not exhibit any discrete behavior and proceed at the prescribed nominal displacement rate, as shown in Figs. 4.3 and 4.5. Since these materials are highly inhomogeneous, sample variation among the pillars may be responsible for these differences.

We hypothesize that these discrete buckling events that result in a momentary loss of contact with the nanoindenter are caused by the coalescence or zipping up of the bottom-most layer of material. The driving force for coalescence is possibly due to the attractive

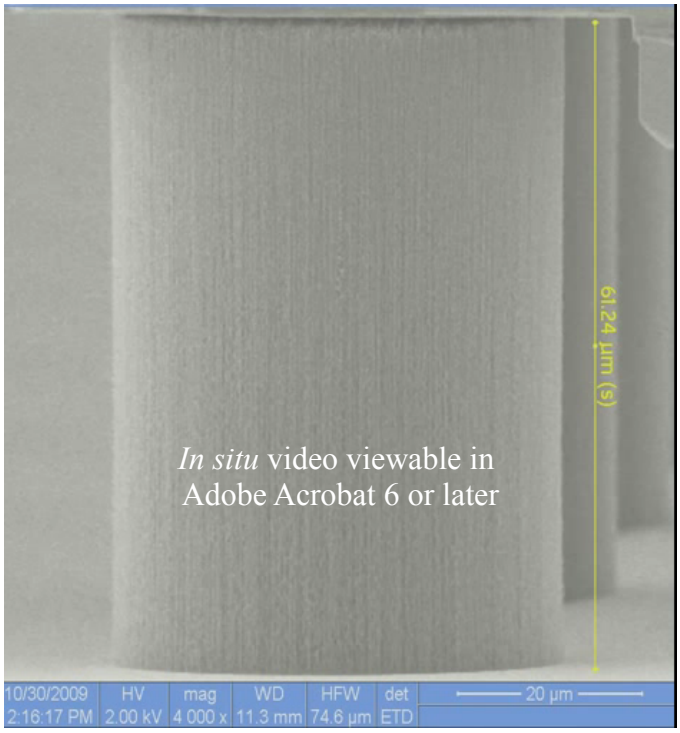

Figure 4.7: *In situ* video of several initial buckling events in which loss of contact between the indenter head and pillar top occured (electronic version only).

van der Waals forces between individual tubes, pulling them towards one another. This 'zipping' layer is initiated by crossing some threshold force at the weakest point within the layer, after which it becomes more energetically favorable for the adjacent CNTs to coalesce together and buckle, propagating the condensation/buckle reaction through the entire layer. In the cases where the zipping does not occur and the indenter head stays in contact with the bundle throughout the compression, it is possible that either the applied force never reaches that needed to 'zip up' a critical number of CNTs or that the critical concentration of tubes necessary for coalescence is not in place. Several factors could contribute to the marked difference in behavior between the initial buckle and all subsequent buckles; the catalyst-anchored CNTs can be pulled out and/or the microstructural network required for the 'zipping' behavior is only possible at the base (i.e., the network may be too ordered or too dense elsewhere). Gravity cannot be responsible for causing the undeformed region of the pillar to 'fall' upon the buckled first layer, as I have observed that even just a few tubes can easily bear the load of the entire pillar. Also, gravity acts in two different directions in the nanoindenter (parallel to the cylinder axis) and SEMentor (perpendicular to the cylin-

der axis). Additionally, CNTs within each fold do not appear to be broken (Fig. 4.8(b)), indicating energetic favorability for reconfiguration rather than structural failure during the 'zipping' process. The increased load required for the first buckling event is likely affected

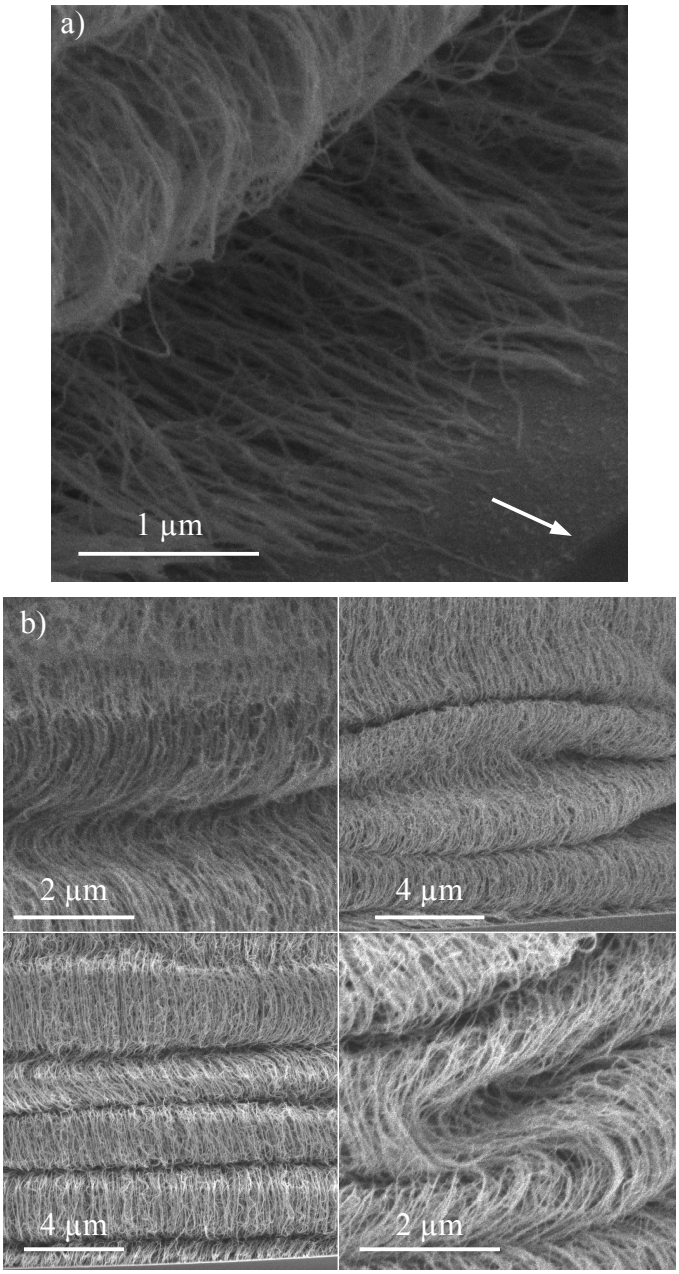

Figure 4.8: **a)** An SEM image of a post-mortem pillar base clearly showing several individual CNTs pulled away from the substrate surface. The initial anchor point of these tubes (the darker-to-lighter transition of the substrate) is indicated by the arrow. **b)** Several high-magnification SEM images reveal details of buckled regions. Within each buckle, CNTs appear to bend and twist without fracturing. The bottom left image shows a series of buckles of approximately the same size.

by a rigid boundary condition at the substrate, as first explored by Zbib, et al. [15] and subsequently in Chapter 5. It should be noted that here the boundary conditions are not constant throughout the initial buckling event as individual CNTs are observed to pull off of the substrate as illustrated in Fig. 4.8(a).

While the stress-strain curves at all strain rates share foam-like features, the humps that occur within the plateau region, corresponding to individual buckling events, are noticeably dependent on strain rate. There are distinct differences in the shape of these humps, with the slower strain rates producing smooth, sinusoidal undulations and the faster rates showing waves of significantly larger amplitude, as evident from the typical stress-strain curves for four different strain rates plotted in Fig. 4.1(b). For all strain rates, each undulation occurs at a progressively higher stress, rather than at a true plateau stress, typical of cellular solids, because each buckling sequence must nucleate and propagate through a stiffer, denser material than the previous one due to the axial tube density gradient discussed earlier. Although the curves chosen for Fig. 4.1(b) appear to reach higher stresses with higher strain rate, this trend does not hold true for all sets of data, and the maximum attained stress depends on the accuracy of the initial pillar-indenter alignment and microstructural variation between individual pillars.

4.3 Viscoelastic Response

Viscoelastic materials are commonly characterized by their storage and loss moduli, where the former represents the stored energy, or elastic response, and the latter corresponds to the amount of energy dissipated as heat. As mentioned in Section 2.5, I calculate the storage and loss stiffnesses, k_{storage} and k_{loss}, rather than moduli, E, because the latter requires knowledge of Poisson's ratio, ν, which is unknown for VACNTs though is likely close to zero, similar to that of a typical foam. Using Sneddon's relation (Eq. (2.5)), the conversion between stiffness and modulus is approximately E[kPa] $\approx 20 \times k$[N/m] (assuming $\nu \approx 0$). The storage and loss stiffnesses are measured and calculated through the procedure described in Section 2.5. Results are summarized in Figures 4.9 and 4.10 where closed and open symbols denote the measured values for storage and loss stiffnesses,

respectively. An alternate procedure for sample storage and loss determination reported by Wright et al. [31] models the sample as a standard linear solid (SLS). If applicable, this method enables calculation of the sample storage and loss stiffnesses for a continuous range of frequencies while accounting directly for the indenter head and frame stiffness. Following their approach, we used the frequencies of 8, 15, and 35 Hz to obtain the SLS model parameters (two spring constants and a damping constant). We find that while of the same order of magnitude, these SLS-based predictions do not follow the trends of the 'black box' analyses from Section 4.3, strongly suggesting that CNT foams do not behave as a standard linear solid and require the development of a more complex mechanical model.

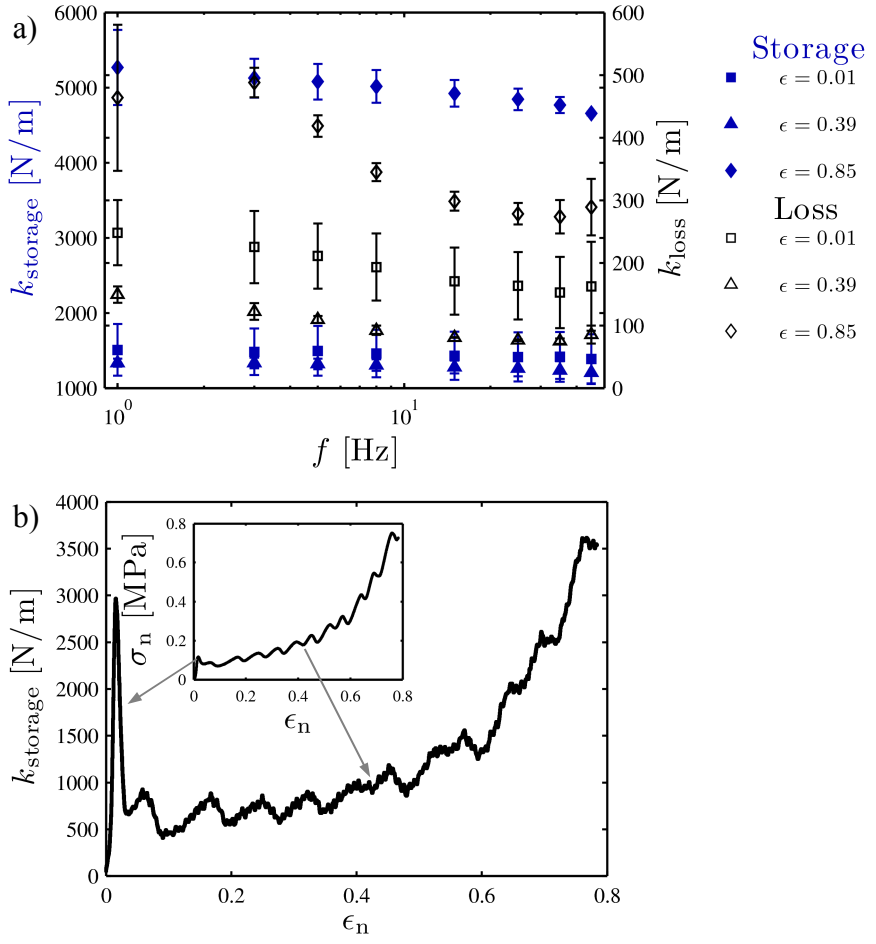

Figure 4.9: **a)** Storage and loss stiffnesses as a function of frequency for three ϵ_{n}. Closed symbols correspond to storage stiffness (elastic response), and open symbols represent loss stiffness (energy dissipation). **b)** Continuous stiffness measurement gathered during a quasi-static ($\dot{\epsilon}_{\text{n}}$, 0.001 s^{-1}) test. Gray arrows illustrate the one-to-one correspondence between the features in the stress-strain and stiffness-strain curves.

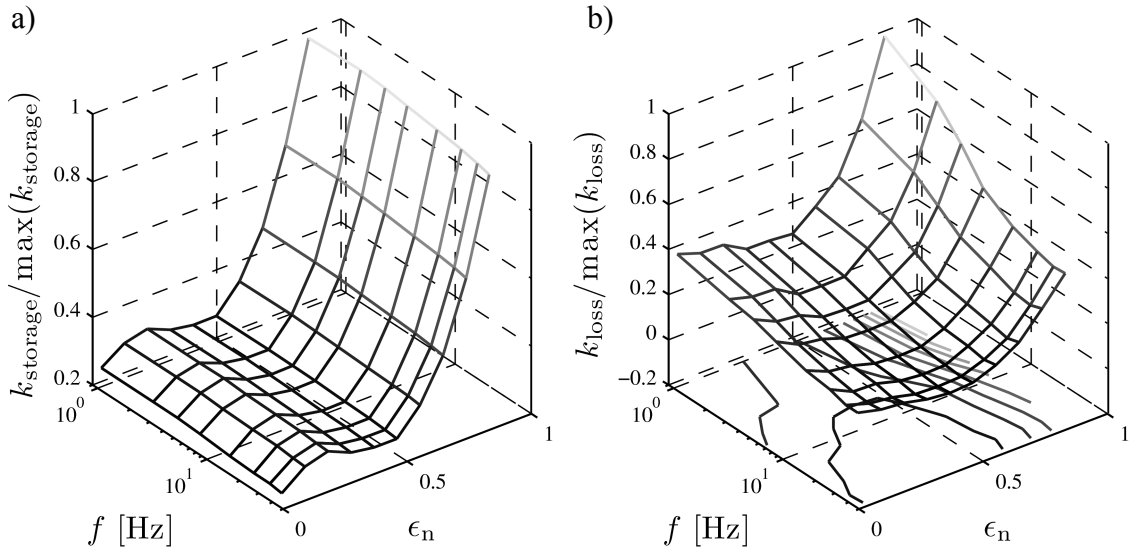

Figure 4.10: **a)** Storage stiffness as a function of frequency and strain showing high strain dependence, but little frequency dependence. **b)** Loss stiffness as a function of frequency and strain showing approximately equal dependence on strain and frequency.

We find that the storage stiffness is frequency independent over the range of frequencies tested, indicating a single energy storage mechanism operating over this range. It is also 10 times larger than the loss stiffness, indicating that more energy is being stored, rather than dissipated, in these materials. This relative ratio of storage to loss behavior is in approximate agreement with previous viscoelastic measurements [14, 19]. The storage stiffness increases with increasing strain (Fig. 4.10(b)) and is corroborated by quasi-static compression testing utilizing simultaneous continuous stiffness measurement (CSM) (Fig. 4.9(b)), which resolves drops in the elastic response corresponding to buckling events. These local fluctuations are averaged out in the storage stiffness data which is taken across several samples and not necessarily within a peak or trough of the stiffness curve. The transition between plateau and densification is clearly visible in both CSM and frequency varied storage stiffness data. The overall change in the stiffnesses is less pronounced in the loss stiffness (factor of 3) when compared with storage stiffness (factor of 5). Unlike the storage stiffness, the loss stiffness is a strong function of frequency, and is generally lower at higher frequencies, though it appears to be slightly bowl shaped. Unfortunately the cutoff frequency for our instrument prevents study of higher frequencies to study the extent of this apparent trend. This frequency dependence seems to be a reasonable observation since loss

mechanisms are typically deformation rate dependent. Thus, over the range of frequencies studied, the energy dissipation mechanisms appear to require a timescale longer than is afforded by a 35 Hz oscillation, with this trend being most evident at larger strains. Because attaining larger strains implies that a higher fraction of the pillar has buckled, we surmise that more energy is dissipated in the buckled portion of the pillar than in the remaining undeformed portion, and this dissipative process corresponds to a time constant of ~ 0.1 s. Simultaneously, the storage modulus indicates that even more energy is being stored in the buckled region. Both hypotheses are in line with observations in Xu et al. [19] in which they see 5 and 10-fold increases in the storage and loss moduli of VACNTs for a 4-fold increase in density.

4.4 Summary

We show that the deformation of CNT bundles in uniaxial compression is accommodated by sequential nucleation of local buckles followed by their lateral propagation across the bundle, gradually collapsing a horizontal slice of the entire structure in a periodic fashion. Buckles occur successively, from bottom to top. We hypothesize that this is due to a combination of the density and accompanying stiffness/strength gradient of the material and the constraint of the substrate. Stress-strain behavior is foam-like, but the stress does not remain constant in the plateau regime, and oscillations correspond to coordinated buckle nucleation and propagation rather than to individual cell collapse. In addition, we hypothesize that the significant slope within the 'plateau' region of the stress-strain response is dependent on the axial property gradient within the VACNT structure. Strain rate dependence is marked by the oscillations' magnitude: smaller for slower rates, sharper and larger for faster rates. Frequency dependence of the loss modulus indicates a timescale sensitive energy dissipation mechanism, largely contained within the buckled region of deformed pillars.

Chapter 5

Finite Element Analyses

5.1 Introduction

This chapter aims to provide insight into the largely irrecoverable deformation observed after uniaxial compression of the VACNT bundles observed in Chapter 4 (Ref. [44]) and by others [15, 47] as opposed to highly recoverable and/or viscoelastic behavior [13, 14, 19, 24, 47, 48], though many similarities exist between the two. In particular, we attempt to capture the localization of deformation via buckling observed under uniaxial compression [13, 15, 24, 44]. This work was carried out in collaboration with Prof. Alan Needleman of the University of North Texas.

We begin by briefly restating the key features observed in Chapter 4. As illustrated in Figure 5.1, this rich behavior is characterized by the accommodation of strain through the creation of a series of vertically localized folds or buckles, which form sequentially starting from the base (where CNTs grow from the substrate) and proceed toward the top [15, 24, 44, 46] (see Fig. 5.1(c)), and the initiation of buckles followed by their lateral propagation as revealed through *in situ* deformation of micron-sized cylindrical bundles, or pillars in Chapter 4 [44, 46] (see Fig. 5.1(b)). Figure 5.1a shows the overall foam-like stress-strain response gathered during testing. The response consists of elastic, plateau, and densification regimes typical of these materials [24]. The plateau possesses a small hardening slope. Here, we plot nominal stress, $\sigma_{\rm n} = P/A$, versus nominal strain, $\epsilon_{\rm n} = u_z/H$, where P is the applied load, A is the initial area of the top of the pillar, H is the initial pillar height, and u_z is the vertical displacement of the top. We find that immediately

following the elastic loading the load drops sharply before reaching the sloped plateau, which is characterized by periodic softening events shown to correspond to the appearance and evolution of individual buckling events [44]. This correspondence is illustrated in the image series in Fig. 5.1(b) for strains denoted by the blue circles in Fig. 5.1(a).

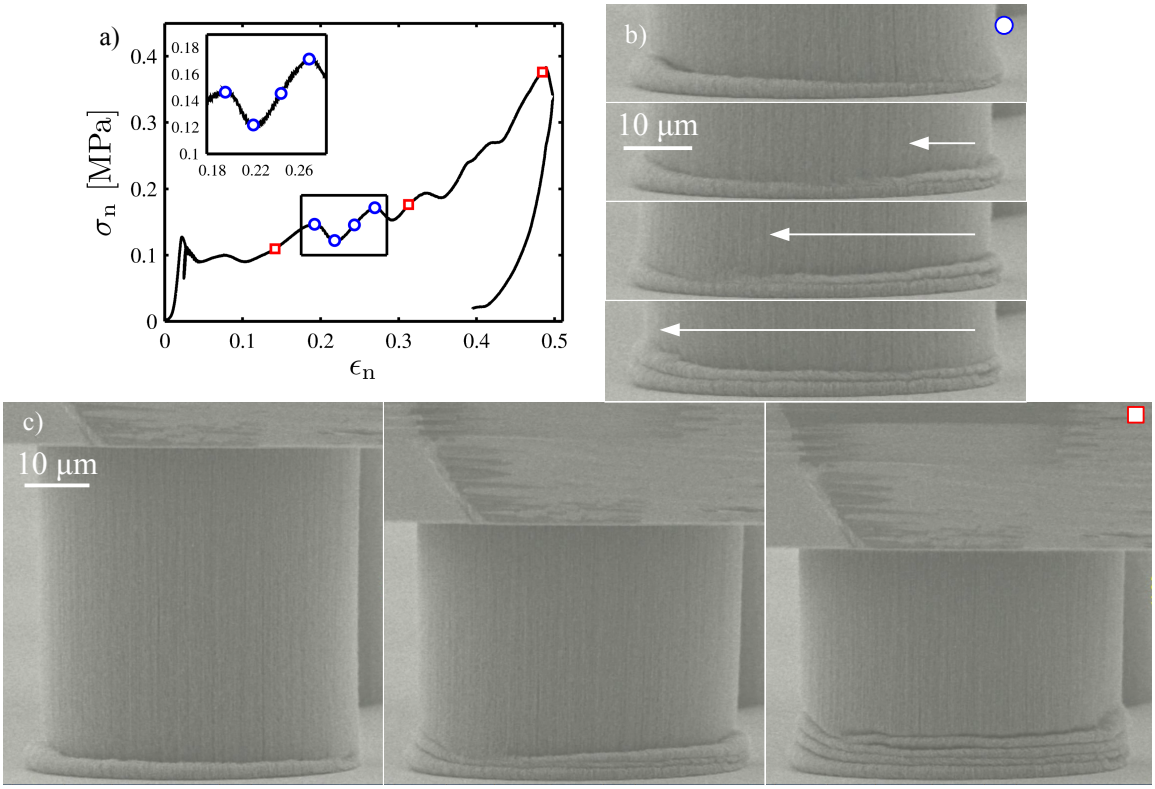

Figure 5.1: *In situ* mechanical compression results using methods presented in Hutchens et al. [44]. **a)** Nominal stress-strain response. Blue circles and red squares denote the strains at which the images in b) and c) were taken. **b)** Illustrates buckle initiation and evolution. **c)** Illustrates bottom-to-top sequential buckling.

While there are several experimental studies showing this highly localized commencement of structural collapse, models describing the mechanical response of VACNTs are few and past efforts have focused on capturing only the one dimensional stress-strain or load-displacement response. For example, the load-displacement response has been modeled energetically as well as in a standard linear solid framework and compared with nanoindentation testing results by Mesarovic et al. [42]. In addition, Euler buckling criteria were applied to uniaxial compression tests [15, 24, 45, 49] as well as nanoindentation testing [14, 42] in order to predict a threshold stress corresponding to the onset of buckling of the

CNT struts. The most detailed of these models by Zbib et al. [15] predicts a functional relationship between the sample height and this transition stress. These predictions are limited to capturing the behavior at relatively small overall strains. More recently, compressions of large VACNT mats were modeled as a one dimensional series of mesoscopic springs that are themselves limiting cases of infinite bi-stable springs in series [50]. This model captures the elastic recoverability and energy dissipation seen in many VACNTs. Bi-stable springs are characterized by a hardening-softening-hardening behavior that we also utilize here, as will be presented in Section 5.2. Our model attempts to capture the permanent, rather than the recoverable, deformation and includes the two dimensional deformational changes associated with the overall pillar stress-strain response through an axisymmetric finite element formulation, thereby enabling the analysis of buckle evolution and morphological characteristics.

We begin by discussing the physical foundation for our choice of constitutive law. We then outline the well-established finite element framework and specify the parameters used in the simulations. We compare results from our simulations with experimentally obtained uniaxial microcompression results from 50 μm diameter VACNT pillars and examine the influence of model parameters on buckle evolution and morphology. An examination of the parameter space of our model indicates the roles of various experimental factors affecting the mechanical response. Finally, we show the effect of prescribing a gradient in strength (along the pillar height) on both buckle evolution and the overall stress-strain response. In particular, we show that the presence of such a gradient, for example a lower yield stress at the bottom as compared with the top, is not needed for bottom-to-top sequential periodic buckling as initially thought.

5.2 Model Formulation

The complex, hierarchical nature of VACNTs makes the choice of scale in modeling their behavior non-trivial. At magnifications of 1000$\times$ they appear as arrays of vertically aligned tubes, markedly anisotropic. Magnifying one hundred times more reveals their highly interconnected, foam-like structure and the network of CNTs begins to appear nearly isotropic.

Magnifying another hundred times one obtains a view of the individual CNTs themselves. In this work, we propose a model that smooths over the discrete nature of the individual tubes and approximates the overall material behavior through an isotropic continuum constitutive relation in the same spirit as, for example, in the Deshpande-Fleck constitutive relation for foams [51]. Our model differs from others for VACNTs that focus on the scale at which the material appears to be a nominally aligned array of tubes [14, 15, 24]. The complex deformation and stress-strain behavior observed in Chapter 4 (Hutchens et al. [44]) serves as both motivation and validation for the choice of constitutive relation.

We use a finite deformation formulation and express the constitutive relation in terms of the rate of deformation tensor, $\mathbf{d}$, the symmetric part of $\dot{\mathbf{F}} \cdot \mathbf{F}^{-1}$, where $\mathbf{F}$ is the deformation gradient, and the Kirchhoff stress $\boldsymbol{\tau} = J\boldsymbol{\sigma}$, with $\boldsymbol{\sigma}$ being the Cauchy stress and $J = \det(\mathbf{F})$. A superposed dot denotes the partial derivative with respect to time. The rate of deformation tensor is taken to be the sum of elastic, $\mathbf{d}^{\mathrm{e}}$, and plastic, $\mathbf{d}^{\mathrm{p}}$, parts. Elastic strains are assumed to be small and are given by

$$\mathbf{d}^{\mathrm{e}} = \frac{1+\nu}{E}\hat{\boldsymbol{\tau}} - \frac{\nu}{E}\mathrm{tr}(\hat{\boldsymbol{\tau}})\mathbf{I}, \tag{5.1}$$

where E is Young's modulus, ν is Poisson's ratio, $\mathrm{tr}(\cdot)$ denotes the trace, $\mathbf{I}$ is the identity tensor and $\hat{\boldsymbol{\tau}}$ is the Jaumann rate of Kirchhoff stress.

In the experiments in Chapter 4 (Hutchens et al. [44], summarized in Fig. 5.1), little recovery of deformation was observed so that a material model framework allowing for permanent deformation was used. Also, material rate dependence is taken into account both for numerical reasons as well as in accordance with the observations by Zhang et al. [47]. We model the irrecoverable deformation response by a modification of the relation for an isotropic, hardening viscoplastic solid to account for the compressibility of the VACNTs. We write

$$\mathbf{d}^{\mathrm{p}} = \frac{3}{2}\frac{\dot{\epsilon}_{\mathrm{p}}}{\sigma_{\mathrm{e}}}\left[\mathbf{s} + B\,\mathrm{tr}(\boldsymbol{\tau})\mathbf{I}\right] \tag{5.2}$$

with

$$\dot{\epsilon}_{\mathrm{p}} = \dot{\epsilon}_0 \left(\frac{\sigma_{\mathrm{e}}}{g}\right)^{1/m}. \tag{5.3}$$

Here, $\dot{\epsilon}_0$ is a reference strain rate, m is the rate hardening exponent, $\mathbf{s}$ is the deviatoric

Kirchhoff stress tensor, $\mathbf{s} = \boldsymbol{\tau} - \mathrm{tr}(\boldsymbol{\tau})\mathbf{I}/3$, and σ_e is the equivalent stress, $\sigma_\mathrm{e} = \sqrt{3/2\,\mathbf{s} : \mathbf{s}}$. The compressibility parameter B is specified in terms of a plastic Poisson's ratio, ν_p, by

$$B = \frac{1}{3}\left[\frac{1-2\nu_\mathrm{p}}{1+\nu_\mathrm{p}}\right]. \tag{5.4}$$

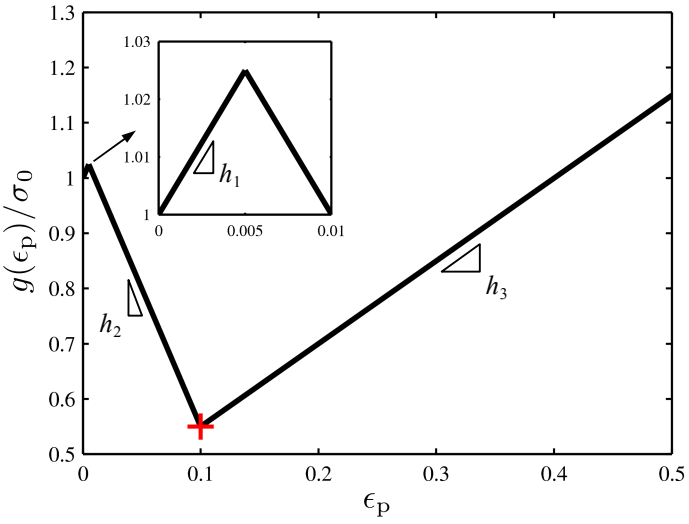

Figure 5.2: A plot of the hardening function, $g(\epsilon_p)$, for $\epsilon_1 = 0.005$, $\epsilon_2 = 0.1$, $h_1 = 5.0$, $h_2 = -5.0$, and $h_3 = 1.5$ illustrating its general shape as defined in Eq.(5.5).

Motivated by structural load-deflection responses that give rise to periodic folds (e.g., [52–54]), we characterize the flow strength or hardening function, $g(\epsilon_\mathrm{p})$, as consisting of a hardening range followed by softening and then subsequent rehardening. A simple form that embodies these features is

$$\frac{g\left(\epsilon_\mathrm{p}\right)}{\sigma_0} = \begin{cases} 1 + h_1\epsilon_\mathrm{p} & \epsilon_\mathrm{p} < \epsilon_1 \\ 1 + h_1\epsilon_1 + h_2\left(\epsilon_\mathrm{p} - \epsilon_1\right) & \epsilon_1 < \epsilon_\mathrm{p} < \epsilon_2 \\ 1 + h_1\epsilon_1 + h_2\left(\epsilon_2 - \epsilon_1\right) + h_3\left(\epsilon_\mathrm{p} - \epsilon_2\right) & \epsilon_\mathrm{p} > \epsilon_2 \end{cases}, \tag{5.5}$$

and is depicted in Fig. 5.2. Parameters h_1, h_2, and h_3 determine the hardening and softening slopes and ϵ_1 and ϵ_2 are the strains at which the hardening-softening and softening-hardening transitions occur, respectively, and σ_0 is a reference stress. The simplified, piecewise nature of the flow strength curve lends itself well to a systematic study of changes in behavior with variations in its shape as discussed in Section 5.3. It is worth noting that

the presence of a material rate dependence acts to regularize the governing equations in the softening regime [55]. A similarly shaped stress-strain relation, that of a bi-stable spring, was used by Fraternali et al. [50] as a microscale element of a 1-D model that captured the quantitative aspects of a reversible deformation response in uniaxially loaded bulk VACNT samples [24]. Attention is restricted to axisymmetric deformations, which eliminates the ability of the model to capture the nucleation and lateral buckle propagation seen in experiments (Fig. 5.1(b)), but still allows for local sequential buckling and significantly reduces the computational time.

The finite element formulation is based on the dynamic principle of virtual work, which can be written as

$$\int_V \boldsymbol{\tau} : \delta\mathbf{d}\, dV = \int_S \mathbf{T}\cdot\delta\dot{\mathbf{u}}\, dS - \int_V \rho\ddot{\mathbf{u}}\delta\mathbf{u}\, dV, \tag{5.6}$$

where V and S are, respectively, the volume and surface of the body in the initial configuration, $\mathbf{T}$ is the traction vector, and $\mathbf{u}$ is the displacement vector.

We perform calculations for a cylinder of height H and radius R. With the assumption of axisymmetric conditions in a cylindrical coordinate system (r,θ,z) all field quantities are independent of θ. A velocity $\dot{u}_z(t)$ is imposed at the top of the pillar, $z=H$, with

$$\dot{u}_z(r,H,t) = \begin{cases} -v_z\frac{t}{t_{\text{rise}}} & \text{for } t < t_{\text{rise}} \\ -v_z & \text{for } t > t_{\text{rise}} \end{cases}, \tag{5.7}$$

and $T_r(r,H)=0$. Here, t_{rise} is the time interval over which the velocity is ramped up to avoid shock loading the system. The bottom of the pillar is presumed fixed to the substrate so $\dot{u}_r(r,0,t)=\dot{u}_z(r,0,t)=0$. The outer surface of the pillar is taken to be traction free, $T_r(R,z)=0$. We do not account for possible contact between the folds that develop due to buckling. The calculations are terminated prior to any material contact.

The finite element discretization of Eq. (5.6) is based on a convected coordinate representation of the governing equations with linear displacement crossed triangles as in a number of previous analyses, e.g., Tvergaard et al. [56] and Tvergaard and Needleman [57]. Time integration is carried out by the explicit Newmark β-method [58] using lumped masses. The rate tangent method of [59] is used for the constitutive update.

5.2.1 Simulation Parameters

The calculations are carried out with $E/\sigma_0 = 100$, $m = 0.02$ (on the order of experimentally measured values of rate sensitivity in VACNTs [47]), $\dot{\epsilon}_0 = \dot{\epsilon}_{\text{ref}}$, $\nu = 0.25$, $\nu_p = 0.25$. The mesh geometry is that of a circular cylindrical pillar with an aspect ratio, H/R, of 3. The imposed velocity, v_z, in Eq. (5.7) is fixed at $\kappa\dot{\epsilon}_{\text{ref}}H$ with $\kappa = 0.004$ and the ramp time $t_{\text{rise}} = 5/\dot{\epsilon}_{\text{ref}}$. The initial hardening portion of Eq. (5.5) was fixed at $\epsilon_1 = 0.005$, $h_1 = 5$ throughout this study. Results are presented for variations in ϵ_2, h_2, h_3.

The finite element mesh in all calculations consists of a uniform 80×240 mesh of quadrilateral "crossed triangle" elements each of which is $H/240 \times H/240$.

If the analyses were quasi-static, these dimensionless parameters would be sufficient to characterize the formulation. However, dynamic, rather than quasi-static, analyses are carried out because, even though the response is generally quasi-static, dynamic snapping can occur due to the up-down-up shape of $g(\epsilon_p)$ (see Fig. 5.2). Hence, a density needs to be specified and is taken to be $\rho = 10^{-14}\,\sigma_0(\dot{\epsilon}_{\text{ref}}/H)^2$ in non-dimensional form.

For $\sigma_0 = 0.1$ MPa, $H = 75$ μm and $\dot{\epsilon}_{\text{ref}} = 25$ s^{-1}, we have $E = 10$ MPa and $\rho = 1.11 \times 10^{-4}$ MPa/(m s)^2 ($\rho = 111$ kg/m^3). Also, $v_z = 7.5$ μm/s and $t_{\text{rise}} = 0.2$, which corresponds to the applied displacement achieving its constant value when the overall strain, $u_z(r, H, t)/H$, reaches 0.01. All of these values are of a similar order to those in the experiments.

Axial gradients in E and σ_0 are incorporated into the material through multiplication of these variables by a dimensionless function $Q(z)$, where $Q(z) \equiv 1$ corresponds to the case in which there is no gradient with z evaluated at the center of the element for which the rescaled E and σ_0 values are being calculated.

5.3 Results and Discussion

Implementation of the model, outlined in Section 5.2, and subsequent exploration of the parameter space resulted in capturing many of the qualitative features of CNT pillar deformation seen in experiments (Fig. 5.1). Interpretation of the parameters that lead to sequential periodic buckling in axisymmetric pillars enables the generation of hypotheses

regarding buckle characteristics (e.g., wavelength and amplitude) given a relationship between the CNT microstructure and the hardening function. The qualitative results from an example set of parameters are summarized by Fig. 5.3 in which an experimental nominal stress, $\sigma_{\mathrm{n}} = P/A_0$, versus true strain, $\epsilon_{\mathrm{t}} = \ln(1+\epsilon_{\mathrm{n}})$, response from a uniaxial compression experiment [44] is shown in Fig. 5.3a for reference. We plot the analogous response from a simulation (Fig. 5.3(b)) in terms of the nominal stress, $\sigma_{\mathrm{n}} = P/[\pi R^2]$, and true strain, $\epsilon_{\mathrm{t}} = -\ln[(H + u_z(r, H, t))/H]$, where P is the sum of the nodal forces in the z direction at the top of the pillar. In both the experiment and the simulation, the area of the

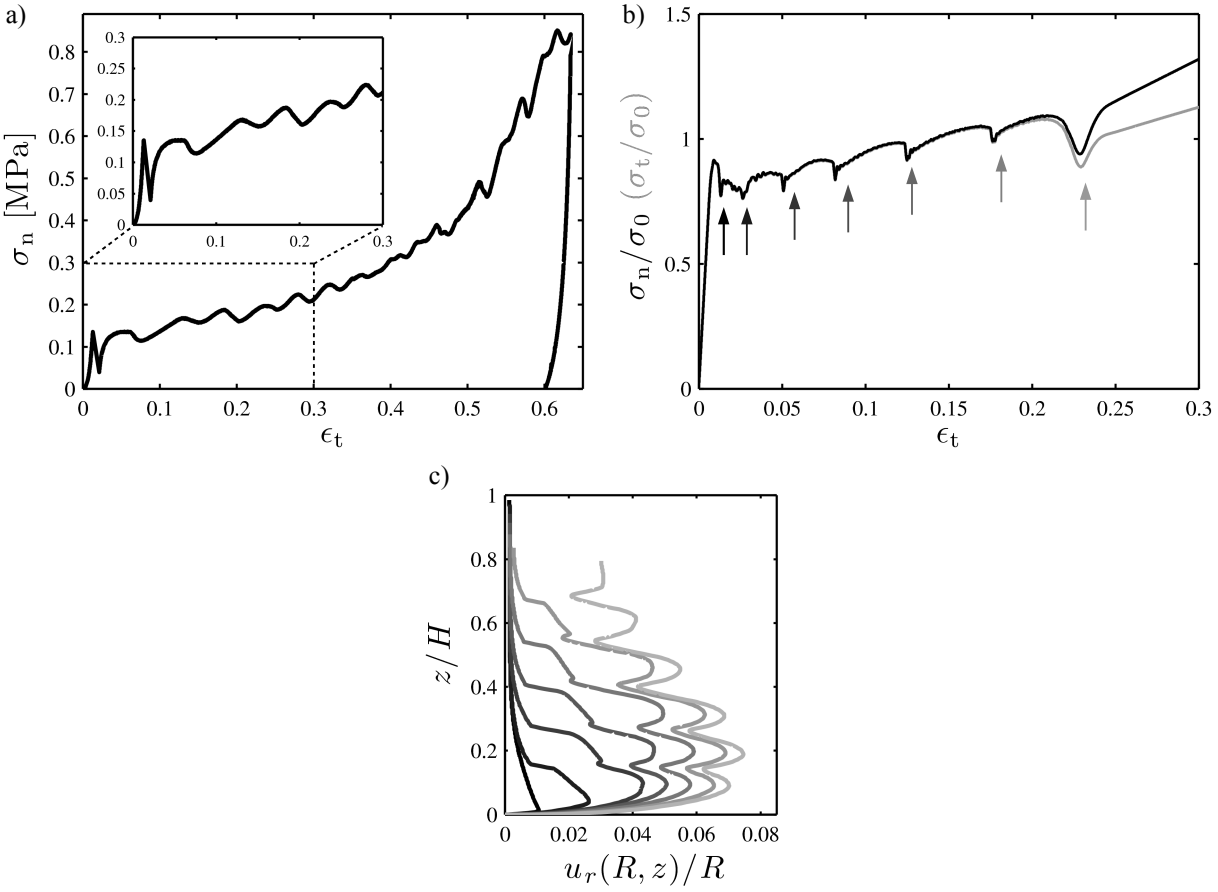

Figure 5.3: Summary of buckle formation phenomena captured by simulations utilizing the proposed constitutive relation. **a)** Experimental data from a pillar microcompression [44]. Inset shows a closeup of the strain region from 0 to 0.3. **b)** The overall nominal stress, force/original area, and true stress, force/current area, versus true strain response from a simulated pillar undergoing periodic sequential buckling. Arrows mark the strains at which the outer displacement profiles are plotted in c). **c)** Outer displacement profiles corresponding to strains directly following a softening event and illustrating simultaneous buckle emergence.

top of the pillar is nearly constant during the process of sequential buckling so that the difference between nominal and true stress is negligible over the majority of the range during which buckling occurs.

In both stress-strain responses in Fig. 5.3 there is a noticeable transition from the linear elastic region to the (sloped) plateau region. An inset of the experimental data is given in Fig. 5.3(a) in order to facilitate comparison with Fig. 5.3(b). The model gives similar behavior as illustrated by a comparison of the ratio of the stress at a strain of 0.2 to the stress at the beginning of the buckling regime ($\epsilon_{\rm t} = 0.05$) in Fig. 5.3(a) to the same ratio for strains of 0.2 and 0.015 in Fig. 5.3(b). These ratios are around 1.3 in both cases. Periodic, local softening events occur within the plateaus and each corresponds to the formation of a new buckle. For the simulations, this finding is illustrated by a collection of curves showing the evolution of the outer surface, $u_r(R, z)/R$ versus z/H, (Fig. 5.3(c)) at several discrete values of the overall pillar strain, ϵ_t, that immediately follow a softening event. These strain values are indicated by arrows in Fig. 5.3(b) where both nominal and true (force/current area) stress values are shown. The outer displacement profiles clearly identify sequential buckle formation beginning at the bottom and progressing to the top. As in experiments, nearly all of the deformation is accommodated through the formation and evolution of localized buckles with the topmost region of the pillar remaining undeformed throughout, as evidenced in the strain contour plots in Fig. 5.3(c). All the simulation results in Fig. 5.3 correspond to the parameters defined in the caption to Fig. 5.2 and include a linear gradient, $Q(z)$, that gives values of σ_0 and E at $z = H$ that are of 40% of their values at $z = 0$. Subsequently, we discuss the effect of an applied gradient on the overall pillar hardening.

The responses shown in Fig. 5.3 are approximately quasi-static since the total kinetic energy of the system remains around 2% of the input work throughout the short rise time discussed in Eq. (5.7), during which the structural response is largely elastic, and then drops to less than 1% for the remainder of the calculation.

A parameter study on the effect of strain rate is not carried out here. However, we have carried out calculations in which the strain rate is increased from the imposed value in Fig. 5.3 by a factor of 2 and decreased from that value by a factor of 1/2 (with all other

parameters fixed). As expected with a strain rate exponent of $m = 0.02$, the effect of changes in strain rate on the stress magnitude is small. The main effect is that the average stress drop that occurs with each buckling event is somewhat greater when the strain rate is doubled and somewhat less for the case when the strain rate is halved. This trend is in agreement with experiments carried out over 3.5 orders of magnitude in strain rate [44] where it was observed that the magnitude of the stress undulations during buckling was greater at larger strain rates.

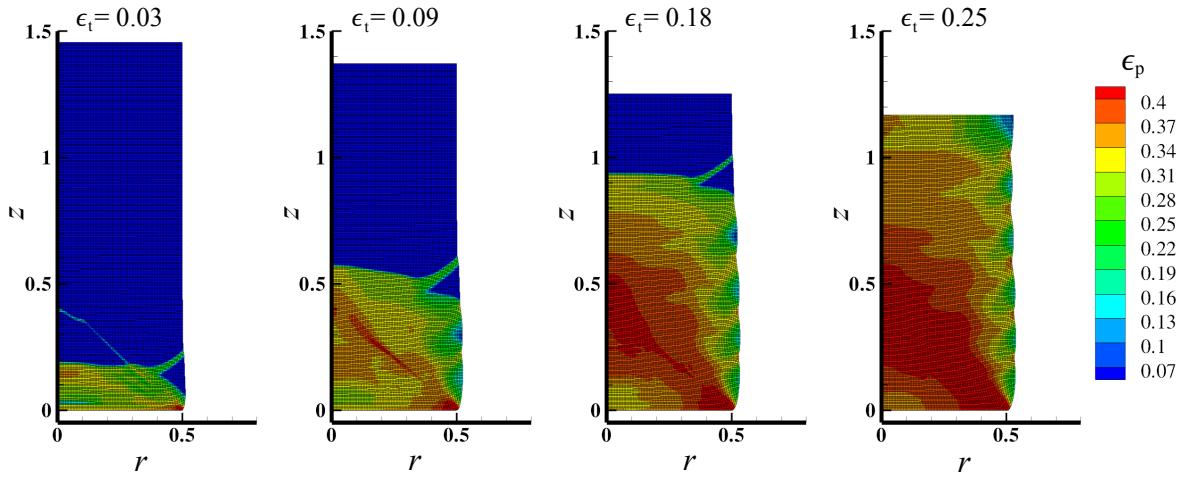

Figure 5.4: Series of strain contour plots and deformed meshes clearly showing sequential deformation and the relatively undeformed upper region of the pillar.

In exploring the model's parameter space, we found that the range in which buckle formation occurs, and where energy absorption is most effective, is limited. Within that buckling domain, we explore the separate contributions of the flow strength function's 'well' width, formed by the intersection of the softening and rehardening slopes, and magnitude of the softening slope, h_2, to changes in buckle morphology. Some calculations are carried out for a homogeneous pillar. However, based on images taken along the VACNT pillar height, there is reason to believe that there is an axial density gradient. Therefore, we investigate the effect of gradients in the onset of plastic flow, σ_0, and elastic modulus, E, for a single set of parameters. In order to illustrate the range of and reason for the limited buckling domain, a typical series of responses corresponding to selected flow strength functions, $g(\epsilon_p)$, are shown in Fig. 5.5. All have fixed hardening slopes, $h_1 = 5$ and $h_3 = 1.5$, with $\epsilon_1 = 0.005$, but vary in the location of their minima, marked by the symbols in Fig. 5.5(a).

For example, a hardening function corresponding to a minimum at $\epsilon_2 = 0.1$ and 55% of

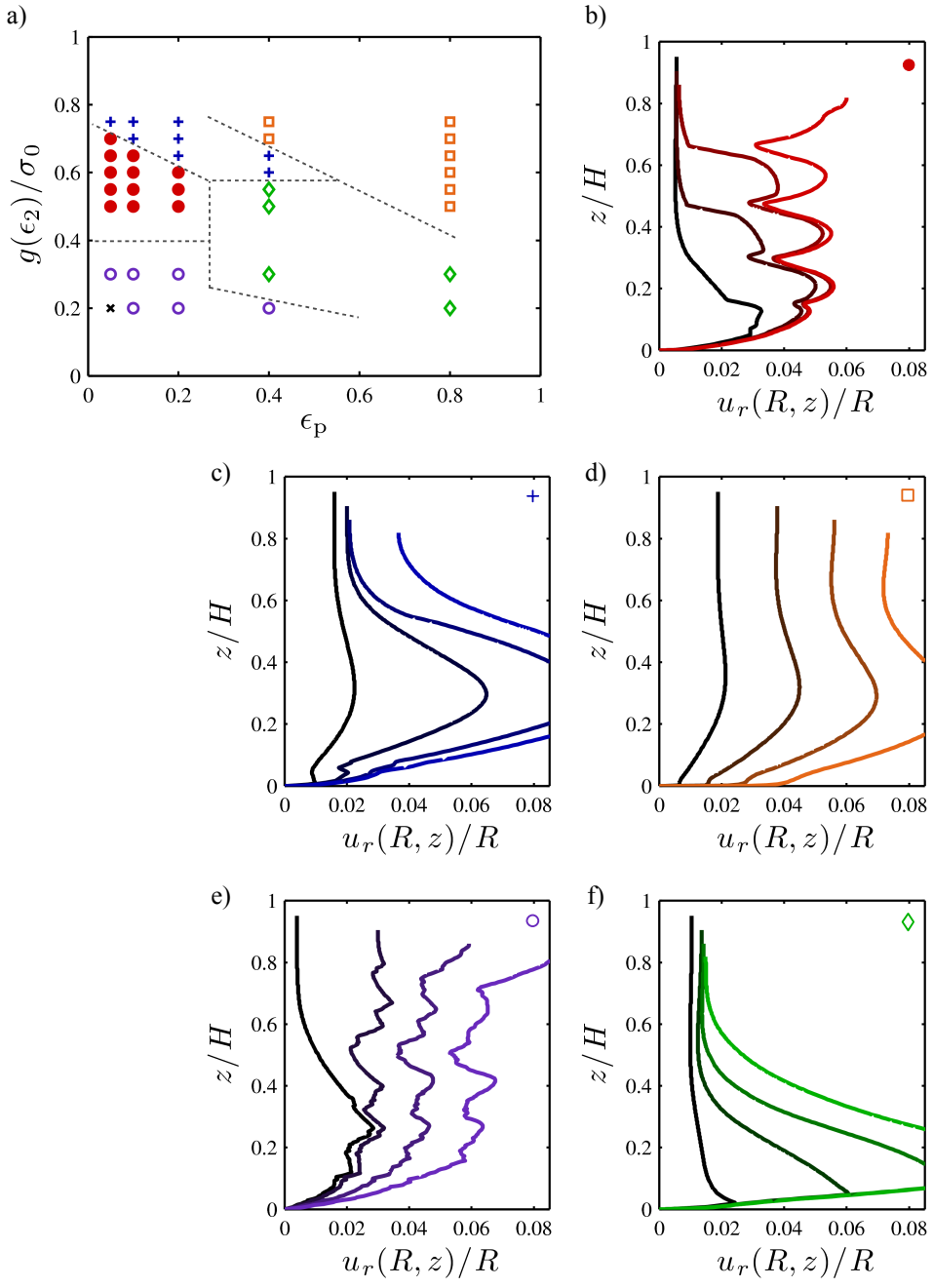

Figure 5.5: Influence of the 'well' minimum position on the formation and morphology of buckles. ($h_1 = 5$, $h_3 = 1.5$,$\epsilon_1 = 0.005$) **a)** Minima locations tested. Domains are denoted by (closed circles) buckling, (pluses) base-only buckling, (open circles) instability dominated, (diamond) base flow, and (squares) bulk flow. (**b**)–(**f**) Representative displacement profiles at $r = R$ for overall strain levels of $\epsilon_t = 0.05$, 0.10, 0.15, and 0.20 for each of the domains.

h/σ_0 ($h_2 = 5.0$) exemplifies the buckling domain (filled circles) through the series of outer displacement profiles given for overall pillar strains of $\epsilon_{\mathrm{t}} = 0.05$, 0.10, 0.15, and 0.20 (Fig. 5.5(a)). Outside of this buckling regime there are several types of behavior that can be roughly categorized into four groups. First, the instability domain (open circles), occurs where minima are located at similar strains but at a greater depth than that for the buckling domain, i.e., they possess a large softening slope h_2. Here, periodicity is completely lost and the deformation is dominated by local instability arising from the large magnitude of h_2. Diagonally upward, at greater strain from the buckling domain, lies the base-only buckle domain (pluses). Here, the local instability due to softening is somewhat preserved, as evidenced by the small waves localized at the pillar base, however, the depth of the minimum has decreased so much that the behavior begins to approach that of a typical foam, i.e., a hardening function in which the softening region is replaced by a flat line, $h_2 = 0$. Continuing toward minima at larger strain but similar depth, there is a bulk flow domain (open squares) where the the magnitude of ($|h_2|$) has considerably decreased to the point that the presence of a local minimum has no noticeable contribution. Here, local flow is large and, as a result, the pillar undergoes extensive flow in a manner that is nearly identical to that seen for typical foam-like simulations ($h_2 = 0$). Finally, holding the magnitude of h_2 approximately constant while extending minima to greater strains we enter what we call the base flow domain (open diamonds). In this domain, a large strain occurs only at the base of the pillar. Periodic buckles do not form as the extensive deformation, due to the large strain position of the minima, damps out any surface fluctuations that would form. It is noteworthy that all of the simulations shown in Fig. 5.5 were generated with no gradient, $Q(z) \equiv 1$.

As a result of these observations of the different morphological domains and their dependence on the character of the flow strength, $g(\epsilon_{\mathrm{p}})$, it becomes clear that a balance between the magnitude of h_2 and the size of the 'well' in $g(\epsilon_p)$ must exist in order to obtain the experimentally observed buckle morphology. In particular, it is evident that the local flow due to the 'well' size (i.e., width) must be limited enough that it does not wash out the undulations that form. Another way to state this is that the material must be strain constrained. We interpret this within the known morphology of VACNTs by noting that the

intertube interactions (entanglement, van der Waals, etc.) limit the local strain that can be experienced by the material. The local softening captured by h_2 arises from the high aspect ratio of the CNT struts which individually undergo a large drop in stiffness by buckling in uniaxial compression. We propose then that local strain constraint, combined with the high aspect ratio of the CNT struts, gives rise to the complex buckling behavior seen in so many VACNT compression experiments. It should be noted that only a variation in the extent of these domains is seen for changes in the value of the hardening coefficient h_3 in Eq. (5.5) as variations in h_3 give rise to similar domains that have the same relative positions with respect to each other.

Within the buckling domain, variations in buckle wavelength and amplitude can be decoupled from one another through control of specific characteristics of the hardening function. These findings are summarized in Fig. 5.6. We define $\Delta\epsilon_{\mathrm{w}}$ as the plastic strain range from the value of ϵ_{p} at which the function $g(\epsilon_{\mathrm{p}})$ in Eq. (5.5) first attains a maximum to the value of ϵ_{p} at which $g(\epsilon_{\mathrm{p}})$ attains that value again as as illustrated in Fig. 5.6(a). $\Delta\epsilon_{\mathrm{w}}$ characterizes the width of the 'well' in the flow strength function, $g(\epsilon_{\mathrm{p}})$. We find that with the depth of the minimum in $g(\epsilon_{\mathrm{p}})$ and the value of h_2 held constant while varying $\Delta\epsilon_{\mathrm{w}}$, the wavelength of the buckles remains the same and the amplitude increases (Fig. 5.6(b)). We quantify the changes in amplitude through a sine wave fit of the buckling region and define the relative change in amplitude, Δa, as

$$\Delta a = \frac{a_\Delta - a_0}{\frac{a_\Delta + a_0}{2}}. \tag{5.8}$$

where a_0 and a_Δ are the amplitudes determined from fits of the results from the reference parameters and from $\pm 25\%$ changes in $\Delta\epsilon_{\mathrm{w}}$, respectively. An analogous expression was used to quantify the relative changes in wavelength, $\Delta\lambda$. A relative change in amplitude of -16% was obtained for a 25% decrease in $\Delta\epsilon_{\mathrm{w}}$ and a relative change of 12% was obtained for a 25% increase. The respective variations in wavelength of the buckles, $\Delta\lambda$, were -2% and 3%. Analogously, holding the depth of the minimum of $g(\epsilon_{\mathrm{p}})$ and $\Delta\epsilon_{\mathrm{w}}$ constant while varying h_2, the amplitude of the buckles is much less affected while the wavelength decreases (Fig. 5.6(d)). A sine wave fit revealed relative changes in $\Delta\lambda$ of 7% and -4% for a 25% decrease and a 25% increase in h_2 with Δs varying by -2% and 0.5% respectively.

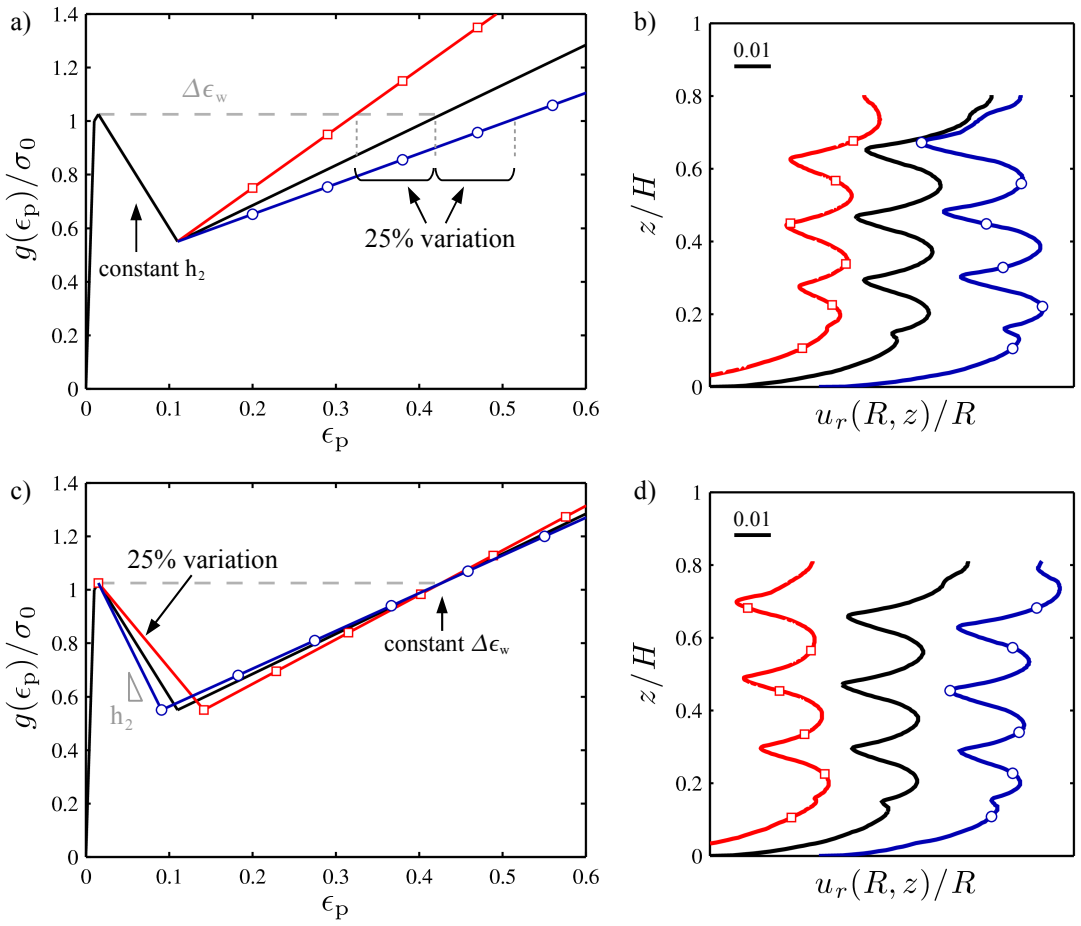

Figure 5.6: Variation in buckle wavelength and amplitude as a function of changes in $\Delta\epsilon_w$ and in the magnitude of h_2. **a)** Schematic indicating the variations in the hardening function, $g(\epsilon_p)$, considered for 25% changes in $\Delta\epsilon_w$. (red/squares = decreased, blue/circles = increased) **b)** A series of displacement profiles at $r = R$ corresponding to the hardening functions in a). An increased value of $\Delta\epsilon_w$ leads to increased buckle amplitude. **c)** Schematic indicating the variations in the hardening function for 25% changes in the magnitude of h_2. (red/squares = decreased, blue/circles = increased) **d)** A series of displacement profiles at $r = R$ corresponding to the hardening functions in c). An increased magnitude of h_2 leads to decreased buckle wavelength.

If h_2 is fixed and $\Delta\epsilon_w$ varied (or vice versa), while the depth of the minimum in $g(\epsilon_p)$ is allowed to change, the wavelength and amplitude variations are much more strongly coupled, and the buckle morphology varies in a way that precludes extracting a simple trend.

These correlations between the changes in h_2 and $\Delta\epsilon_w$ and the resulting variations in buckle wavelength and amplitude can be qualitatively related to real VACNT materials

as follows. If we presume that the ability of a VACNT material to flow is constrained by the tube-to-tube interactions, we expect that a more dense (number of tubes per unit volume) material would produce smaller amplitude buckles due to its increased number of interactions and therefore decreased deformability. If the magnitude of the negative slope, h_2, is correlated with CNT strength in compression (i.e., smaller diameter tubes soften with a greater slope than larger diameter tubes), we expect that a material made with smaller tubes would have shorter wavelength buckles.

It has been speculated that the initiation of the sequential buckling phenomena observed experimentally by several research groups was due to an axial density gradient in the material [24, 44]. This is motivated by the observations of a lower CNT number density base of similarly grown VACNTs as discussed in Chapter 3 and Ref. [35]. An axial gradient in the number of load bearing members is expected to give rise to a corresponding inhomogeneity in stiffness and yield stress. Since the precise correlation between the stiffness and the tube number density remains to be determined, we refer to it hereafter as a property gradient. We explore the effects of such a property gradient within the simulation framework by multiplication of E and σ_0 by the function $Q(z)$, where $Q(z) = 1$ corresponds to the case in which there is no gradient. We find that changes in Young's modulus, E, have very little effect on the shape of the stress-strain curve or the overall buckle morphology, but are included for completeness. We present the results of simulations with no gradient (black), 20% and 200% linear increases (blue/circles, red/squares), and a 10% linear decrease (green/triangles) in $Q(z)$ in Fig. 5.7. Here, in Fig. 5.7(b) we plot curves of true stress, $\sigma_{\mathrm{t}} = P/[\pi(R + u_r(R, H, t))^2]$ versus true strain, $\epsilon_{\mathrm{t}} = -\ln[(H + u_z(r, H, t))/H]$. Simulations with no property gradient give rise to sequential periodic buckling (Fig. 5.7(b)), implying that buckle formation is robust against local density variations. The fixed constraint of the rigid substrate, as is the case for as-grown CNT bundles, we model by the fixed displacement boundary conditions at $z = 0$. This constraint induces non-uniform deformation, which promotes buckle initiation at the base of the pillar. The gradient in σ_0 has a marked effect on the hardening slope of the plateau region in the overall pillar stress-strain response as illustrated by the curves corresponding to 20 and 200% increases (Fig. 5.7(a)). Here, it is clear that the property gradient directly correlates with the overall pillar

hardening as a $10\times$ increase in property gradient yields an approximately $5\times$ increase in overall strain hardening. For property gradients that are sufficiently large, $\sim 400\%$, periodic buckling is no longer obtained. In our calculations, even a small reverse gradient can cause the sequential buckling to occur in the reverse direction (Fig. 5.7(c)), suggesting that a plausible explanation for variation in top-first vs. bottom-first buckling [43, 60] is the difference in the spatial location of the least number of load-bearing members within the sample.

Although our model captures some of the key qualitative features of VACNT pillar buckling, there are also some discrepancies between the model predictions and the experimental observations. One marked difference concerns the number and size of buckles. This could be due to a number of idealizations including, for example: isotropy and the simple characterization of compressibility, such as the assumption of a constant value of the compressibility parameter, B, in Eq. (5.4). In addition, contact between buckles is not modeled.

5.4 Summary

We report that a dynamic finite element implementation of an isotropic, viscoplastic solid combined with a piecewise positive-negative-positive hardening function within an axisymmetric pillar mesh geometry captures the main qualitative features seen in experimental microcompression tests on 50 μm VACNT pillars. These include sequential, periodic buckling initiated at the base of the pillar and progressing to its top, strain accommodation nearly entirely through the formation of localized buckles, a stress-strain response characterized by an elastic loading followed by a low-hardening plateau, local softening events within the plateau corresponding to buckle formation, and strain hardening within the buckle region due to an axial property gradient. We explore the parameter space that we use to define a window in which buckle formation occurs, thereby providing understanding of the microstructural mechanism behind buckle formation. Through this exploration, we find that the buckle wavelength decreases with an increased magnitude of the negative hardening slope and its amplitude increases with an increased width of the 'well' in the flow strength function. Agreement with multiple experimental observations provides evidence that the proposed constitutive relation is a reasonable starting point for developing a full three dimensional, anisotropic constitutive relation for VACNTs. In addition, exploration of the parameter space within the simple, isotropic model provides insight into the mechanisms governing VACNT deformation. Specifically, it is the strain-constrained nature of VACNTs combined with the loss of load carry capacity accompanying the buckling of the CNT struts that gives rise to the sequential periodic buckling that characterizes these materials in uniaxial compression. The model also reveals bottom-to-top buckling, even in the case of homogeneity (no axial property gradient). However, we find that this buckling sequence can be reversed (top-to-bottom) with a small inverse property gradient (having lower strength at the top). Finally, we show that the value of the slope of this property gradient directly correlates with a post-buckling increase in the overall pillar stress level.

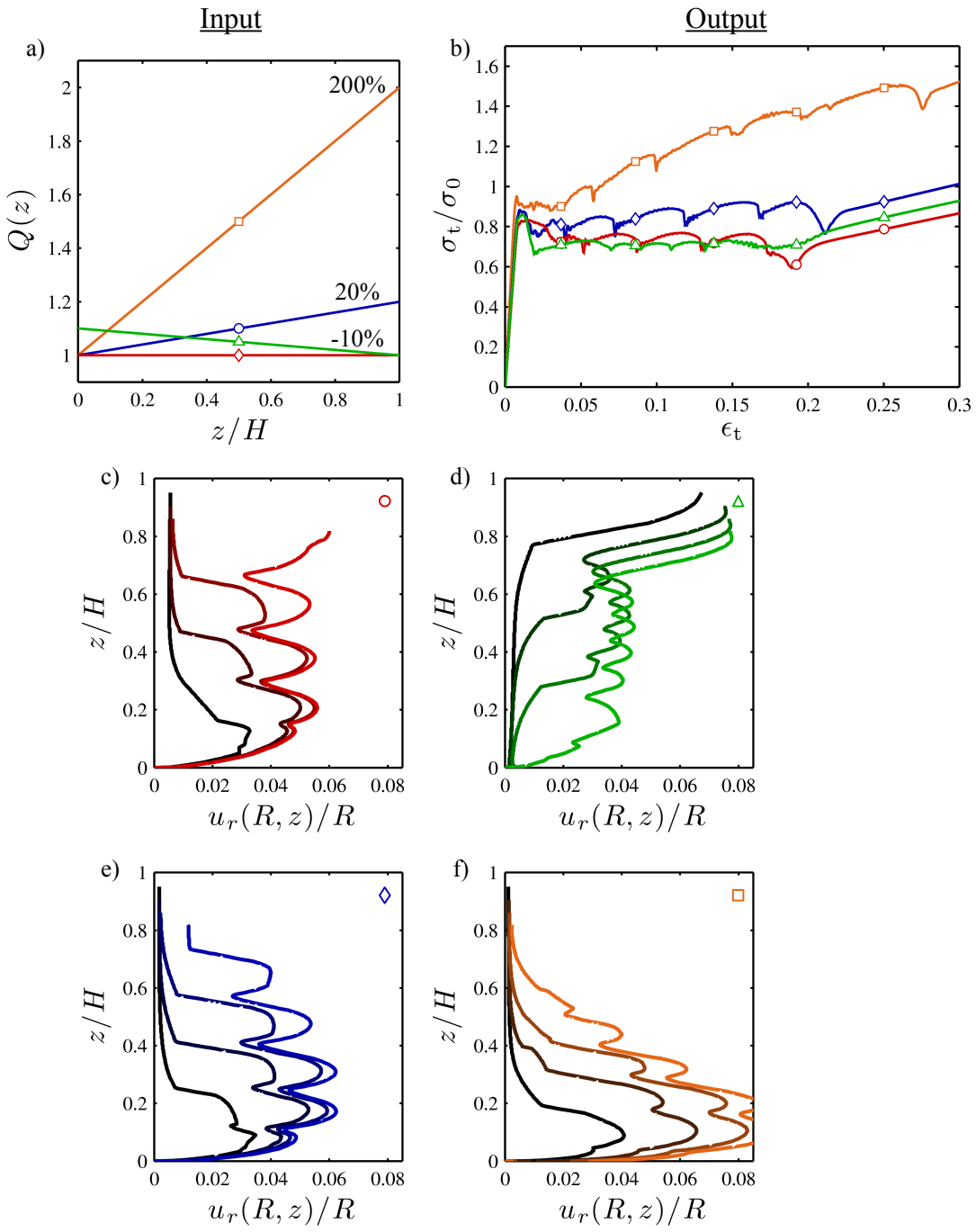

Figure 5.7: The effects of a gradient in σ_0 and E on the pillar's true stress-true strain response. **a)** Input axial gradients, $Q(z)$, applied to σ_0 and E to give the responses in b). **b)** Stress-strain responses from simulations having no (red/diamond), 20% and 200% linear increasing (blue/circle, orange/square), and 10% linear decreasing (green/triangle). **c)** Displacement profiles at $r = R$ at four strain levels ($\epsilon_t = 0.05$, 0.10, 0.15, and 0.20) for the calculation with no gradient in σ_0 and E. **d)** As in c) but for a 10% linearly decreasing gradient. **e)** As in c) but for a 20% linearly increasing gradient. **f)** As in c) but for a 200% linearly increasing gradient.

Chapter 6

Summary and outlook

This work has been an early study on VACNTs. I have performed unique mechanical experiments that have corroborated the bottom-first buckling sequence of VACNTs under uniaxial loading. Additionally, I observe that these buckles form by initiating at a local instability before propagating laterally across the pillar rather than collapsing as a single layer all at once. I propose a constitutive relation implemented in a finite deformation, finite element model that captures the sequential periodic nature of the buckles for an axisymmetric cylindrical structure having similar boundary conditions and under uniaxial compression. Interpretation of the behavior of this model and its dependence on parameters governing the local flow of a material element indicates that the formation of sequential periodic buckles is due to local flow constraint of the material, which demands the formation of surface undulations in order to accomodate the overall applied strain. With these results as motivation, several avenues of further research are apparent.

Several questions directly follow the work begun in this thesis. They include, first and foremost, accounting for the material anisotropy in the constitutive relation of the finite element model. With this included, I would expect to achieve much closer agreement with experimental observations, particularly in terms of buckle wavelength. Additionally, in order to capture and understand the initiation/propagation behavior observed in experiment, a fully 3-D model is necessary. Both experimentally and theoretically, it would be useful to perform a systematic look at the effect of aspect ratio and height as the latter has been indicated to have an effect on buckle size [15]. All of these efforts would further the development of the consitutive relation for VACNTs.

Though not as rigorously addressed within this thesis, several other avenues of future study have become apparent throughout the discussion. Foremost, a quick, robust, and accurate method for measurement of VACNTs density or porosity in small quantities is essential for the cross-comparison of results. Even in macroscale samples, these measurements are imprecise due to the low density of VACNTs. Additionally, control of the CNT growth process will enable more systematic study of the microstructure-property relationship. In particular, it will lead to an understanding of why some materials show near full recovery while similar structures remain largely permanently deformed. These developments must proceed simultaneously with microstructure characterization techniques to determine tube number density gradients within structures and accurately measure the tortuosity of the tubes.

With respect to their application as energy dissipative materials, development of either growth techniques that increase CNT density or additives that strengthen the tube- to-tube interactions are necessary to give these structures increased strength in macroscale applications. VACNT composite materials are one example of this application which stands to benefit from understanding the tube-only response as begun in this thesis.

Bibliography

[1] K. Balasubramanian, M. Burghard, Biosensors based on carbon nanotubes, *Analytical and Bioanalytical Chemistry* **385**, 452–468 (2006).

[2] Z. Liu, S. Tabakman, K. Welsher, H. J. Dai, Carbon nanotubes in biology and medicine: in vitro and in vivo detection, imaging and drug delivery, *Nano Research* **2**, 85–120 (2009).

[3] P. M. Ajayan, O. Z. Zhou, Applications of carbon nanotubes, *Carbon Nanotubes* **80**, 391–425 (2001).

[4] M. C. LeMieux, et al., Self-sorted, aligned nanotube networks for thin-film transistors, *Science* **321**, 101–104 (2008).

[5] S. Iijima, Carbon nanotubes: past, present, and future, *Physica B: Condensed Matter* **323**, 1–5 (2002).

[6] G. D. Nessim, Properties, synthesis, and growth mechanisms of carbon nanotubes with special focus on thermal chemical vapor deposition, *Nanoscale* **2**, 1306–1323 (2010).

[7] J. Hone, *Dekker Encyclopedia of Nanoscience and Nanotechnology* (Marcel Dekker, Inc., 2004), chap. Carbon nanotubes: thermal properties, pp. 604–610.

[8] J. Che, T. Çağin, W. A. Goddard, Thermal conductivity of carbon nanotubes, *Nanotechnology* **11**, 65–69 (2000).

[9] M. Baxendale, The physics and applications of carbon nanotubes, *Journal of Materials Science: Materials in Electronics* **14**, 657–659 (2003).

[10] S. Iijima, C. Brabec, A. Maiti, J. Bernholc, Structural flexibility of carbon nanotubes, *Journal of Chemical Physics* **104**, 2089–2092 (1996).

[11] A. J. Hart, A. H. Slocum, Rapid growth and flow-mediated nucleation of millimeter-scale aligned carbon nanotube structures from a thin-film catalyst, *Journal of Physical Chemistry B* **110**, 8250–8257 (2006).

[12] E. Joselevich, H. Dai, J. Liu, K. Hata, A. H. Windle, Carbon nanotube synthesis and organization, *Carbon Nanotubes* **111**, 101–164 (2008).

[13] J. R. Raney, F. Fraternali, A. Amendola, C. Daraio, Modeling and *in situ* identification of material parameters for layered structures based on carbon nanotube arrays, *Composite Structures* (in press, 2011).

[14] S. Pathak, Z. G. Cambaz, S. R. Kalidindi, J. G. Swadener, Y. Gogotsi, Viscoelasticity and high buckling stress of dense carbon nanotube brushes, *Carbon* **47**, 1969–1976 (2009).

[15] A. A. Zbib, et al., The coordinated buckling of carbon nanotube turfs under uniform compression, *Nanotechnology* **19**, 175704 (2008).

[16] C. M. McCarter, et al., Mechanical compliance of photolithographically defined vertically aligned carbon nanotube turf, *Journal of Materials Science* **41**, 7872–7878 (2006).

[17] L. Ge, S. Sethi, L. Ci, P. M. A. Ajayan, A. Dhinojwala, Carbon nanotube-based synthetic gecko tapes, *Proceedings of the National Academy of Sciences of the United States of America* **104**, 10792–10795 (2007).

[18] L. F. Boesel, C. Greiner, E. Arzt, A. del Campo, Gecko-inspired surfaces: A path to strong and reversible dry adhesives, *Advanced Materials* **22**, 2125–2137 (2010).

[19] M. Xu, D. N. Futaba, T. Yamada, M. Yumura, K. Hata, Carbon nanotubes with temperature-invariant viscoelasticity from -196° to 1000°C, *Science* **330**, 1364–1368 (2010).

[20] J. Suhr, et al., Fatigue resistance of aligned carbon nanotube arrays under cyclic compression, *Nature Nanotechnology* **2**, 417–421 (2007).

[21] A. Misra, J. R. Greer, C. Daraio, Strain rate effects in the mechanical response of polymer-anchored carbon nanotube foams, *Advanced Materials* **21**, 334–338 (2009).

[22] C. Daraio, V. F. Nesterenko, S. Jin, W. Wang, A. M. Rao, Impact response by a foamlike forest of coiled carbon nanotubes, *Journal of Applied Physics* **100**, 064309 (2006).

[23] L. J. Gibson, M. F. Ashby, *Cellular Solids: Structure and Properties* (Cambridge University Press, 1999), 2nd ed.

[24] A. Y. Cao, P. L. Dickrell, W. G. Sawyer, M. N. Ghasemi-Nejhad, P. M. Ajayan, Supercompressible foamlike carbon nanotube films, *Science* **310**, 1307–1310 (2005).

[25] H. M. Manohara, et al., Carbon nanotube bundle array cold cathodes for THz vacuum tube sources, *Journal of Infrared, Millimeter and Terahertz Waves* **30**, 1338 (2009).

[26] T. J. Stark, G. M. Shedd, J. Vitarelli, D. P. Griffis, P. E. Russell, H_2O enhanced focused ion beam micromachining, *Journal of Vacuum Science & Technology B* **13**, 2565–2569 (1995).

[27] J. Hay, P. Agee, E. Herbert, Continuous stiffness measurement during instrumented indentation testing, *Experimental Techniques* **34**, 86–94 (2010).

[28] E. G. Herbert, W. C. Oliver, G. M. Pharr, Nanoindentation and the dynamic characterization of viscoelastic solids, *Journal of Physics D: Applied Physics* **41**, 074021 (2008).

[29] *Agilent G200 Reference Manual*.

[30] W. C. Oliver, G. M. Pharr, An improved technique for determining hardness and elastic-modulus using load and displacement sensing indentation experiments, *Journal of Materials Research* **7**, 1564 (1992).

[31] W. J. Wright, A. R. Maloney, W. D. Nix, An improved analysis for viscoelastic damping in dynamic nanoindentation, *International Journal of Surface Science and Engineering* **7**, 274–292 (2007).

[32] W. J. Wright, W. D. Nix, Storage and loss stiffnesses and moduli as determined by dynamic nanoindentation, *Journal of Material Research* **24**, 863 (2009).

[33] I. N. Sneddon, The relation between load and penetration in the axisymmetric boussinesq problem for a punch of arbitrary profiles, *International Journal of Engineering Science* **3**, 47–57 (1965).

[34] J. Y. Kim, J. R. Greer, Tensile and compressive behavior of gold and molybdenum single crystals at nanoscale, *Acta Materialia* **57**, 5245 (2009).

[35] M. Bedewy, et al., Collective mechanism for the evolution and self-termination of vertically aligned carbon nanotube growth, *Journal of Physical Chemistry C* **113**, 20576–20582 (2009).

[36] P. D. Bradford, X. Wang, H. Zhao, Y. T. Zhu, Tuning the compressive mechanical properties of carbon nanotube foam, *Carbon* **49**, 2834–2841 (2011).

[37] H. Malik, K. J. Stephenson, D. F. Bahr, D. P. Field, Quantitative characterization of carbon nanotube turf topology by SEM analysis, *Journal of Materials Science* **46**, 3119–3126 (2011).

[38] M. Pesenson, et al., Image processing application for cognition (IPAC) - Traditional and emerging topics in image processing in astronomy, *Astronomical Data Analysis Software and Systems XVII* **394**, 97–106 (2008).

[39] F. Salzenstein, C. Collet, Fuzzy Markov random fields versus chains for multispectral image segmentation, *IEEE Transactions on Pattern Analysis and Machine Intelligence* **28**, 1753–1767 (2006).

[40] D. R. Martin, C. C. Fowlkes, J. Malik, Learning to detect natural image boundaries using local brightness, color, and texture cues, *IEEE Transactions on Pattern Analysis and Machine Intelligence* **26**, 530–549 (2004).

[41] S. G. Armato, M. L. Giger, H. MacMahon, Automated detection of lung nodules in CT scans: preliminary results , *Medical Physics* **28**, 1552–1561 (2001).

[42] S. Mesarovic, et al., Mechanical behavior of a carbon nanotube turf, *Scripta Materialia* **56**, 157–160 (2007).

[43] A. Qiu, et al., Local and non-local behavior and coordinated buckling of CNT turfs, *Carbon* **49**, 1430–1438 (2011).

[44] S. B. Hutchens, L. J. Hall, J. R. Greer, In situ mechanical testing reveals periodic buckle nucleation and propagation in carbon nanotube bundles, *Advanced Functional Materials* **20**, 2338–2346 (2010).

[45] T. Tong, et al., Height independent compressive modulus of vertically aligned carbon nanotube arrays., *Nano letters* **8**, 511–5 (2008).

[46] O. Yaglioglu, Carbon nanotube based electromechanical probes, Ph.D. thesis, Massachusetts Institute of Technology (2007).

[47] Q. Zhang, et al., Viscoelastic creep of vertically aligned carbon nanotubes, *Journal of Physics D: Applied Physics* **43**, 315401 (2010).

[48] Y. Gogotsi, High-temperature rubber made from carbon nanotubes, *Science* **330**, 1332–1333 (2010).

[49] C. P. Deck, J. Flowers, G. S. B. McKee, K. Vecchio, Mechanical behavior of ultralong multiwalled carbon nanotube mats, *Journal of Applied Physics* **101** (2007).

[50] F. Fraternali, T. Blesgen, A. Amendola, C. Daraio, Multiscale mass-spring models of carbon nanotube foams, *Journal of the Mechanics and Physics of Solids* **59**, 89–102 (2011).

[51] V. A. Deshpande, N. A. Fleck, Isotropic constitutive models for metallic foams, *Journal of the Mechanics and Physics of Solids* **48**, 1253–1283 (2000).

[52] F. C. Bardi, H. D. Yun, S. Kyriakides, On the axisymmetric progressive crushing of circular tubes under axial compression, *International Journal of Solids and Structures* **40**, 3137–3155 (2003).

[53] F. C. Bardi, S. Kyriakides, Plastic buckling of circular tubes under axial compression - part I: Experiments, *International Journal of Mechanical Sciences* **48**, 830-841 (2006).

[54] F. C. Bardi, S. Kyriakides, H. D. Yun, Plastic buckling of circular tubes under axial compression - part II: Analysis, *International Journal of Mechanical Sciences* **48**, 842–854 (2006).

[55] A. Needleman, Material rate dependence and mesh sensitivity in localization problems, *Computer Methods in Applied Mechanics and Engineering* **67**, 69–85 (1988).

[56] V. Tvergaard, A. Needleman, K. K. Lo, Flow localization in the plane strain tensile test, *Journal of the Mechanics and Physics of Solids* **29**, 115–142 (1981).

[57] A. Needleman, V. Tvergaard, Finite elements for finite strain plasticity problems, *Plasticity of Metals at Finite Strain: Theory, Computation, and Experiment*, E. Lee, R. Mallett, eds. (Stanford Univ CA Div of Applied Mechanics, 1982), pp. 387–436.

[58] T. Belytschko, R. L. Chiapetta, H. Bartell, Efficient large scale nonlinear transient analysis by finite elements, *International Journal for Numerical Methods in Engineering* **10**, 579–596 (1976).

[59] D. Peirce, C. F. Shih, A. Needleman, A tangent modulus method for rate dependent solids, *Computers & Structures* **18**, 875–887 (1984).

[60] S. Pathak, J. R. Greer, *personal communication* (2011).

Chapter 7

Nucleation of Charged Macromolecule Solutions

The results presented in this chapter are a departure from the previous chapters and come from work performed under the guidance of Prof. Zhen-Gang Wang during the first few years of my graduate studies. They are included here for my own record as well as for the fact that it is work that I performed and feel contributed significantly to my education as a researcher.

As a whole, this initial work can be summarized as a mean field study of charged macromolecule solutions in spherical geometries. The work presented in the next few sections relates to homogeneous nucleation in this general type of solutions. Nucleation is an important mechanism of first-order phase transitions in which discontinuities occur in the order parameter(s) that characterize the two phases of a system. The initial phase may exist in a metastable state near its coexistence value (stable with respect to infinitesimal changes [1]) until a free energy barrier is overcome, allowing new phase formation. The transition is made possible by the lower free energy of the new phase. A homogeneous first-order phase transition takes place when a fluctuation in the order parameter(s) creates a nucleus large enough to overcome this barrier and grow into the more stable phase. These fluctuations are thermally induced, and the rate of nucleation varies depending on the height of the free energy barrier [2].

Nucleation phenomena have significance in a variety of areas of modern science, such as characterization of atmospheric nanoparticles [3], synthesis of zeolites [4], dewetting in thin films [5], and creation of high quality protein crystals [6], which all utilize homoge-

neous or heterogeneous nucleation mechanisms.

Classical and non-classical nucleation theories provide the means for gaining insight into these phenomena. Classical nucleation can be summarized as the formation of a uniform drop of the more stable phase within the uniform metastable phase. The lower free energy of the more stable phases encourages drop formation and growth, while formation of a surface limits this growth and formation up to some critical nucleus size. This chapter will discuss a proposed two-step mechanism based on the superposition of classical theory with more complex, long-range Coulomb interactions.

Additionally, the density functional theory based framework developed to treat the two-step nucleation mechanism can be adapted to a variety of charged macromolecule systems. One example that I began study on is a calculation of the osmotic pressure of a charged macomolecule confined to a sphere inspired by DNA in a viral capsid. Unfinished work toward this purpose is given in Appendix F.

7.1 Introduction

Weakly charged polyelectrolytes and colloidal particles are of great interest due to their rich phase behavior and relevance to biopolymers. For example, weakly charged polymer solutions below the coil/globule transition and charged colloidal suspensions share many properties with proteins in solution. Because protein structural determination still largely relies on X-ray diffraction from high quality protein crystals, protein crystallization from solution has been an area of active study. Recent work by Vekilov and co-workers on several protein solution systems [7–10] suggests a two-step nucleation mechanism, whereby the nucleation of the crystalline phase is preceded by the formation of a dense liquid-like precursor. This two-barrier scenario predicts different features than implied by the more common single-barrier model, such as the temperature dependence of the nucleation rate [6, 8]. The nature of the dense liquid-like clusters is not clear. However, in order for there to be two nucleation barriers in the formation of the bulk crystal phase, these clusters must correspond to a local free energy minimum with respect to the size (which is one of the key reaction coordinates). In this paper we explore one physical scenario due to long-ranged

Coulomb repulsion, which can give rise to metastable cluster intermediates in the transition between a dilute solution of monomers and a bulk, condensed phase.

The existence of large equilibrium clusters stabilized by charge has been demonstrated previously for a charged colloidal system in the absence of excess ions by Groenewold and Kegel [11]. In this case, the driving force for condensation due to short-range van der Waals interactions is checked by the unfavorable long-range electrostatic repulsion between the particles that increases superlinearly with the number of particles in a cluster, thus preventing the formation of a bulk condensed phase. In contrast, we are interested in clusters that can further nucleate a bulk condensed phase. We propose that the presence of excess ions that neutralize and screen charges on the monomers in solution provides the needed mechanism for allowing the formation of a bulk liquid phase. We find that for some combinations of parameters, a bulk condensation transition proceeds by going through a metastable cluster state with a well-defined cluster size, and that the metastable cluster itself is formed through nucleation, i.e., the overall process involves two nucleation barriers. While our model may not be directly applicable to the crystallization of proteins from solution, we believe the mechanism for condensation via metastable cluster intermediates to be quite general, though possibly confined to a small region of the phase diagram, in systems having short-range attraction and long-range repulsion, such as solutions of polyelectrolytes [12], charged colloids [13], and globular proteins [14], which can exhibit both micro and macro phase separations [15], with the former involving clusters of finite sizes.

Conditions giving rise to the metastable intermediate cluster behavior as well as the nature of cluster formation are analyzed in the following sections. Our analysis employs a simple capillarity model for the cluster that is commonly used in classical nucleation theory, combined with the Poisson-Boltzmann equation for treating the electrostatic interactions. In Sec. 7.2.1, we briefly review the classical nucleation theory and describe its application to our system. In Sec. 7.2.2, the electrostatic contribution to the cluster free energy is calculated using the Poisson-Boltzmann approach. We present the results of our calculation in Sec. 7.3: We show the free energy of cluster formation as a function of size and demonstrate several scenarios with respect to the stability of the intermediate clusters for a specific set of parameters. The formation of clusters with preferred size is shown to

be similar to the formation of micelles and a concentration similar to the critical micelle concentration can be identified. Section 7.4 provides a summary of our results with some concluding remarks.

7.2 Model Formulation

We consider a dilute solution of weakly charged particles (henceforth called unimers in their unclustered state), which can be globular proteins, polyelectrolyte globules, or colloidal particles, each carrying an electric charge q. Without loss of generality, we take the charge on the unimers to be positive. The system is maintained electrically neutral by counter-ions that we assume to be monovalent for simplicity. In addition, the system contains ions from salt, also assumed to be monovalent. Short-range attractions, e.g., van der Waals or hydrophobic interactions, provide the driving force for the formation of clusters and for potential condensation into a bulk phase; a schematic is shown in Fig. 1. As the focus of this work is on the metastable liquid-like clusters, we will not address issues directly related to the formation of a crystal phase.

We study the formation of clusters and the eventual condensation into a bulk phase by taking a nucleation perspective, i.e., by constructing the appropriate free energy of formation as a function of the size of the clusters. Since a cluster is formed from the surrounding solution of unimers and in the presence of small mobile co-ions and counter-ions, it is convenient to treat the volume enclosing the cluster as an open system, with chemical potentials μ, μ_+, and μ_-, respectively for the unimers, the co-ions and the counter-ions. The appropriate free energy is the change in the grand potential upon the formation of a cluster from a uniform solution, defined as

$$\begin{aligned}\Delta W &= W_c(m;\mu,\mu_+,\mu_-,V) - W_s(\mu,\mu_+,\mu_-,V) \\ &= F_c(m,n_+,n_-,V) - m\mu - n_+\mu_+ - n_-\mu_- + (p_s+p_+ + p_-)V. \qquad (7.1)\end{aligned}$$

In this expression, $F_c(m,n_+,n_-,V)$ is the Helmholtz free energy of a charged cluster of size m, with n_+ co-ions and n_- counter-ions, and $W_s(\mu,\mu_+,\mu_-,V) = -(p_s + p_+ +$

$p_-)V$, with p_s, p_+, p_-, the (osmotic) pressure of the unassociated unimers, the co-ions and counter-ions, respectively; we have implicitly assumed that these pressures are additive for the purpose of calculating W_s, which amounts to making an ideal solution (in the sense of Henry's law) approximation for these species. Since we do not explicitly consider the solvent, for simplicity of terminology, we will often refer to the dilute solution as the vapor, and the osmotic pressure as just the pressure.

We treat the cluster using a simple capillary model, i.e., taking it as a spherical of liquid of uniform density with a sharp interface. While this is clearly a crude approximation and there are many recognized pitfalls in its application to nucleation, for our present purpose, the model is sufficient to capture most of the essential physics of interest without complications that would be introduced in a more realistic but mathematically more involved representation and solution.

With the use of the capillary model, it is convenient to separate the free energy change into two parts: a contribution due to the short-range interactions in a hypothetical uncharged system and a contribution due to the electrostatic effects. Hereafter we will use the word "uncharged" when referring to the hypothetical uncharged system lacking co-ions and counter-ions. We write Eq. (7.1) as

$$\begin{aligned}\Delta W &= \Delta W^{(0)} + \Delta W^{(e)} \\ &= [F_c^{(0)}(m,V) - m\mu^{(0)} + p_s V] \\ &+ [F_c^{(e)}(m,n_+,n_-,V) - n_+\mu_+ - n_-\mu_- + (p_+ + p_-)V - m\mu^{(e)}],\end{aligned} \tag{7.2}$$

where $F_c^{(0)}$ and $F_c^{(e)}$ are, respectively, the uncharged and electrostatic parts of the Helmholtz free energy of the cluster (the translational entropy of the cluster is not included), and $\mu^{(0)}$ and $\mu^{(e)}$, are respectively the uncharged and electrostatic parts of the chemical potential of the unimers ($\mu^{(0)} + \mu^{(e)} = \mu$), with the translational contribution contained in $\mu^{(0)}$.

We now proceed to calculate these two free energy changes separately. We treat the uncharged part using the classical nucleation theory and the electrostatic part using the Poisson-Boltzmann approach.

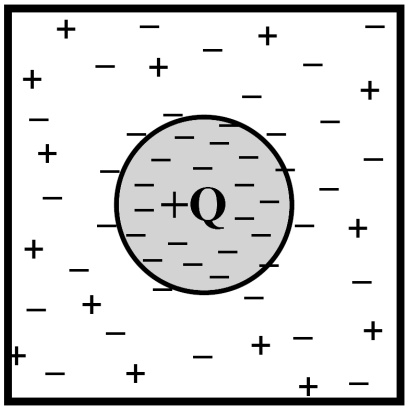

Figure 7.1: Schematic of a cluster of charge $+Q$ within a monovalent co-ion and counter-ion reservoir.

7.2.1 Free Energy without Electrostatic Interaction

We calculate the free energy of formation for an m-sized, uncharged cluster using classical nucleation theory. The classical nucleation theory makes the simplistic assumption that the free energy of a cluster can be dissected into a negative bulk free energy and a positive interfacial free energy. Thus the grand free energy of a dense cluster of volume V_c having interfacial area A_c is

$$W_c = -p_c(\mu^{(0)})V_c + A_c\gamma,$$

where p_c is the pressure (the negative of the grand potential density) inside the cluster and γ is the interfacial tension. The grand potential change upon creating a cluster of volume V_c in an observational volume V from a homogeneous solution of unimers with pressure p_s is then

$$\begin{aligned}\Delta W^{(0)} &= -V_c p_c(\mu^{(0)}) + A_c\gamma - (V - V_c)p_s(\mu^{(0)}) + V p_s(\mu^{(0)}) \\ &= -V_c\left[p_c(\mu^{(0)}) - p_s(\mu^{(0)})\right] + A_c\gamma. \end{aligned} \tag{7.3}$$

We now write the pressure difference in terms of the supersaturation relative to the phase coexistence pressure of the hypothetical uncharged system.

To do so, we utilize the thermodynamic relation $\partial\mu/\partial p|_T = 1/\rho$, where ρ is the density. It follows that the pressure difference is related to the difference in chemical potential through $p_c - p_s = (\rho_c - \rho_s)(\mu^{(0)} - \mu^{(0)}_{\text{coex}}) \approx \rho_c(\mu^{(0)} - \mu^{(0)}_{\text{coex}})$ where $\mu^{(0)}_{\text{coex}}$ is the chemical po-

tential of the hypothetical uncharged system at vapor-liquid coexistence at which $p_c = p_s$. Finally, assuming ideal gas behavior for the vapor phase, the chemical potential difference can be written as $\mu^{(0)} - \mu^{(0)}_{\text{coex}} = kT \ln(p_s/p_{\text{coex}}) \equiv kT \ln(S)$. The resulting free energy of formation is

$$\begin{aligned} \Delta W^{(0)} &= -kT\rho_c V \ln(S) + A_c\gamma \\ &= -mkT \ln(S) + A_c\gamma. \end{aligned} \tag{7.4}$$

To use Eq. (7.4) for the free energy of formation for a cluster of m unimers, the dependence of the surface area on m needs to be specified. In the case of coalescing globular polyeletrolytes, if we assume that the globules are uniform spheres of radius R_1 and that there is no change in the monomer density (as the polymers can deform and interpenetrate) upon the formation of a cluster of radius R_c, then clearly

$$m = \left(R_c/R_1\right)^3. \tag{7.5}$$

On the other hand, hard spherical colloids pack less densely and therefore this expression would need to be modified by inclusion of a packing factor. Throughout the rest of the paper, we assume the former so that

$$A_c(m) = 4\pi R_1^2 m^{2/3}. \tag{7.6}$$

The expression for $\Delta W(m)$ as given by Eq. (7.4) and Eq. (7.6) contains one of the well-known inconsistencies of classical nucleation theory: the existence of a finite free energy of formation for a cluster of one monomer. Resolution of this inconsistency is subtle and has been discussed intensely by Lothe and Pound [16], Reiss and Katz [17, 18], and more recently by Kusaka [19]. Rather than make use of these more rigorous methods, which are unnecessary given the nature of the approximations we are making, we utilize a simple corrected form that has been artificially shifted by taking the free energy relative to

a cluster of size one,

$$\Delta W^{(0)} = -kT\ln(S)\,(m-1) + 4\pi R_1^2\gamma\left(m^{2/3}-1\right). \tag{7.7}$$

We note that this shift has no consequence on the main results of this study.

Equation (7.7) is the expression for the free energy of formation of a cluster of m unimers for an uncharged system. For $S > 1$, this expression predicts the well-known behavior for nucleation of a dense liquid phase through a single nucleation barrier. No metastable cluster is allowed. We next discuss the electrostatic interaction that provides the necessary balancing force that makes the metastable clusters possible.

7.2.2 Free Energy of Electrostatic Interactions

It is easy to see how Coulomb repulsion can lead to a preferred cluster size. We first consider the case of no counter-ions and no added salt.

In a cluster of m unimers each having a point charge q, the total Coulomb interaction is given by

$$E_{\mathrm{c}} = \frac{1}{2}\sum_{i,j\neq i}\frac{q^2}{4\pi\varepsilon_0\epsilon R_{ij}},$$

where R_{ij} is the distance between charges i and j, ϵ is the dielectric constant of the medium (assumed uniform throughout V here), and ε_0 is the vacuum permittivity. Since the average distance between the charges scales as the size of the cluster R_c, the electrostatic interaction in a cluster of m charged unimers scales as

$$E_{\mathrm{c}} \sim \frac{q^2}{8\pi\varepsilon_0\epsilon R_c}m(m-1) \sim \frac{q^2}{8\pi\varepsilon_0\epsilon R_1}m^{5/3}, \tag{7.8}$$

where the second part follows from the relationship between the size of the cluster and the size of the unimer, Eq. (7.5), and we have assumed m to be much larger than one.

When combined with the neutral part of the free energy $\Delta W^{(0)}$ from Eq. (7.4), we see that as the cluster size (number of unimers) increases, the free energy first increases due to the positive surface free energy term, then decreases because of the negative bulk free energy term, but increases again due to the positive superlinear electrostatic energy term,

creating a free energy minimum at some intermediate size

$$\Delta W \sim 4\pi R_1^2 \gamma m^{2/3} - mkT\ln(S) + \frac{q^2}{8\pi\,\varepsilon_0 \epsilon R_1} m^{5/3};$$

this is in fact the same argument as given by Groenewold and Kegel [11].

While this simple scaling analysis predicts the existence of clusters with a preferred size, the superlinear dependence of the free energy on m for large clusters excludes the possibility of a dense bulk phase. Thus these mesoscopic clusters are fully stable. A dense bulk phase is made possible by the combined neutralization and screening by the co-ions and counter-ions. It is expected that bare Coulomb repulsion is dominant when the cluster size is small, while neutralization and screening become effective when the cluster size becomes sufficiently large, making the electrostatic free energy extensive again. Figure 7.2 shows the crossover from the $m^{5/3}$ scaling to the linear scaling of the electrostatic free energy as a function the cluster size. We now proceed with a more detailed description of the calculation for the electrostatic part of the free energy of cluster formation.

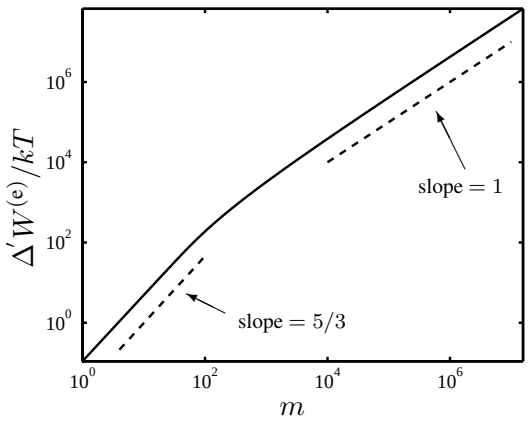

Figure 7.2: An example of the size dependence of the free energy of electrostatic interaction ($\Delta' W^{(e)}$) depicting $m^{5/3}$ and m behavior for small and large clusters respectively. This curve was obtained using cluster charge density, $\rho_0 l_B^3 = 0.08$, Debye screening length, $\lambda/l_B = 0.15$, and dielectric constant ratio, $\epsilon_1/\epsilon_2 = 0.2$.

Consistent with our use of the uniform liquid model for the cluster, we assume the charge distribution due to the clustering unimers to be continuous and uniform inside the cluster with a constant charge density ρ_0. This *jellium* model is similar to that used by

Sear and Warren [20] in their calculation of the electrostatic contribution to planar surface tension. We then include co-ions and counter-ions that equilibrate with the charged cluster with ion density profiles c_+ and c_-. (We make the simplifying but inconsequential assumption that the cations from the salt are the same as the counter-ions for the charged clusters of interest.) Superposition of these charge density profiles with the step-function charge density profile of the cluster results in an overall charge density profile $\rho(\mathbf{r}) = \rho_0 e\,\theta(R_c - r) + ec_+(r) - ec_-(r)$, where $\theta(R_c - r)$ is a step function equal to one inside the cluster and zero outside and e is the elementary unit of charge. Re-expressing Coulomb's law in terms of a variational integral by introducing the electrostatic potential $\psi(\mathbf{r})$ leads to the following expression for the electrostatic energy:

$$E_{\mathrm{c}}[\rho(\mathbf{r}), \psi(\mathbf{r})] = \int d\mathbf{r} \left\{ \rho(\mathbf{r})\psi(\mathbf{r}) - \frac{\varepsilon_0 \epsilon}{2} \left[\nabla\psi(\mathbf{r})\right]^2 \right\}. \tag{7.9}$$

The total electrostatic free energy must include the translational entropy of the mobile free ions. Since the volume surrounding the cluster is semi-open: closed with respect to the condensed cluster unimers, but open with respect to the co-ions and counter-ions, we add the grand free energy due to these mobile ions. Treating the ions as volumeless, non-interacting particles in contact with a reservoir of chemical potential μ_2, we have the total electrostatic free energy of the cluster as:

$$\begin{aligned} W^{(\mathrm{e})} = & \int_V d\mathbf{r} \big\{ \rho(\mathbf{r})\psi(\mathbf{r}) - \frac{\varepsilon_0 \epsilon}{2} \left[\nabla\psi(\mathbf{r})\right]^2 \big\} \\ & + kT \int_V d\mathbf{r} \big\{ c_+ \ln(c_+ a^3) - c_+ - c_+ \beta\mu_2 \big\} \\ & + kT \int_V d\mathbf{r} \big\{ c_- \ln(c_- a^3) - c_- - c_- \beta\mu_2 \big\}. \end{aligned} \tag{7.10}$$

The system volume (V) is taken to be large enough to include the cluster and any variations in ion concentration. The lengthscale, a, assumed to be the same for both types of ions, is of no consequence in the results because of cancellation with its appearance in the reservoir chemical potential, $\mu_2 = kT \ln(c_\infty a^3)$.

The spherically symmetric equilibrium ion concentration profiles c_+ and c_- and the electrostatic potential are obtained by extremization of the free energy in Eq. (7.10) with

respect to these variables. Variation with respect to the ion concentrations yields

$$c_+(r) = c_\infty \exp\left[-\beta e\psi(r)\right]$$

$$c_-(r) = c_\infty \exp\left[\beta e\psi(r)\right],$$

where β is the inverse thermodynamic temperature $1/kT$. Substitution of these relations back into the free energy Eq. (7.10) and subsequent variation with respect to $\psi(\mathbf{r})$ results in the Poisson-Boltzmann equation,

$$\varepsilon_0\epsilon\nabla^2\psi(r) = -\rho_0 e\,\theta(R_c - r) + 2kTc_\infty \sinh\left[\beta e\psi(r)\right]. \tag{7.11}$$

To reduce the number of independent parameters and gain better insight into the relative importance of the various physical effects, it is convenient to non-dimensionalize the equations. To this end, we introduce the Debye screening length, $\lambda = (8\pi b c_\infty)^{-1/2}$, and the Bjerrum length, $l_B = \beta e^2/(4\pi\varepsilon_0\epsilon)$. We elect to express the length r in units of l_B as opposed to λ to avoid the complication of an ion concentration dependent length. Similarly, the charge density ρ_0 is non-dimensionalized as $\rho_0 l_B^3$. Finally, $\beta e\psi$ is the resulting dimensionless electrostatic potential, ξ. The free energy of a charged cluster in an ion reservoir expressed in terms of the above dimensionless variables is

$$W^{(\mathrm{e})} = -kT\int_V r^2 dr\left\{\frac{1}{2}\left[\nabla_r\xi\right]^2 + \left(\frac{l_B}{\lambda}\right)^2\cosh\left[\xi(r)\right] - 4\pi\rho_0 l_B^3\xi(r)\,\theta(R_c - r)\right\}. \tag{7.12}$$

The corresponding non-dimensionalized Poisson-Boltzmann equation is

$$-\nabla^2\xi + \left(\frac{l_B}{\lambda}\right)^2\sinh\left[\xi(r)\right] = 4\pi\rho_0 l_B^3\,\theta(R_c - r). \tag{7.13}$$

The ratio l_B/λ is seen to be a natural parameter measuring the importance of screening. It can be easily verified that in the limit of $l_B/\lambda = 0$ or $\lambda/l_B \to \infty$, we recover the electrostatic energy of a uniformly charged sphere.

For simplicity of presentation, thus far we have considered the dielectric constant to be uniform. In reality, the two regions inside and outside the cluster will have different di-

electric constants, ϵ_1 and ϵ_2, respectively. Apart from modifying the energy due to change in the electrostatic potential, the difference in dielectric constant also results in a preferred solubility of the ions within the region of higher dielectric constant due to difference in the reference chemical potential in the two different media. This difference may be approximated using the Born solvation energy. The Born solvation energy is the free energy change in transferring an ion with charge q and radius a from a medium with dielectric constant ϵ to a medium with dielectric ϵ_0 and is written

$$-\frac{q^2}{8\pi a\varepsilon_0}\left(\frac{1}{\epsilon_0}-\frac{1}{\epsilon}\right).$$

Thus the difference in chemical chemical potential between an ion in dielectric medium one versus an ion in dielectric medium two is given by

$$\begin{aligned}\Delta\mu^* = \mu_1 - \mu_2 &= -\frac{q^2}{8\pi a\varepsilon_0}\left(\frac{1}{\epsilon_2}-\frac{1}{\epsilon_1}\right)\\ &= -\frac{q^2}{8\pi a\varepsilon_0\epsilon_2}\left(\frac{\epsilon_2}{\epsilon_1}-1\right).\end{aligned} \tag{7.14}$$

In our case, ϵ_1/ϵ_2 is always less than one. Therefore, $\Delta\mu^*$ is always positive and it is energetically unfavorable for the co-ions and counter-ions to enter the lower dielectric medium within the cluster.

An analogous derivation to that just described can be performed in which the effect of a difference in the dielectric constant between the cluster and the solvent is taken into account. It requires two additional dimensionless groups, the ratio of the dielectric constants ϵ_1/ϵ_2, and the difference in reference chemical potentials, $\beta\Delta\mu^* = \beta\mu_1^* - \beta\mu_2^*$. The expressions for this derivation are given in E. It is the solutions to these equations that are presented in this section and Sec. 7.3.

The Poisson-Boltzmann equation is solved numerically using the Runge-Kutta method. Boundary conditions arise from neutrality at an infinite distance from the cluster, $\xi \rightarrow 0$ as $r \rightarrow \infty$, and spherical symmetry, $\partial\xi/\partial r \rightarrow 0$ as $r \rightarrow 0$. Additionally, across the cluster boundary, we have the continuity of the electric potential, $\xi(R_c^-) = \xi(R_c^+)$, and the electric displacement field, $-\epsilon_1\nabla\xi(R_c^-) = -\epsilon_2\nabla\xi(R_c^+)$.

Solution of the differential equation that includes the dielectric constant discontinuity (Eq. (E.2)) results in potential profiles and corresponding total charge density profiles like those shown in Fig. 7.3 for clusters of different sizes, m. It is clear from these figures that for small cluster sizes, e.g., $m = 10$, the charge of the cluster is essentially the bare charge carried by the aggregating molecules, and the corresponding electrostatic potential is barely distinguishable from that obtained from solving the simple unscreened Poisson equation (with an inverted parabolic potential profile). For $m = 100$, we find that there is now appreciable neutralization of the charge by the counter-ions in the center of the cluster and the potential in the center nearly reaches the bulk asymptotic value. For the larger clusters, $m = 10^3$ and $m = 10^4$, the neutralization of charge in the interior of the cluster is almost complete. The charge that is not neutralized is distributed primarily near the edge of the cluster with an oppositely charged region in the immediate vicinity outside the cluster. The potential profile becomes essentially flat inside the cluster for these larger sized clusters and decays to zero with a lengthscale on the order of the Debye screening length. For clusters whose radii are much larger than the Debye screening length, it is possible to write the electrostatic free energy of the cluster as a volume term and an interfacial term, with a negative interfacial tension [20, 21].

The crossover from the small cluster to the large cluster behavior in the electrostatic potential and charge density is consistent with the crossover in the free energy shown in Fig. 2. It is this crossover that is largely responsible for the two-barrier nucleation scenario in the condensation of the molecules.

7.2.3 Total Free Energy

By construction, we have written the total free energy of cluster formation as composed of an uncharged part and an electrostatic part. Referring to Eq. (7.2), the free energy expression derived in Sec. 7.2.1 accounts for the terms in the first bracket of the second equality in Eq. (7.2), while the electrostatic free energy described in the last section corresponds to the first three terms in the second bracket. It is straightforward to include the remaining bulk osmotic pressure terms due to the co-ions and counter-ions in a uniform solution by

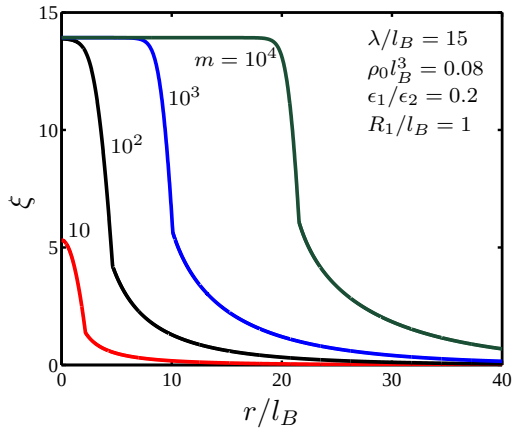

(a) Electrostatic Potential

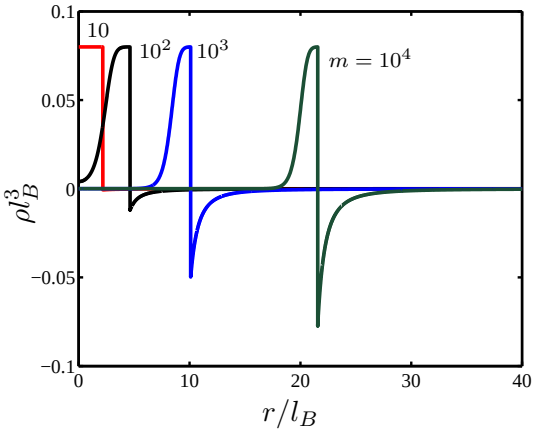

(b) Total Charge Density

Figure 7.3: The electrostatic potential profiles (a) and total charge density profiles (b) obtained from the Poisson-Boltzmann equation (Eq. (E.2)) for cluster radii of increasing radius.

defining a free energy difference $\Delta' W^{(\mathrm{e})}$ using $W^{(\mathrm{e})}$ from Eq. (7.10) yielding

$$\Delta' W^{(\mathrm{e})} = W^{(\mathrm{e})} - kT \int_V d\mathbf{r}\ 2c_\infty, \tag{7.15}$$

which has no effect on solution of the governing differential equations. To complete our total free energy, we need to account for the last term in the second bracket of Eq. (7.2). By our definition, $\mu^{(e)}$ is the excess chemical potential of the unassociated unimers due to the electrostatic self interaction within the globular cluster. We treat the unimer in a manner identical to that for the cluster, i.e., regarding it as a uniformly charged sphere surrounded by mobile co-ions and counter-ions. The excess chemical potential is then logically identified as the special case of Eq. (7.15) when $m = 1$. The total electrostatic

free energy that accounts for all the terms in the second equality of Eq. (7.1) is then

$$\Delta W^{(\mathrm{e})} = \Delta' W^{(\mathrm{e})}(m) - m\Delta' W^{(\mathrm{e})}(1). \tag{7.16}$$

and the total free energy of cluster formation is

$$\Delta W = \Delta W^{(0)} + \Delta W^{(\mathrm{e})}. \tag{7.17}$$

This expression yields the free energy of formation of an m-sized cluster for a given set of parameters: λ/l_B, R_1/l_B, $\rho_0 l_B^3$, ϵ_1/ϵ_2, the interfacial tension γ, and the supersaturation S. Its behavior as a function of m provides information about the thermodynamic stability of the clusters, their size distribution, and their role in the formation of a dense bulk phase.

7.2.4 Bulk Phase Coexistence

In Sec. 7.2.1, the supersaturation S is introduced with reference to the coexistence vapor pressure of a hypothetical uncharged system. For this hypothetical system, a bulk condensation occurs at $S = 1$. The addition of electrostatic interactions shifts the value of the coexistence supersaturation from one, for an uncharged system, to a value greater than one, for the charged system. Its new value is determined by the condition that the extensive terms ($\propto m$) in the total free energy of cluster formation must sum to zero in the limit of $m \to \infty$; this is equivalent to the equality of the grand potential between the dilute solution of unimers and the condensed phase (within the same volume), i.e, the equality of (osmotic) pressure. From our expression for the total free energy, it is straightforward to show that the coexistence "supersaturation" (that is the supersaturation relative to the coexistence pressure of a hypothetical uncharged system) is given by:

$$S_{\text{coex}} = \exp\left[\frac{1}{kT}\left(w_{\text{bulk}}^{(\mathrm{e})} - \Delta' W^{(\mathrm{e})}(1)\right)\right],$$

where $w_{\text{bulk}}^{(\mathrm{e})} = \lim_{m\to\infty} \Delta' W^{(\mathrm{e})}(m)/m$. The full algebraic expression for $w_{\text{bulk}}^{(\mathrm{e})}$ is somewhat cumbersome and is given by the following expression where, in the limit of cluster size ap-

proaching infinity, ξ is constant $\left(= \sinh^{-1}\left[4\pi\rho_0 b^3 \left(\frac{\lambda}{l_B}\right)^2 e^{-\beta\Delta\mu^*}\right]\right)$, and the free energy becomes

$$\frac{w^{(\mathrm{e})}_{\mathrm{bulk}}}{m} = -kT\left(\frac{l_B}{\lambda}\right)^2 \frac{R_1^3}{3}\left[e^{-\beta\Delta\mu^*}\sqrt{1+\left(4\pi\rho_0 l_B^3\left(\frac{\lambda}{l_B}\right)^2 e^{\beta\Delta\mu^*}\right)^2}\right.$$
$$\left. - 4\pi\rho_0 l_B^3\left(\frac{\lambda}{l_B}\right)^2 \sinh^{-1}\left(4\pi\rho_0 l_B^3\left(\frac{\lambda}{l_B}\right)^2 e^{-\beta\Delta\mu^*}\right)\right].$$

Note that while there exists an algebraic form for $w^{(\mathrm{e})}_{\mathrm{bulk}}$, we still must solve the Poisson-Boltzmann equation to obtain the electrostatic energy of a unimer, $W^{(\mathrm{e})}(1)$.

We now have a reference with which to judge whether any clusters formed are metastable with respect to the dense-liquid phase, and therefore can take part as an intermediate in bulk phase formation.

7.3 Results and Discussion

Before presenting and discussing the main results of this study, we first revisit the physics leading to cluster formation and discuss the limits of their existence and their relation to bulk phases. As discussed in Sec. 7.2.2 and illustrated in Fig. 7.2, there are two main regimes associated with the electrostatic part of the free energy of formation, the superlinear ($m^{5/3}$) and the linear (m) regimes, corresponding to highly charged and largely neutralized clusters, respectively. The interplay between the location and magnitude of these regimes, the surface tension, and the solution supersaturation gives rise to several possible behaviors involving preferred-size clusters.

In order to obtain the two-barrier free energy curve we discuss here, the electrostatic and the uncharged free energies must be of the same order of magnitude. This results in rich phase behavior, but limited cluster sizes. The size of clusters is limited by the size range of the $m^{5/3}$ region in Fig. 7.2. In other words, clusters acting as metastable intermediates can be no larger than the size (m) at which the $\Delta W^{(\mathrm{e})}$ dependence changes from $m^{5/3}$ to linear. While very large clusters ($m > 10^4$) are predicted under certain conditions, we find that these clusters do not exist in a state metastable to the bulk liquid, i.e, the bulk liquid

state does not exist for these conditions. It may be possible that these large clusters are metastable with respect to a more stable crystalline state; this possibility will be examined in future work.

We now briefly discuss the parameters used in our model. An ion concentration c_∞ in the range of 0.8 M–8 mM in water (physiological salt concentration $= 0.2$ M) with a dielectric constant of 80 (ϵ_2 in our notation) results in the parameter λ/l_B ranging from 0.25 to 25, the Bjerrum length being 7 Å. We choose $\lambda/l_B = 15$ for our representative calculations. The dielectric constant within proteins, ϵ_1, is difficult to estimate; however values from 4 to 20 [22] have been theoretically estimated and used, resulting in corresponding ϵ_1/ϵ_2 values of 0.05–0.25. In our representative calculations, we set $\epsilon_1/\epsilon_2 = 0.2$. Decreasing ϵ_1/ϵ_2 increases the electrostatic free energy $W^{(e)}$ as well as results in a slight increase in the cluster size at which crossover between the $m^{5/3}$ and m behavior occurs. For the interfacial tension, we use $\gamma = 0.95\ kT/l_B^2 = 8$ mN/m, which is intermediate between a clean oil/water interface (50 mN/m) and tensions measured in colloidal phases (1–20 μN/m) [20]. We use a low charge density $\rho_0 l_B^3 = 0.08$. This charge density is on the same order of magnitude as many globular proteins. Low charge density is necessary in order to still allow for a bulk condensation. In the case of polyelectrolytes, the low charge density is also necessary to ensure that the collapsed polymer is in the globular regime, not in the necklace regime [23]. Finally, we choose $R_1/l_B = 1$ for the unimer size. We choose this size because it most clearly illustrates the behavior we wish to highlight. This size is on the smaller end even for proteins. For larger unimer size, the range of the superlinear dependence of the free energy electrostatic interaction decreases, thus decreasing the aggregation number of the metastable clusters, other conditions being equal. On the other hand, smaller sizes for charged unimers are relevant for other systems, e.g., in zeolite or nanoparticle synthesis [24, 25].

The main result of this study is summarized in Fig. 7.4, which shows the free energy of formation as a function of the cluster size for increasing values of the supersaturation (or equivalently the unimer concentration). At small supersaturation, the only minimum of the free energy curve occurs at $m = 1$. As supersaturation increases beyond some critical value (curve A), a local minimum in the free energy for a finite-sized cluster first begins

to develop. As the concentration of unimers increases, the free energy of the finite-sized cluster decreases, with an attendant shift in the location of the minimum to larger cluster size. When the supersaturation exceeds that corresponding to the vapor-liquid coexistence (curve B, indicated by Coex.), the global free energy minimum is that of the bulk liquid phase (i.e., infinite cluster size) and the vapor phase becomes metastable with respect to the stable bulk liquid. However, the formation of the bulk liquid phase requires overcoming two barriers, the first for the formation of the finite-sized clusters and the second for the clusters at the free energy minimum to grow into the bulk liquid phase. We thus have the scenario of a two-step nucleation process with the clusters of finite sizes acting as long lived metastable intermediates. The lifetime of these metastable clusters is determined by the barriers on the two sides of the minimum. For the range of parameters we use in our study, the typical free energy barrier for the dissolution of the clusters is on the order of 10 kT, depending on the supersaturation. The barrier to the formation of the bulk liquid phase can be quite large (which also implies large critical nuclei), again depending on the supersaturation, due to the strong electrostatic interactions. In reality, these large clusters are more likely to take other shapes, such as disks or rods [11], to decrease the electrostatic repulsions; this would lead to a decrease in the second nucleation barrier. For sufficiently large supersaturation, the second nucleation barrier disappears (curve F) and the condensation into a liquid bulk phase proceeds through a simple single-barrier scenario.

In addition to the metastable liquid-like clusters that can be intermediates in the bulk phase transition, in other words, that result in two nucleation barriers like those shown in Fig. 7.4, our model also predicts the existence of clusters that are metastable or stable with respect to the dilute solution, with no possibility for bulk liquid formation. [We clarify that the terms "stable" and "metastable" are used in the sense of Fig. 7.4: The clusters are considered stable with respect to the solution phase if the minimum in their free energy of formation from the solution phase is negative (curve E for example), and metastable if the minimum of the free energy of formation is positive (curve C). Curve D denotes the limit of this stability.] The case of metastable clusters with respect to the unimer solution phase, whether a bulk liquid exists or not, may be reasonably described by our model, as the number density of the clusters formed will be small due to the positive free energy required

for their formation. In the case where the clusters are more stable than the solution of unimers, we expect that the clusters will appear in large numbers; cluster-cluster as well as unimer-cluster interactions become important and our picture of non-interacting clusters is no longer valid. In all likelihood this latter case would correspond to microphase separation, which is beyond the scope of this work.

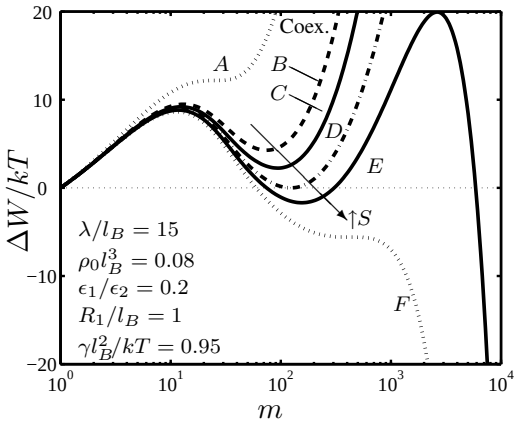

Figure 7.4: Total free energy of cluster formation for six increasing values of supersaturation (S).

Figure 7.4 demonstrates that several phase transition scenarios are possible as the supersaturation varies. Clearly the transition scenarios will depend significantly on the extent of screening. Since the unimer concentration is proportional to S, and the reservoir ion concentration is proportional to $(l_B/\lambda)^2$, these serve as the natural controlling parameters in experiments. We thus present in Fig. 7.5 a generalized "phase diagram" in S and λ/l_B that illustrates the different phase transition scenarios. In this "phase diagram," the dash line designates the vapor-liquid coexistence. Region II corresponds to stable dilute solutions, while in region I a supersaturated dilute solution phase will turn into the bulk liquid phase via the normal one barrier nucleation. Note that region I corresponds to high screening and/or high supersaturation. The region bounded by the two dotted lines is the region where finite-sized clusters have a free energy minimum. With reference to Fig. 7.4, the lower dotted line corresponds to the first appearance of a shoulder on the left (curve A), while the upper dotted line corresponds to the disappearance of the barrier on the right (curve F). The dash-dot line denotes the supersaturation at which the free energy of forma-

tion of the clusters becomes zero (curve D). Thus, regions III and VI correspond to clusters that have lower free energy than the unimers. As alluded to in the last paragraph, the energetic favorability for forming the clusters will lead to a high concentration of clusters which is outside the regime of validity of this study. Regions IV and V are the most interesting from the perspective of this work. Region IV corresponds to metastable preferred-size clusters that cannot grow into bulk liquid, while in region V the metastable clusters serve as intermediates to the formation of the bulk liquid. A two-barrier nucleation mechanism operates in region V.

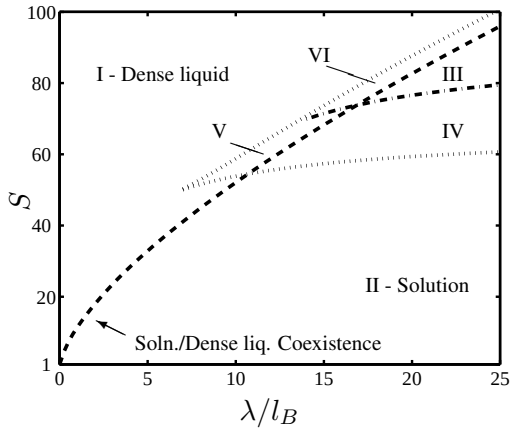

Figure 7.5: The "phase diagram" for a unimer radius of 1 l_B, dielectric ratio, ϵ_1/ϵ_2, of 0.2, charge density, $\rho_0 l_B^3$, of 0.08, and surface tension, $\gamma = 0.95\ kT/l_B^2$.

The formation of the metastable clusters with preferred sizes is akin to the formation of micelles in surfactant solutions. To explore this connection, we calculate the cluster size distribution and the partitioning of the molecules between unimers and clusters. Assuming no cluster-cluster and unimer-cluster interactions, the cluster size distribution, i.e, the number density of m-sized clusters is directly related to the free energy of formation, $\Delta W(m)$ [26]:

$$\rho_m \propto e^{-\beta \Delta W(m)} \tag{7.18}$$

The proportionality involves a volume scale that arises from evaluation of the full partition function of the clusters, including shape fluctuations. As such fluctuations are not included in our mean-field calculation, we simply set the volume to be the volume of a unimer $4\pi R_1^3/3$. As the size distribution is dominated by the exponential term, uncertainties in this

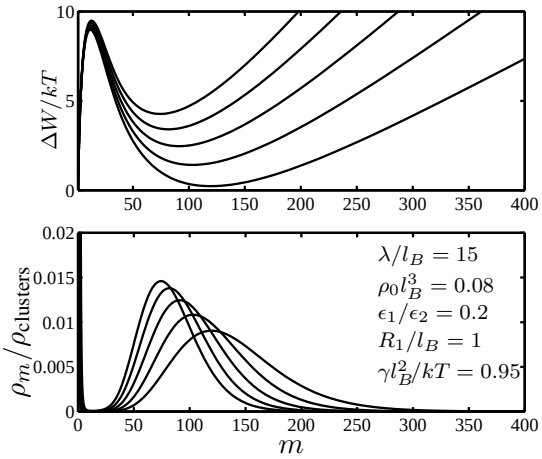

Figure 7.6: Cluster density profiles for varying supersaturations. The lower figure is obtained by dividing the cluster density as obtained by Eq. (7.18) at a given cluster size by the total number of clusters, obtained by integrating the profile generated by Eq. (7.18) over the entire cluster size range, in other words from barrier to barrier in the energy profiles shown in the upper figure.

volume factor should have little consequence on the results.

Figure 7.6 shows an example of the cluster size distribution (normalized by the total number of clusters) for several values of the supersaturation (unimer concentration). The bimodal nature of the distribution, with one peak for the unimers and one at some preferred size, is very similar to the behavior of micellar solutions. However, the width of the distribution is fairly broad and also the cluster peak shifts significantly to larger sizes as the supersaturation increases, in contrast to micellar solutions. In the case of micelles, the size is determined primarily by local packing constraints [27], which severely limit the range of size variations.

A quantity similar to the critical micelle concentration (CMC) can be defined for the cluster formation by examining the partitioning of molecules between the unimers and clusters. Because of the broad nature of the size distribution, we include the entire distribution of clusters between the two free energy barriers. A typical plot is shown in Fig. 7.7.

In the case of surfactant solutions, CMC is usually defined to correspond to the condition at which the surfactant molecules are equally distributed as unimers and micelles. In Fig. 7.7, this occurs at a scaled density $\rho/\rho_{\text{coex}} \approx 1.15$. [Here, ρ_{coex} is the unimer density at which coexistence occurs for the hypothetical uncharged system.] In our case, however, a more dramatic change of behavior occurs at $\rho/\rho_{\text{coex}} \approx 0.16$. This condition corresponds

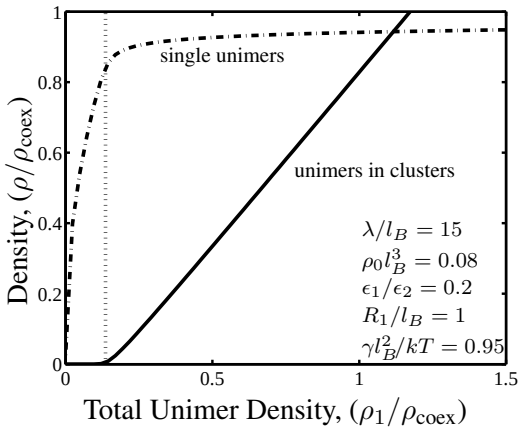

Figure 7.7: An illustration of the critical micelle-like behavior of cluster formation. The micellar (cluster) dissolution concentration (MDC) is denoted here by the dotted line.

to the first appearance of a local minimum in the free energy (curve A). Since the condition corresponding to curve A sets the limit of metastability for clusters of finite sizes, i.e., clusters with finite sizes can exist as entities with finite lifetime only beyond this supersaturation, it should be logically termed the micellar (cluster) dissolution concentration (MDC), following a similar concept (the micellar dissolution temperature) introduced in Ref. [28] in the study of micellar formation in diblock copolymer melts. For our current system, the MDC is a theoretically more meaningful concept than the CMC.

For concentrations beyond the MDC, adding more molecules to the system essentially only increases the number of clusters, with only small increases in the unimer density, similar to the behavior seen in micelles. Thus, once the clusters form, they provide a regulating mechanism for the unimer concentration and hence for the value of the supersaturation, thus limiting the driving force for nucleation of the bulk liquid phase. Therefore, for the same *nominal* relative supersaturation, condensation through metastable cluster intermediates will take much longer than the simple vapor-liquid nucleation.

7.4 Summary

In this paper we have examined a simple model of liquid-like clusters with preferred sizes that act as intermediates in the formation of a bulk liquid phase in solutions of charged

macromolecules. Such clusters arise as a consequence of competition between the short-range attractions that cause condensation and the long-range Coulomb interactions. The presence of these clusters can lead to a two-barrier nucleation scenario, with the first barrier associated with the formation of these clusters and the second associated with the growth of these preferred-sized clusters into the bulk liquid phase. However, in order that these clusters are only metastable and will eventually grow into a bulk liquid phase, charge neutralization by counter-ions and screening by both co-ions and counter-ions are crucial. The size of the clusters and the nucleation barrier from these clusters to the bulk liquid phase are determined by a combination of these effects.

While this study is motivated by the experimental work of Vekilov and co-workers on protein crystallization, direct application of our results does not explain the experimental observations. Their more recent work reveals that the clusters that are involved in the protein nucleation contain on the order of 10^5 or more protein molecules per cluster [9, 10]. This size is much too large to explain with our electrostatic model: The size in our case is limited by the Debye screening length, which under our sub-physiological conditions is 100 Å, corresponding to 10^2–10^3 protein molecules. Experiments on protein solutions and charged colloidal particles with depletion attraction show stable clusters with aggregation number of order 10 [29]. Also, the typical charge on proteins is larger than the small charge necessary to make the clusters metastable with respect to a bulk liquid (however, they can be metastable to the crystalline phase). Therefore, our study seems to suggest that the clusters in the protein nucleation are not due to electrostatic interactions. At present, the nature of the intermediate clusters in the protein crystallization is still unclear, although Vekilov and co-workers have recently suggested that the clusters are purely kinetic in nature as a result of slow dynamics [9]. Kumar and co-workers suggest that patchiness is an important feature in protein-protein interactions [30] and can give rise to slow relaxation dynamics at high densities [31], leading to a delay in the crystal formation. In these scenarios, the cluster intermediates observed in the work of Vekilov and co-workers would be some long-lived amorphous dense regions in the protein solution. However if that is the case, it is difficult to envision a two-barrier scenario for nucleation, which necessarily implies a free energy minimum between two barriers.

Although our results appear to exclude electrostatic interaction as the explanation behind the intermediate dense-liquid clusters in protein crystallization, the behavior predicted in this paper should be relevant and observable for many weakly charged macromolecular and colloidal systems, based on our estimates of the parameter ranges for this type of behavior. It is therefore desirable to refine and extend this initial study using more realistic models and more sophisticated approaches. For example, the use of molecular density functional theory that properly accounts for the excluded volume, short-range attractions, as well as electrostatic effects beyond the simple Poisson-Boltzmann approach, avoids the capillary approximations and also allows the inclusion of a crystalline phase.

At the phenomenological level, our model shares many common features with several systems that exhibit both macroscopic phase separation and aggregation into finite-size clusters, such as diblock copolymer–homopolymer mixtures [32], and solutions of amphiphilic copolymers [33]. For example, Wu and co-workers have reported stable aggregates with aggregation number ranging from 10 to several thousands (depending on temperature and concentration) in aqueous solutions of the non-ionic hydrophobically modified poly (N-isopropylacrylamide), between single-chain globules and macroscopic precipitation [34, 35]. It is quite probable that these mesoglobules can also exist in a metastable state relative to the dilute single-globule solution phase and macroscopically condensed phase, in which case condensation will occur through a two-step mechanism similar to the one proposed in our work.

Another interesting phenomenon that is hinted at by our results but cannot be addressed due to our use of the single cluster picture, is the relationship between microphase separation and macroscopic condensation. In particular, the existence of a metastable microphase separated state and its effects on the nucleation of a bulk dense liquid phase from a dilute solution phase appears to be a problem worthy of investigation.

Bibliography

[1] J. Cahn, J. Hilliard, Free energy of a nonuniform system. III. Nucleation in a two-component incompressible fluid, *J. Chem. Phys.* **31**, 688–699 (1959).

[2] D. W. Oxtoby, Homogeneous nucleation: Theory and experiment, *J. Phys.: Condens. Matter* **4**, 7627–7650 (1992).

[3] J. N. Smith, et al., Chemical composition of atmospheric nanoparticles during nucleation events in Atlanta, *J. Geophys. Res.* **110**, 1–13 (2005).

[4] M. J. Mora-Fonz, C. R. A. Catlow, D. W. Lewis, The role of solvation and pH in the nucleation of pure silica zeolites, *Stud. Surf. Sci. Catal.* **158**, 295–302 (2005).

[5] R. Seemann, et al., Dynamics and structure formation in thin polymer melt films, *J. Phys.: Condens. Matter* **17**, S267–S289 (2005).

[6] J. Drenth, The nucleation of lysozyme from a fluctuation point of view, *Cryst. Growth Des.* **5**, 1125–1127 (2005).

[7] P. G. Vekilov, Dense liquid precursor for the nucleation of ordered solid phases from solution, *Cryst. Growth Des.* **4**, 671–685 (2004).

[8] W. Pan, A. B. Kolomeisky, P. G. Vekilov, Nucleation of ordered solid phases of proteins via a disordered high-density state: Phenomenological approach, *J. Chem. Phys.* **122**, 174905 (2005).

[9] W. Pan, O. Galkin, L. Filobelo, R. L. Nagel, P. G. Vekilov, Metastable mesoscopic clusters in solutions of sickle-cell hemoglobin, *Biophys. J.* **92**, 267–277 (2007).

[10] O. Gliko, et al., Metastable liquid clusters in super- and undersaturated protein solutions, *J. Phys. Chem. B* **111**, 3106–3114 (2007).

[11] J. Groenewold, W. K. Kegel, Anomalously large equilibrium clusters of colloids, *J. Phys. Chem. B* **105**, 11702–11709 (2001).

[12] I. A. Nyrkova, A. R. Khokhlov, M. Doi, Microdomain structures in polyelectrolyte systems: Calculation of the phase diagrams by direct minimization of the free energy, *Macromolecules* **27**, 4220–4230 (1994).

[13] F. Sciortino, S. Mossa, E. Zaccarelli, P. Tartaglia, Equilibrium cluster phases and low-density arrested disorderd states: The role of short-range attraction and long-range repulsion, *Phys. Rev. Lett.* **93**, 055701(1–4) (2004).

[14] J. Lutsko, G. Nicolis, The effect of the range of interaction on the phase diagram of a globular protein, *J. Chem. Phys.* **122**, 244907 (2005).

[15] R. P. Sear, W. M. Gelbart, Microphase separation versus the vapor-liquid transistion in systems of spherical particles, *J. Chem. Phys.* **110**, 4582–4588 (1999).

[16] J. Lothe, G. M. Pound, On the statistical mechanics of nucleation theory, *J. Chem. Phys.* **45**, 630–634 (1966).

[17] H. Reiss, J. Katz, Resolution of the translation-rotation paradox in the theory of irreversible condensation, *J. Chem. Phys.* **46**, 2496–2499 (1966).

[18] H. Reiss, J. L. Katz, E. R. Cohen, Translation-rotation paradox in the theory of nucleation, *J. Chem. Phys.* **48**, 5553–5560 (1968).

[19] I. Kusaka, Statistical mechanics of nucleation: Incorporating translational and rotational free energy into thermodynamics of a microdroplet, *Phys. Rev. E* **73**, 031607 (2006).

[20] R. P. Sear, P. B. Warren, On the electrical double layer contribution to the interfacial tension of protein crystals, *J. Chem. Phys.* **117**, 8074–8079 (2002).

[21] S. Hutchens, Z.-G. Wang. Unpublished work.

[22] C. N. Schutz, A. Warshel, What are the dielectric "constants" of proteins and how to validate electrostatic models?, *Proteins* **44**, 400–417 (2001).

[23] A. V. Dobrynin, M. Rubinstein, Hydrophobic polyelectrolytes, *Macromolecules* **32**, 915–922 (1999).

[24] T. M. Davis, et al., Mechanistic principles of nanoparticle evolution to zeolite crystals, *Nat. Mater.* **5**, 400–408 (2006).

[25] J. D. Rimer, R. F. Lobo, G. V. Dionisios, Physical basis for the formation and stability of silica nanoparticles in basic solutions of monovalent cations, *Langmuir* **21**, 8960–8971 (2005).

[26] I. Kusaka, D. W. Oxtoby, Z.-G. Wang, On the direct evaluation of the equilibrium distribution of clusters by simulation. ii, *J. Chem. Phys.* **115**, 6898–6906 (2001).

[27] J. N. Israelachvili, D. J. Mitchell, B. W. Ninham, Theory of self-assembly of hydrocarbon amphiphiles into micelles and bilayers, *J. Chem. Soc., Faraday Trans. 2* **72**, 1525–1568 (1976).

[28] J. Wang, Z.-G. Wang, Y. Yang, Nature of disordered micelles in sphere-forming block copolymer melts, *Macromolecules* **38**, 1979–1988 (2005).

[29] A. Stradner, et al., Equilibrium cluster formation in concentrated protein solutions and colloids, *Nature* **432**, 492–495 (2004).

[30] H. Liu, S. K. Kumar, F. Sciortino, G. T. Evans, Vapor-liquid coexistence of fluids with attractive patches: An application of wertheim's theory of association, *J. Chem. Phys.* **130**, 044902 (2009).

[31] S. Kumar. Unpublished.

[32] M. W. Matsen, Phase-behavior of block-copolymer homopolymer blends, *Macromolecules* **28**, 5765 (1995).

[33] E. Timoshenko, Y. A. Kuznetsov, Analysis of stability of macromolecular clusters in dilute heteropolymer solutions, *J. Chem. Phys.* **112**, 8163 (2000).

[34] M. Siu, H. Y. Liu, X. X. Zhu, C. Wu, Formation of mesoglobular phase of amphiphilic copolymer chains in dilute solution: Effect of comonomer composition, *Macromolecules* **36**, 2103 (2003).

[35] G. Zhang, C. Wu, Folding and formation of mesoglobules in dilute copolymer solutions, *Adv. Polym. Sci.* **195**, 101 (2006).

Appendix A

Testworks Compression Method

The list of test segments comprising the compression method utilized in this thesis is given in Figure A.1. I will briefly describe the purpose of each segment or group of test segments along with relevant details so that this method can be easily reproduced from the information in this appendix.

Testing the Sample:

1–9 Prepare the indenter head for loading by placing it above the sample testing position at a surface approach start position (usually $u_{\mathrm{raw}} = 0$ for the first test as discussed previously) and turning on the CSM (25 Hz, 10 μN).

10–11 Perform the surface find by approaching at a sufficiently slow loading rate, 0.005 mN/s, and stores its position in 'Raw Displacement at the Surface.'

12–16 Pull the indenter 1 μm away from the surface and turns off the harmonic oscillations.

17–25 Returns the indenter head to the surface of the pillar and waits for it to stabilize to within 20 nm of that value before changing to a constant load hold during with the drift is monitored until falling below a threshold of 0.5 nm/s. This new position is marked with 'Surface Marker.'

26 & 42 The loading loop which allows for multiple load-unload cycles, though only one was used in this thesis.

27–32 Calculates the displacement limit and loads at a constant prescribed displacement rate until it is reached. The details of segment 30 are shown in Figure A.2.

33 A short hold at the maximum displacement to eliminate any lag between the indenter position and values reported by the electronics (only really necessary for very fast strain rates). Holds for 0.003 s.

34–39 Calculates the unload limit (10% of the maximum load) and unloads at a constant prescribed displacement rate until it is reached. The details of segment 37 are similar to those in Figure A.2, but with the loading direction being 'Unloading' and the rate being a value set to the negative of the 'Prescribed Displacement Rate.'

40 Another hold segment identical to 33.

41 Augmenting the load counter to determine if reloading is necessary.

43–44 Unloading the pillar completely (until the indenter reaches the surface location position) and ending the sample test.

Characterizing the Machine:

45 Moving the sample tray out of the way so that the indenter head can be characterized in air unimpeded.

46 & 74 A 'Cycles Method' loop for characterizing the machine response in air at 'NumberOfCharPoints' = 10.

47–48 Calculate the raw displacement position at which characterization should occur and move to it.

49–52 If this is the first point characterized run the 'NanoConfig' segment to find the offset and set the Gain to 3.

53–57 Turn on the CSM and allow it to reach a steady state.

58–67 Measure and monitor the phase angle until it reaches a constant value (changes of less than 0.2 degrees over a 10 second hold).

68–73 Take data and augment cycle (including store data acquired during the hold in segment 70.)

Figure A.1: List of test segments used for compression of VACNT pillars.

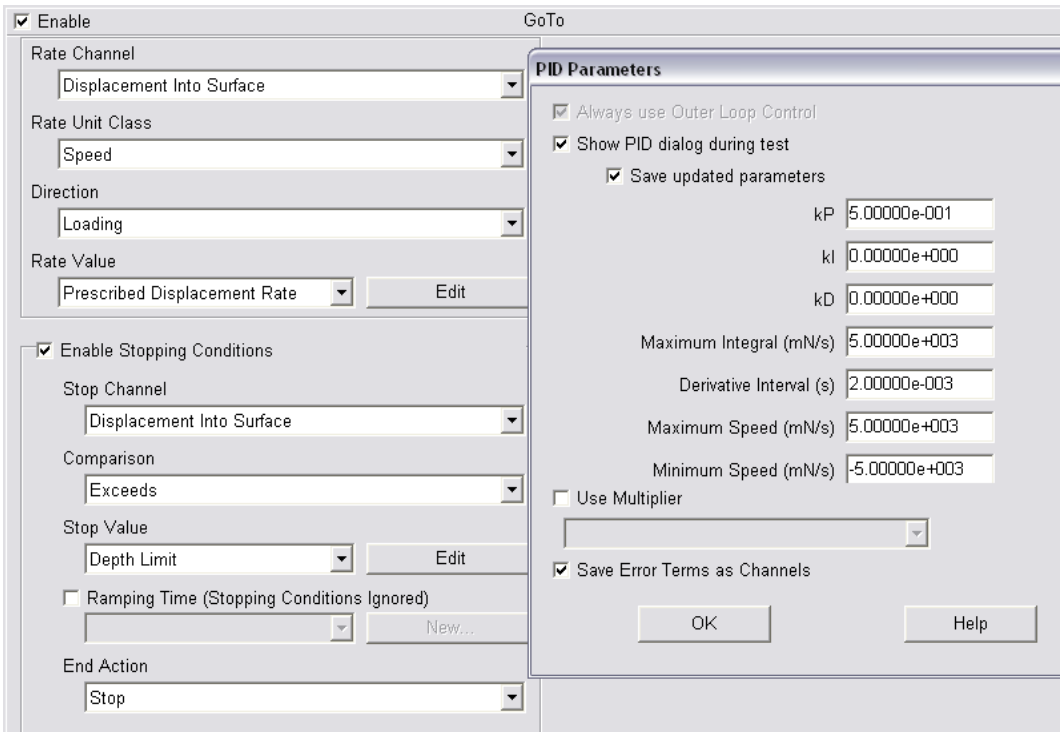

Figure A.2: Screen capture of the Testworks PID parameters used for loading.

Appendix B

Testworks Compression Method

The list of test segments comprising the DMA method utilized in this thesis is given in Figure B.1. As in Appendix A, I briefly describe the purpose of each segment or group of test segments along with relevant details so that this method can be easily reproduced from the information in this appendix.

Testing the Sample:

1–15 Accomplish the same task as in 1.-11. in the compression test method in Appendix A.

16 & 61 The loop for scanning through the displacement values to be characterized. (A 'cycles method' loop.)

17–21 Calculate and go to the desired displacement for characterization.

22–23 Find the offset and set the gain to 5.

24–29 Wait for sample drift to be <1 nm/s while correcting drift so that characterization occurs at the desired raw displacement.

30 Choose how many frequencies to test.

31 & 59 Loop over the series of frequencies to test.

32–35 Select and set the test frequency and oscillation amplitude allowing for a short stabilization hold.

36–38 Capture and use the harmonic load value that corresponds to that oscillation amplitude. Another short hold for stabilization.

39–48 Wait for phase angle to reach a constant value. (1 degree change over a 5 second hold.)

49–51 Gather data.

52–53 Turn off CSM.

54–58 Store gathered data.

60 Increment cycle number and store gathered data in cycles variables.

62–65 Reset system for similar characterization in air.

Characterizing the Machine:

Segments 66–106 perform the same overall task as the first loop in this test, i.e., holding at several different raw displacements and running a series of steady-state frequency holds at each. The only difference lies in segments 75 through 84 in which oscillation amplitudes (harmonic load targets) are set in two different ways depending on if the frequency is greater than 30 Hz or less than 30 Hz. These thresholds are based on some trial and error values enabling measurement of the cleanest data possible.

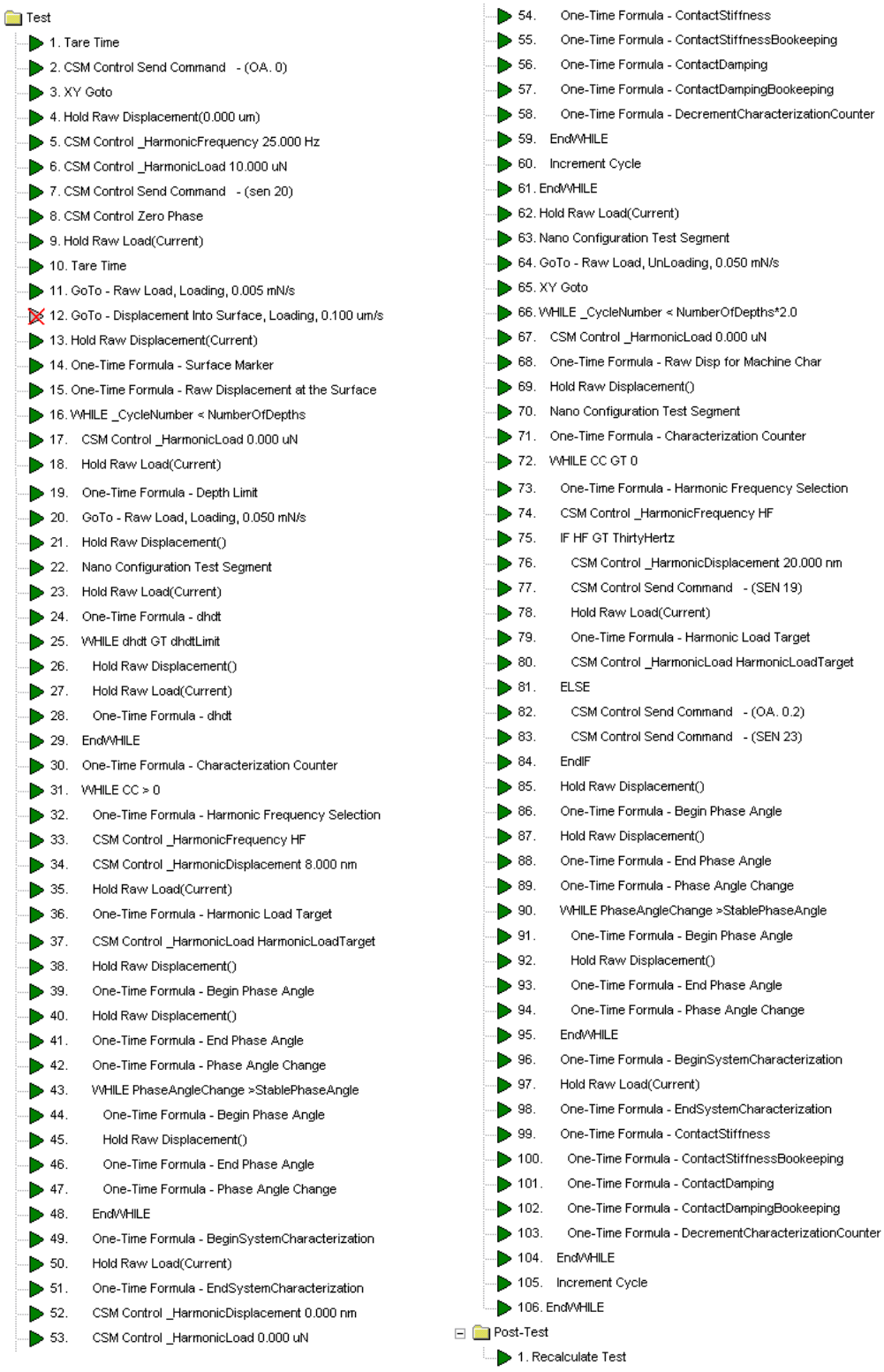

Figure B.1: List of test segments used for viscoelastic measurement of VACNT pillars.

Appendix C

FIB Procedure for VACNT pillar

VACNT pillar geometries were milled using a FEI Nova 200 Dual Beam system in combination with the Selective Carbon Mill ($MgSO_4$-$7H_2O$) gas injection needle. The first step is milling a 30 μm $\times$ 60 μm rectangluar viewing window. This window is necessary to obtain tilted views of the milled pillar. The window must be milled first to minimize redeposition on milled pillars. The is accomplished with a 7 nA current for 6.5 minutes (for 4 windows). Following the large viewing window and small rectangular area at the end of the window (30 μm $\times$ 5 μm) was milled to reduce redeposition that might interefere with the window. A 5 nA current for 40 seconds was used on each individual window. Following the creation of the series of windows, a series of decreasing annuli were milled at one end of following the procedure outlined in Table C.1.

Table C.1: Procedure for FIB milling 20 μm diameter VACNT pillars from a continuous film

Outer Diameter [μm]	**Inner Diameter [μm]**	**Current [nA]**	**Time [s]**
50	35	7	180
35	30	5	66
31	25	5	68
26	23	3	50
24	21	3	46
21.5	20.5	3	16
21	20	3	14

* After the first annulus, subsequent annuli were milled at a magnification of 2400×.

Appendix D

Simulated CNT Images

Simulated VACNT microstructure images for image analysis verification are constructed using the following series of steps.

1. A Gaussian distribution ($\mu_{\text{sat}} \approx 128$, $\sigma_{\text{sat}} \approx 20$) of line intensity values is generated for the number of lines desired in an image.

2. A 1400 $\times$ 1400 constant background of intensity $\mu_{\text{sat}} - 2\sigma_{\text{sat}}$ is generated.

3. Lines are drawn on the background image in order of increasing intensity. Lines that would have intensity less than the background disappear. Each line has thickness generated by a log-normal distribution having the same characteristics as those measured in the experimental images (Section 3.2.1). Lines are uniformly distributed on the background with a Gaussian distribution of angles having a mean of 0 (vertical) and standard deviation of π/32.

4. Gaussian noise with a mean of 0 and standard deviation of 0.02 is added to the lined image.

Appendix E

Free Energy Expressions for Differing Dielectric Constants

Defining the Bjerrum length using the dielectric constant of the solvent, ϵ_2, the free energy expression for a cluster with dielectric constant ϵ_1 within a reservoir with dielectric constant ϵ_2 is

$$W^{(\mathrm{e})} = -kT \int_0^\infty r^2 dr \Bigg\{ \frac{1}{2} \left(1 + \left[\frac{\epsilon_1}{\epsilon_2} - 1 \right] \theta(R_c - r) \right) \left[\nabla_r \xi \right]^2 + \left(\frac{l_B}{\lambda} \right)^2 \left(1 + \left[e^{-\beta \Delta \mu^*} - 1 \right] \theta(R_c - r) \right) \cosh\left[\xi(r) \right] - 4\pi \rho_0 l_B^3 \xi(r)\, \theta(R_c - r) \Bigg\}. \tag{E.1}$$

The corresponding Poisson-Boltzmann equation is

$$- \left(1 + \left[\frac{\epsilon_1}{\epsilon_2} - 1 \right] \theta(R_c - r) \right) \nabla_r^2 \xi + \left(\frac{l_B}{\lambda} \right)^2 \left(1 + \left[e^{-\beta \Delta \mu^*} - 1 \right] \theta(R_c - r) \right) \sinh\left[\xi(r) \right] = 4\pi \rho_0 l_B^3\, \theta(R_c - r). \tag{E.2}$$

Appendix F

Toward a DFT Approach to Polyelectrolyte Behavior in Small Systems

F.1 Introduction

The osmotic pressure of a solution is generally understood in terms of macroscopic, homogeneous systems. The following notes address the idea of osmotic pressure as defined for small systems.

F.2 Theoretical Framework

In this section we obtain the appropriate free energy for a semi-open system employing an implicit solvent model through the application of McMillan-Meyer solution theory. We begin with the variational formulation for the free energy of a semi-open system including the solvent. First, imagine a volume of interest, V, enclosed by a semi-permeable membrane within a much larger system, V_{tot}. n_m macromolecules (or monomers if the macromolecule is a polymer) are trapped within V. Solvent and small ion molecules move freely accross the membrane. Due to its size, the reservoir, $V_{tot}-V$, has a constant pressure, p_0, and chemical potentials μ_s and μ_i for the solvent and small ions, respectively. The total Hemlholtz free energy for this system is

$$F_{tot}(n_m, N_s, N_i, V; n_s, n_i) = F(n_m, n_s, n_i, V) + F_{res}(N_s - n_s, N_i - n_i, V_{tot} - V)$$
$$\approx F(n_m, n_s, n_i, V) + p_0 V - n_s\mu_s - n_i\mu_i + F_{res}(N_s, N_i, V_{tot}).$$

The equilibrium number of solvent and ion molecules, n_s and n_i, are obtained from minimizing F_{tot} with respect to these variables. In the limit of an infinite reservoir, the approximation in the second line becomes exact, with the last term being a constant which can be used to define the following thermodynamic potential

$$W(n_m, \mu_s, \mu_i, V; n_s, n_i) = F_{tot}(n_m, N_s, N_i, V; n_s n_i) - F_{res}(N_s, N_i, V_{tot})$$
$$= F(n_m, n_s, n_i, V) + p_0 V - n_s\mu_s - n_i\mu_i \tag{F.1}$$

with equilibrium conditions

$$\frac{\partial W}{\partial n_s} = 0 \quad \text{or} \quad \frac{\partial F}{\partial n_s} = \mu_s$$
$$\frac{\partial W}{\partial n_i} = 0 \quad \text{or} \quad \frac{\partial F}{\partial n_i} = \mu_i.$$

Pressure is given by the negative of the derivative of the Helmholtz free energy with respect to volume at fixed number of molecules for all species. In this case, because of the variation conditions with respect to n_s and n_i, this derivative, when applied to W, is at fixed n_m, μ_i, and μ_s. Thus we obtain

$$-\left.\frac{\partial W}{\partial V}\right|_{n_p,\mu_s,\mu_i} = -\left.\frac{\partial F}{\partial V}\right|_{n_p,n_s,n_i} - p_0$$
$$= p - p_0 = \Pi.$$

Therefore, if we obtain the potential W, its derivative with respect to V will yield the

excess pressure of the macromolecule system with respect to a solvent and ion only system, Π. This is the osmotic pressure by definition, i.e., the difference in pressure required to equilibrate the macromolecule subsystem with the reservoir. The potential obtained in Eq. (F.1) includes degrees of freedom from all molecules, but applying ideas from McMillan-Meyer theory, we can eliminate the degrees of freedom of either the solvent, ion or both, resulting in a simpler potential function, W'.

While the W in Eq. (F.1) is technically for a closed system (given the minimization of F_{tot}), in the thermodynamic limit it is equivalent to the maximum term of an analagous semi-open system which we will also call W. This semi-open potential of the form given by Eq. (F.1) suggests the following statistical mechanical expression:

$$\begin{aligned} W &= -kT \log \Psi(n_m, \mu_s, \mu_i, V) + p_0 V \\ &= -kT \log \left[\frac{\Psi(n_m, \mu_s, \mu_i, V)}{\Xi(\mu_s, \mu_i, V)} \right] \end{aligned} \tag{F.2}$$

where $\Psi(n_p, \mu_s, \mu_i, V)$is a semi-grand partition function open with respect to the solvent and ions, but closed with respect to the macromolecule and $\Xi(\mu_s, \mu_i, V)$ is the grand partition function in the absence of the macromolecule, k is the Boltzmann constant, and T is the temperature. Next, we manipulate Eq. (F.2) into an expression involving the potential of mean force for the macromolecules so that we may eliminate explicit reference to the solvent.

$$\begin{aligned} \Psi(n_m, \mu_s, \mu_i, V) &= \frac{1}{n_m! \Lambda_m^{3n_m}} \sum_{n_s \geq 0} \sum_{n_i \geq 0} \frac{\exp(\beta n_s \mu_s + \beta n_i \mu_i)}{n_i! \Lambda_i^{3n_i} n_s! \Lambda_s^{3n_s}} \\ &\quad \times \int d\{\mathbf{r}_{n_m}\} \int d\{\mathbf{r}_{n_s}\} \int d\{\mathbf{r}_{n_i}\} \exp\left[-\beta U(\{\mathbf{r}_{n_m}\}, \{\mathbf{r}_{n_s}\}, \{\mathbf{r}_{n_i}\})\right] \end{aligned}$$

$$\begin{aligned} \Xi(\mu_s, \mu_i, V) &= \sum_{n_s \geq 0} \sum_{n_i \geq 0} \frac{\exp(\beta n_s \mu_s + \beta n_i \mu_i)}{n_i! \Lambda_i^{3n_i} n_s! \Lambda_s^{3n_s}} \\ &\quad \times \int d\{\mathbf{r}_{n_s}\} \int d\{\mathbf{r}_{n_i}\} \exp\left[-\beta U(\{\mathbf{r}_{n_s}\}, \{\mathbf{r}_{n_i}\})\right] \end{aligned}$$

β is $1/kT$, and Λ_m, Λ_s, and Λ_i are the thermal de Broglie wavelengths of the macromolecule (the monomer if it is a polymer), solvent, and ion molecules respectively. $\{\mathbf{r}_{n_j}\}$ represents the set of of $n_j$position vectors, $\mathbf{r}$, corresponding to molecules of type j. Division of $\Psi(n_p, \mu_s, \mu_i, V)$ by $\Xi(\mu_s, \mu_i, V)$ amounts to an averaging over the solvent degrees of freedom, which defines an effective potential

$$\begin{aligned}
\exp\left[-\beta U_{\text{eff}}(\{r_{n_m}\})\right] &= \sum_{n_s\geq 0}\sum_{n_i\geq 0}\frac{\exp(\beta n_s\mu_s+\beta n_i\mu_i)}{n_i!\Lambda_i^{3n_i}n_s!\Lambda_s^{3n_s}} \\
&\quad\times\int d\{\mathbf{r}_{n_s}\}\int d\{\mathbf{r}_{n_i}\}\exp\left[-\beta U(\{\mathbf{r}_{n_m}\},\{\mathbf{r}_{n_s}\},\{\mathbf{r}_{n_i}\})\right. \\
&\quad\left.+\beta U_0(\{\mathbf{r}_{n_s}\},\{\mathbf{r}_{n_i}\})\right] \\
&\quad\times\frac{\exp\left[-\beta U_0(\{\mathbf{r}_{n_s}\},\{\mathbf{r}_{n_i}\})\right]}{\Xi(\mu_s,\mu_i,V)} \\
&\equiv \left\langle\exp\left[-\beta U(\{\mathbf{r}_{n_m}\},\{\mathbf{r}_{n_s}\},\{\mathbf{r}_{n_i}\})+\beta U_0(\{\mathbf{r}_{n_s}\},\{\mathbf{r}_{n_i}\})\right]\right\rangle_0 \qquad \text{(F.3)}
\end{aligned}$$

where the average is taken with respect to the probability of finding solvent and ion molecules in a solvent-ion only solution. In order to have a meaningful, finite-valued potential for a single macromolecule or monomer we define an effective one-body potential, $U_{1,\text{eff}}$, for an isolated macromolecule or monomer in the solvent.

$$\exp\left[-\beta U_{1,\text{eff}}\right] = \frac{\Psi(1,\mu_s,\mu_i,V)}{\Xi_0(\mu_s,\mu_i,V)\frac{V}{\Lambda_m^3}}, \qquad \text{(F.4)}$$

where Ψ/Ξ is an average over the degrees of freedom analagous to that in U_{eff} and V/Λ_m^3accounts for the translational freedom of the molecule in V. Subtracting Eq. (F.4) from Eq. (F.3) amounts to a redefinition of the reference point for the potential, resulting in the potential of mean force, $U_{\text{PMF}}(\{\mathbf{r}_{n_m}\}) = U_{\text{eff}}(\{\mathbf{r}_{n_m}\}) - n_m U_{1,\text{eff}}$, the average potential the macromolecules in solution feel due to all interactions of and with the solvent. Now Eq. F.2 can be written as

$$\exp[-\beta W] = \frac{\exp(-\beta n_m U_{1,\text{eff}})}{n_m!\Lambda_m^{3n_m}}\int d\{\mathbf{r}_{n_m}\}\exp\left[-\beta U_{\text{PMF}}(\{\mathbf{r}_{n_m}\})\right], \qquad \text{(F.5)}$$

which has the same appearance as a canonical partition function for a one-component sys-

tem with interaction potential $U_{\rm PMF}$. Later on in our example calculation for a semi-dilute polyelectrolyte confined within a semi-permeable shell, it becomes desirable to explicitly keep the degrees of freedom for the ions. In this case we will have a potential of mean force for the ions in solvent as well as inbetween the polymer and ions. By multiplying and dividing the ratio of partition functions within the logarithm of (F.2) by the grand partition function $\Xi_s(\mu_s, V)$ corresponding to a pure solvent and going through similar steps as those leading to (F.5), we obtain

$$\exp[-\beta W] = \exp[-\beta n_m U_{1,\rm eff}] \frac{\Psi_{\rm PMF}(n_m, \mu_i, V)}{\Xi_{\rm PMF}(\mu_i, V)}. \tag{F.6}$$

Ψ_{PMF} is a semi-grand partition function (closed for macromolecule, but open for ions) with macromolecules and ions interacting with potential of mean force and Ξ_{PMF} is the grand partition function for the ions interacting with potential of mean force .

Because the effective one-body potential is independent of volume, it can be lumped into the definition of W. Doing this, taking the logarithm of both sides of Eq. (F.6), and multiplying by $-kT$ yields

$$W(n_m, \mu_i, V) = -kT \log(\Psi_{PMF}) + kT \log(\Xi_{PMF}). \tag{F.7}$$

The first term defines the free energy a semi-open system interacting through potential of mean force, $F_{PMF}(n_m, n_i, V) - n_i\mu_i$. The second term is the free energy of an open solvent mediated ion system, $\Pi_0 V$. Thus averaging over the solvent degrees of freedom has allowed (F.1) to be rewritten in terms of implicit solvent interactions

$$W(n_m, \mu_i, V; n_i) = F(n_m, n_i, V) + \Pi_0 V - n_i\mu_i \tag{F.8}$$

where Π_0 can also be viewed as the osmotic pressure of the reservoir due to the ions in solution.

F.3 Osmotic Pressure for Small Systems

In this section, we adapt the general derivation in Section F.2 to the specific case of a polyelectrolyte in the semi-dilute regime confined within a spherical capsule that is permeable to point-charge-like ions and solvent, which will be accounted for implicitly. The general discussion above applies to macroscopic systems where the boundary between the system and reservoir can be ignored. In other words, they are sufficiently uncoupled that the reservoir is homogeneous. In small systems, long-ranged interactions of the system with the reservoir leads to coupling between them that cannot be ignored and the additivity assumed in the derivation of Eq. (F.1) does not apply. Thus, we need to modify the way we look at the system in order to calculate osmotic pressure in these small systems.

F.3.1 Derivation of Osmotic Pressure

If we draw a sufficiently large volume, V, around the capsule, the reservoir becomes homogeneous, we may apply Eq. (F.8) in which the free energy, $F(n_m, n_i, V)$, includes contributions from both inside and outside the capsule of volume $V_R = \frac{4}{3}\pi R^3$, and W becomes independent of V. To illustrate the latter, we increase the volume from $V$to $V + \Delta V$. Because the boundary for V is far from the capsule, the composition in any volume outside it is homogeneous. If Δn_i is the number of ions in ΔV, the change in W is

$$\Delta W = F(\Delta n_i, \Delta V) + \Pi_0 \Delta V - \Delta n_i \mu_i. \tag{F.9}$$

Since $F(\Delta n_i, \Delta V) - \Delta n_i \mu_i = \Pi_0 \Delta V$ for a uniform system, ΔWequals zero, and $W$is an excess free energy that is independent of V in the limit of sufficiently large V.

While W does not depend on V, it does depend strongly on V_R through the dependence of n_i and $F(n_m, n_i, V)$ on V_R. We now illustrate how the negative of the derivative of W with respect to V_R is the osmotic stress applied by the capsule wall. First, imagine the capsule is an elastic shell with an unstressed area A_0. For small expansion or contraction to a new area, A_R, the free energy cost is

$$F_{\text{elastic}} = \frac{1}{2}\kappa A_0^{-1} \left(A_R - A_0\right)^2 . \tag{F.10}$$

So for the total free energy of the system consisting of the encapsulated solution, the local reservoir to the encapsulated solution, and the elastic capsule is $\Omega = W + F_{\text{elastic}}$. At equilibrium we have $\partial\Omega/\partial n_i = 0$ from the variational condition for W in (F.8) and $\partial\Omega/\partial V_R = 0$ from F_{elastic}. From the second equilibrium condition we have

$$\frac{\partial W}{\partial V_R} + \frac{\partial F_{\text{elastic}}}{\partial A_R}\frac{\partial A_R}{\partial V_R} = 0. \tag{F.11}$$

From (F.10), $\partial F_{\text{elastic}}/\partial A_R = \kappa A_0^{-1}(A_R - A_0) \equiv \sigma$, where σ is the tension of the shell. Therefore, the variation condition for V_R yields

$$-\frac{\partial W}{\partial V_R} = \frac{2\sigma}{R}. \tag{F.12}$$

By the Laplace-Young equation, the right hand side of the expression is naturally interpreted as a pressure difference between the inside and outside of the capsule shell.

F.4 Confined Polyelectrolyte in a Semi-Open System

The particular system to which we apply the previous arguments for the use of an implicit free energy and definition of osmotic stress is that of a polyelectrolyte confined within a spherical capsule permeable to the solvent and small ions, but impermeable to the polyelectrolyte. The free energy of this system may be constructed in parts. First, the free energy of a polymer in the semi-dilute regime is given by Flory-Huggins and self-consistent field theory. (The Flory-Huggins interaction parameter is zero because we are not interested in phase change of the confined polymer.)

$$F_{poly} = \int_v d\mathbf{r}\frac{1}{v}\left\{(1-\phi)\ln(1-\phi) + \frac{b^2}{6}\left[\nabla(\phi^{1/2})\right]^2\right\}. \tag{F.13}$$

Volumeless, free ions with varying number density c_+ and c_- and reservoir density $c_+|_\infty = c_-|_\infty = c_\infty$ have free energy

$$F_{ions} = \int_v d\mathbf{r}\left\{c_+\ln c_+ - c_+ + c_+ - (c_\infty\beta\mu_\infty - c_\infty)\right.$$

$$+c_{-}\ln c_{-} - c_{-} + c_{-} - (c_{\infty}\beta\mu_{\infty} - c_{\infty})\} \,.$$

Finally, the electrostatic interaction should accounted for by the variational form of the Poisson-Boltzmann equation.